FEASIBILITY AND DESIGN OF BLAST MITIGATION SYSTEMS FOR NAVAL APPLICATIONS USING WATER MIST FIRE SUPPRESSION SYSTEMS

By

Julie A. Kitchenka

S.B. Engineering Sciences (Mechanical)
Harvard University, 1998

Submitted to the Department of Ocean Engineering and the Department of Civil and Environmental Engineering in partial fulfillment of the requirements for the degrees of

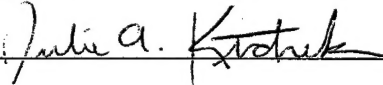Naval Engineer in Naval Architecture and Marine Engineering
And
Master of Science in Civil and Environmental Engineering
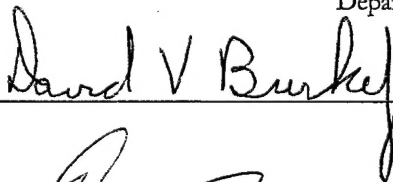At the
MASSACHUSETTS INSTITUTE OF TECHNOLOGY
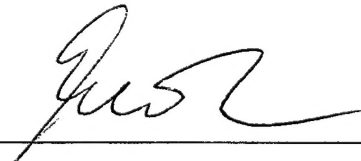June 2004

Signature of Author _____
Department of Ocean Engineering and
Department of Civil and Environmental Engineering
07 May 2004

Certified By _____

David V. Burke
Senior Lecturer
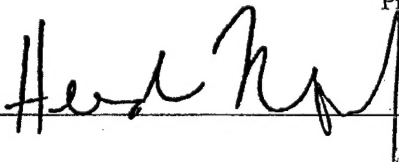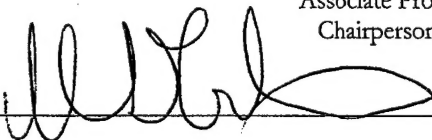Thesis Supervisor

Certified By _____

Eduardo Kausel
Professor of Civil and Environmental Engineering
Thesis Reader

Accepted By _____

Heidi M. Nepf
Associate Professor of Civil and Environmental Engineering
Chairperson, Department Committee on Graduate Studies

Accepted By _____

Michael Triantafyllou
Professor of Ocean Engineering
Chairperson, Department Committee on Graduate Studies

FEASIBILITY AND DESIGN OF BLAST MITIGATION SYSTEMS FOR NAVAL APPLICATIONS USING WATER MIST FIRE SUPPRESSION SYSTEMS

By

Julie A. Kitchenka

Submitted to the Department of Ocean Engineering and
The Department of Civil and Environmental Engineering
On 07 May 2004, in partial fulfillment of the requirements for the degrees of

Naval Engineer in Naval Architecture and Marine Engineering
and
Master of Science in Civil and Environmental Engineering

ABSTRACT

The recent trend of using fine water mist systems to replace the legacy HALON-1301 fire suppression systems warrants further study into other applications of the water mist systems. Preliminary research and investigation indicates that fine mists (20-25 μm droplet size) may reduce peak overpressures of a shock wave traveling through a space. Such pressure reductions could be used to mitigate the destructive effects of a shock wave (initiated by an explosive device) traveling through a structure.

Currently these blast mitigation effects have only been demonstrated in small-scale shock tube tests and computer simulations. Uncertainty exists as to the scalability of such a system. The intention of this research is to investigate the applicability of such a blast mitigation system for shipboard use. Study into the degree of mitigation necessary to make a system practical for shipboard installation was conducted. In addition, a theoretical study of the mechanisms of blast mitigation using water mists was completed.

Preliminary design of a full-scale system was examined. Given the recent trend toward tumblehome hull forms in future Naval Combatant designs, there exists strong applicability of this system in the "dead" spaces created by the shaping of the tumblehome hull. Further work is needed in numerical modeling and laboratory testing of specific phases of the mitigation. The end goal is a feasible design of a blast mitigation system to be used in the outermost spaces of Naval Combatants to protect interior vital system spaces.

Thesis Supervisor: David V. Burke
Title: Senior Lecturer

Thesis Reader: Eduardo Kausel
Title: Professor of Civil and Environmental Engineering

TABLE OF CONTENTS

LIST OF FIGURES

ACKNOWLEDGMENTS

NOMENCLATURE

DDS: U.S. Navy Design Data Sheets. Contain construction and performance requirements and guidelines for U.S. Navy ships.

GenSpecs: U.S. Navy General Specifications for construction and performance of U.S. Navy ships.

Survivability: Concept that includes all aspects of protecting personnel, weapons, and supplies while simultaneously deceiving the enemy.

ODS: Ozone Depleting Substance.

ODP: Ozone Depletion Potential.

CFC: Chlorofluorocarbon, a common refrigerant.

CPSMA: Commission on Physical Sciences, Mathematics, and Applications.

τ_v: Particle equilibration time.

m: Individual particle mass.

η: mass loading ratio.

P_o: Peak incident overpressure. Peak pressure in the incident shock wave.

P_a: Ambient atmospheric pressure.

P_r: Maximum reflected overpressure. Peak pressure due to additive effect of incident and reflected shock waves.

q_o: Dynamic pressure. Accounts for dynamic effects of pressure pulse duration.

P_s: Stagnation pressure. Static equivalent pressure including dynamic effects.

τ: Duration of positive phase of pressure pulse.

Z: Scaled blast range.

W: Weight of explosive for blast calculations.

μ: Ductility factor. Used in DDS 100-9 to account for allowable plastic deformation levels.

R_p: Panel resistance in pounds force. Used in DDS 100-9 to evaluate stiffened panel design.

σ_o: Plastic flow stress

M_o: Plastic collapse moment

σ_{odyn}: dynamic yield stress

ε_{dot}: strain rate (= rupture strain/pulse time)

L: Frame spacing. Horizontal length of stiffened panel.

H: Plate thickness.

B: Stiffener spacing or deck height.

PVLS: Peripheral Vertical Launch System

INTRODUCTION

Central to the strength of a naval force is its ability to survive and continue to fight through a battle situation. The United States Department of Defense Dictionary of Military Terms defines survivability as "a concept that includes all aspects of protecting personnel, weapons, and supplies while simultaneously deceiving the enemy." The ability of a system to retain functionality in a damaged state is central to the concept of survivability and therefore is a primary concern in the design of naval combatants. The protection of personnel and equipment from battle damage is essential to the effectiveness of a ship. Warships must be designed with inherent resistance to hull and shipboard system damage inflicted under battle conditions. Part of this protection includes methods of strengthening the structure of the ship to resist damage from blast-type loading. The stronger the ship, the more likely it is to survive battle damage and continue its ability to fight in a damaged condition.

Strengthening ships to blast loading is traditionally achieved through enhanced structural design, but can include measures to mitigate the peak overpressures and loads placed on a ship by shock impingement. Water mists have been shown to achieve a degree of mitigation of blast shocks in a confined space, namely a reduction in the velocity and peak overpressure of the impinging shock wave. The potential application of this feature of water mists to U.S. Naval combatants is presented in this study.

Ship Design for Blast Resistance

There are obvious trade-offs to battle hardening of Naval assets. Allocating significant amounts of weight and space to armor plating or blast-resistant structures will cost in speed, efficiency, endurance, and overall effectiveness of the platform. In the days before technologically advanced radars and guided weapons, armor plating was essential to ship design since major threats included ship-to-ship gunfire and close-in ballistic fire. However, recent years have turned the focus on creating ships with low signatures and small radar cross sections to make targeting by enemies more difficult. To accomplish

these goals, ships must appear small and quiet, often conflicting design features to side-hull protection. Modern warships are also filled with the sensitive electronic equipment required to compete in today's high-tech arenas. These ships contain a much higher ratio of combat system equipment weight to ship structural weight in comparison to naval combatants of the past. The next generation of ships is entirely electric and must carry a previously unheard of amount of electrical generation and distribution equipment to complete their required missions. They will operate in an environment where the force that can conduct the best surveillance, advanced warning, and precision strike missions will dominate the field. This means that ships must be fast, technologically advanced, and robust.

As technologically advanced next-generation ships are designed to meet the computing and combat systems needs of the future, the concept of survivability in ship design has changed. Battle-hardening no longer means the ability to withstand hits from explosive shells. Ships are designed to project power far away and detect and combat threats from equally long distances. As a result, heavy armor has been traded for high-tech detection and engagement systems. However, the close-in threat has not disappeared. The most daunting threats to the new generation of ships are from undetected, fast moving cruise missiles and unexpected terrorist plots. Ships are designed to keep a full operational picture of an entire battle space, so the threat of direct fire from another surface combatant or strike from an air asset is minimized. The new dangers to these ships are non-traditional war fighting scenarios such as small boat attacks when operating in port or in vulnerable situations close to shore. This close-in threat is evidenced by the attack on the USS COLE (DDG-67) in the port of Aden, Yemen on October 12, 2000.

USS COLE was performing a routine refueling operation in a protected harbor when a small vessel appearing to be a tender pulled alongside. An explosion detonated on the small vessel caused extensive damage to the ship. Unofficial estimates state that the explosive charge was equivalent to approximately 400-700 pounds of TNT. It was detonated along the waterline at a standoff distance of 0 to 10 feet from the hull. The explosion caused a 40 foot by 45 foot hole in the port side of the ship extending below the

waterline. Two longitudinal watertight subdivisions were breached, exposing the interior of the ship to fire and flooding damage well past centerline. Figure 1 is a photograph of the damage to the port side of the USS COLE, revealing the blast damage to the side hull of the ship. The resulting damage crippled the state-of-the-art Arleigh-Burke class destroyer and instigated a close look at methods of mitigating the damage caused by such attacks to Naval vessels.
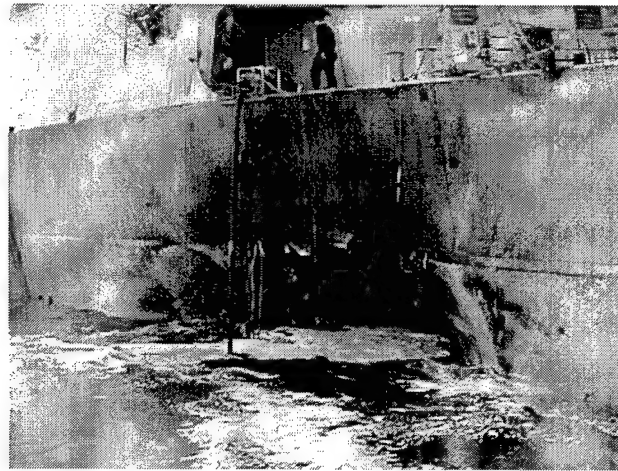
Figure 1: Port Side Damage to USS COLE (Photo from U.S. Navy Information Office)

In a case such as the explosion alongside the USS COLE, the tearing of the hull and subsequent travel of the explosive shock wave through the ship infrastructure resulted in a complete loss of power and propulsion capabilities, along with significant injury and loss of life to personnel. A method of mitigating the spread of the shock wave through the ship might have isolated the damage to the outermost spaces adjacent to the blast, protecting the inboard engineering spaces. Preserving the integrity of these vital spaces would allow continued operation of propulsion and electrical generation engines and maintain war-fighting capabilities.

Arleigh-Burke class destroyers such as USS COLE are not equipped with specific side-hull protection systems. They are designed to withstand the necessary ship loads in accordance with U.S. Navy Design Data Sheets (DDS). DDS's are design guidelines that

outline a systems-based approach to the mitigation of damage for ship structures. They were developed using classified explosive deformation and failure studies for naval vessels, empirically based on data accrued through years of live fire tests conducted by the Office of Naval Research (ONR). The blast loading guidelines in these documents are primarily concerned with protecting the ship from the stresses produced by own-ship weapons systems and hull dynamic loading. For example, there are requirements to design bulkheads and decks to withstand the loading of the overpressure from a gun barrel firing or from the impingement of missile rockets as they launch. However, there are no specific requirements for U.S. Navy ships to have armor plating or blast protection to withstand damage from outside sources other than nuclear overpressures. Blast protection or mitigation capabilities, if installed, are merely design features of the specific platform.

The next generations of U.S. Navy destroyers, DD(X), are designed with a bit more side-hull protection as a consequence of the location of their missile launchers. DD(X) has a tumblehome hull form; the sides of the hull slope inward from a maximum beam below the waterline. Vertical launch missile cells are positioned directly inboard of the side hull in this design, creating a dead space outboard of the missiles due to the slope of the hull. In order to protect the ship from damage due to unintentional detonation of the missiles housed in these launchers, current design uses reactive armor and heavy plating inboard of the launcher. This design is necessary to protect the ship, but costly in terms of space and weight.

An alternative means to partially reduce blast loading on the side hull of DD(X) could produce significant savings for the ship design. Blast mitigation would need to be performed with minimal impact on major ship systems, preferably using extensions of currently installed systems. Water mists are currently being used as fire suppression systems on the next-generation destroyer and future U.S. Naval combatants. It appears that some degree of mitigation may be achieved by proper application of water mist to a space prior to the propagation of a shock wave. Therefore, the feasibility of using water mist to mitigate blast damage must be investigated.

12

HALON Replacement and Water Mist

Current U.S. Naval combatants primarily rely on HALON-1301 as a space flooding fire protection system for vital shipboard spaces such as engine rooms. Halons are low-toxicity, chemically stable compounds that have been used for fire and explosion protection throughout this century. HALON-1301 (a gaseous agent) is used mainly in total flooding fire suppression systems. Halons have proven to be extremely effective fire suppressants, which are clean (leave no residue) and remarkably safe for human exposure. They work by breaking the chain reaction required for a fire to burn unabated.

Three things must come together at the same time to start a fire. The first ingredient is fuel (anything that can burn), the second is oxygen (normal breathing air is ample) and the last is an ignition source (high heat can cause a fire even without a spark or open flame). Traditionally, to stop a fire you need to remove one side of the triangle - the ignition, the fuel or the oxygen. Halon adds a fourth dimension to fire fighting - breaking the chain reaction. It stops the fuel, the ignition and the oxygen from dancing together by chemically reacting with them. Many people believe that Halon displaces the air out of the area it is dispensed in, but this is false. Even for the toughest hazards, less than an 8% concentration of Halon by volume is required. There is still plenty of air in the space for personnel to use during the evacuation process.

Under the Clean Air Act (CAA), the U.S. banned the production and import of virgin HALON-1301 beginning January 1, 1994 in compliance with the 1987 Montreal Protocol. The Montreal Protocol placed a ban on the production of ozone depleting substances (ODSs) for industrialized nations in January 1996. A compound's ability to destroy ozone depends on many factors, including the amount of chlorine and/or bromine that it contains. To aid them in comparing compounds, scientists have developed a relative scale called the ozone depletion potential (ODP). Chlorofluorocarbons (CFCs), the common refrigerants found in refrigerators and car air conditioners, have been assigned the value 1 as a reference. HALON-1301 has the value between 10 and 16, meaning it has 10-16 times the more potential for destroying the ozone layer. Halon use worldwide is significantly less than that of CFCs, so even though it is more damaging to the ozone layer,

13

there is not as much of it released into the atmosphere. In fact, it is estimated that overall Halons account for less than 20% of ozone depletion. Recycled Halon and inventories produced before January 1, 1994 are now the only sources of supply in the United States.

There are a number of traditional fire extinguishing agents, such as water, carbon dioxide, dry chemicals, and foam that are good alternatives to Halons for many applications. In addition, recent research has led to the commercialization of new agents and technologies. These fall into four basic categories: halocarbon compounds, inert gas mixtures, water-mist or fogging systems, and powdered aerosols. The growing list of alternatives to Halon, in conjunction with advanced detection and fire resistant materials, provides protection from a broad spectrum of potential hazards. However, matching a fire-fighting agent to the specific uses required in confined areas on combatant ships poses a difficult problem.

The Navy has attempted to identify non-ozone depleting alternatives to fill the role of HALON-1301 fire suppression systems. Many inert gas mixtures operate on the principal of oxygen displacement, quickly turning a confined space into a suffocation zone for escaping personnel. Dry chemical agents tend to be very corrosive to electronic equipment, causing significant damage in a shipboard environment. Traditional foam and water flooding systems are quite effective, but application must be limited due to stability considerations on a floating platform. Water mist systems seem to be the best-suited replacement for Halon flooding systems on U.S. Navy combatants.

The U.S. Navy has developed a machinery space water mist system that utilizes a modified high-pressure spray nozzle. According to the Commission on Physical Sciences, Mathematics, and Applications (CPSMA) (1997), the system is designed to produce high volumes of 100 µm droplet (mean diameter) sprays with very high spray momentum to achieve rapid suppression of large hydrocarbon pool or spray (Class B) fires. These nozzles emit 2 gpm at 1000 psi on a grid system. This system produces water flow application rates of $0.06 - 0.07$ gpm/ft^2, three to four times higher than commercially available systems.

14

Blast Mitigation using Water Mist

The recent trend of using fine water mist systems to replace the legacy HALON-1301 fire suppression systems warrants further study into other applications of the water mist systems. Preliminary research by the Naval Research Laboratories indicates that fine mists (20-25 μm droplet size) may reduce peak overpressures of a shock wave traveling through a space. Such pressure reductions could be used to mitigate the destructive effects of a shock wave (initiated by an explosive device) traveling through a structure. Although the mitigation effects are not observed to the same extent for droplet sizes in the 100 μm range used in the current U.S. Navy water mist system, modification to smaller nozzle apertures such as those used on many commercially available water mist systems could make such a system feasible for installation on ships.

Currently these blast mitigation effects have only been demonstrated in small-scale shock tube tests (Outa et al (1976) and Sommerfield (1985)) and computer simulations (Schwer et al (2002 & 2003)). Uncertainty exists as to the scalability of such a system. The intention of this research was to fully investigate the applicability of such a blast mitigation system for shipboard use. A theoretical study of the mechanisms of blast mitigation using water mists was undertaken to explain the phenomena and possible methods of scaling and application. Current research into water mist blast mitigation was thoroughly reviewed and examined for trends to aid in guiding the direction of future work. In addition, a study of the degree of mitigation necessary to make a system practical for shipboard installation was conducted, including a close look at the calculation of failure loads for stiffened panels.

These trends provide necessary information to begin design of a scalable blast mitigation system with applicability to real-world shipboard spaces. Given the recent trend toward tumblehome hull forms in future Naval Combatant designs, there exists strong applicability of this system in the "dead" spaces created by the shaping of the tumblehome hull. The end goal is a feasible design of a blast mitigation system to be used in the outermost spaces of Naval Combatants to protect interior vital system spaces.

15

SHOCK STRUCTURES IN GAS-PARTICLE MIXTURES

The first phase of investigating the use of water mists for blast mitigation involves studying the dynamics of the mist-air mixture in the presence of a blast or shock wave. In order to understand the phenomena observed in shock tube tests and numerical simulations, the governing dynamics of gas-particle mixtures were studied and applied to the specific case of a water mist. Although a complete theoretical explanation of the blast mitigation effects observed when a shock wave passes through a water mist – air mixture does not exist, the phenomena can be at least partially explained by further study into the dynamic interaction of pressure waves and gas-particle mixtures.

The interaction of a shock wave with a mixture of water mist and air is a complex time and space dependent process. Understanding this interaction requires the use of simplifying assumptions to identify the properties of the gas mixture. The dynamics of gas-particle mixtures are heavily studied for low Mach number processes in works such as Clift et al (1978) and Crowe et al (1998). These studies employ the basics of fluid dynamics such as the Navier-Stokes equations for slow viscous flows, modified to include particle mixtures and interactions of heat and mass transfer for particles of various shapes and sizes. Crow et al (1998) develop particle interaction models, phase equations for multi-dimensional flows, and droplet-particle cloud equations from both a Lagrangian and an Eularian approach. These equations are then used as the background for numerical modeling techniques for a variety of multi-phase flows.

Energy Methods

Part of the numerical modeling involved in the above studies includes work to model evaporating droplets in sprinkler fire suppression systems. This includes energy equation modeling for individual droplets including convective and radiative heat transfer. Heat transfer could represent a significant portion of the total energy absorption encountered in the blast mitigation process, although the time dependency of the heat transfer process is likely to limit its effects when dealing with short duration blast pulses. It

16

is speculated that the time necessary to allow for heat transfer to occur to the mist particles is significantly greater than the time for the shock front to pass. The effects of heating and vaporization of the water mist are likely to play a major role in the cooling and fire suppression achieved, but not in the mitigation of blast overpressures.

To further investigate the role of vaporization and heat transfer, an energy method was used to compare the energy required to heat and vaporize a unit volume of mist with the energy of the impinging shock wave. The heat of vaporization of fresh water is used to calculate representative energy absorption for vaporizing one cubic meter of water mist at room temperature. Appendix A contains the calculations demonstrating that for 25 μm water mist, using the U.S. Navy standard design mist concentration, 6 mega joules (MJ) of energy are required to vaporize one cubic meter of mist from room temperature. The energy of the shock wave is calculated by integrating the pressure of the wave over time and multiplying by the speed of wave propagation. In this case, the shock wave is assumed to propagate at the speed of sound. The energy of the representative shock wave used is 0.239 MJ per square meter.
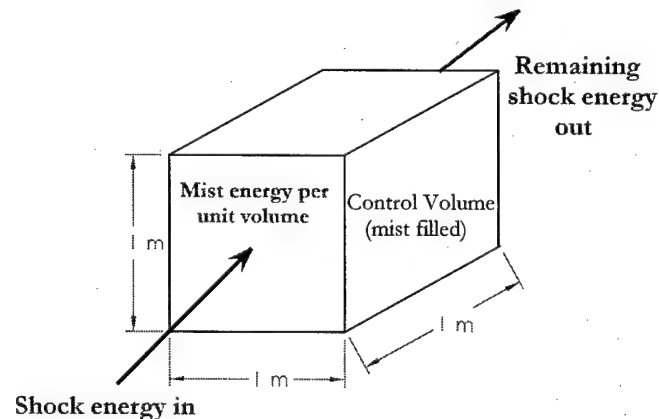
Figure 2: Simplified Energy Flux for Unit Volume

A net energy is calculated by multiplying the energy of the shock wave by the unit area over which it impinges and subtracting the energy of the unit volume of mist from this quantity. The result of this calculation is a negative energy, indicating that if the mist were

17

in fact vaporized to absorb the shock energy, the shock would be completely dissipated. Experimental results show that this is not the case, supporting the theory that the mitigation effects observed are not primarily caused by vaporization. Schwer et al (2003) provide further validation of the assumption that this vaporization energy is not a major contributor to the net mitigation effects through numerical simulations described later in this report.

Gas-Particle Dynamics

Investigation of the mechanics of shock propagation in an air-water mist mixture provides a background for understanding the mitigation achieved. Marble (1970) develops a relevant discussion of the mechanics of heterogeneous media for this study. In developing constitutive equations for mixed media, he makes a series of profound assumptions. Although each assumption is essential to the development of an analytical solution for a complex, mixed-media problem, it is likely that many of the phenomena causing the mitigation effects in water mist are eliminated from the analysis through these assumptions. Therefore, a careful look at Marble's assumptions and their repercussions is essential to understanding his development and its applicability to the problem at hand.

Marble's first major assumption is that the volume fraction of the solid-particle or droplet cloud is considered to be so small that interaction between individual particles may be neglected or simplified. Since the mass loading experienced for fine water mist is relatively small, this assumption is not likely to invalidate Marble's conclusions for this problem. Detailed transport processes between particles and gas are considered to be independent from the dynamic problem. Factors not considered in this analysis yet relevant to mist mitigation include the impact of particles on walls, and the effects of particle settling due to gravity. Marble considers the gas to behave as an ideal gas.

A viscous stress tensor exists for gas only and is considered undisturbed by the presence of the particles. The volume fraction of the particles is considered negligible. This assumption allows omitting the Einstein correction from continuity equations. Marble uses a "smoothing" assumption for the continuum variables of the gas. Gas velocities and

18

temperatures vary strongly in the immediate vicinity of a particle moving through and exchanging heat with the gas, but for the purposes of continuum equations, values are used which are averaged over a gas volume containing several particles. This assumption essentially mandates that all particle wakes and regions of immediate influence be dissipated very rapidly over the gas volume considered. The phenomena of particles forming groups and traveling in one another's wakes are not accounted for under these assumptions, although this grouping is not likely to play a major role in pressure reduction or energy absorption.

To model the processes of drag and heat transfer for a coupled particle/gas cloud, the Reynolds and Mach numbers determine a regime for the flow and the corresponding governing equations. Generally, numerical solutions are required unless the flow falls into a clear-cut regime such as Stokes flow, quadratic flow, or hypersonic flow. By limiting the analysis to a single regime, the limits of the approximation can be clearly defined and analytical solutions obtained. Marble assumes that Stokes flow and a Nusselt number of one describe particle drag and heat transfer.

Appendix B shows the derivation of the governing equations for particles of radius σ moving in a gas of viscosity μ. Included in this derivation is a definition of the characteristic time, shown in Equation 1 below. This is the time required by a particle to reduce its velocity relative to the gas by e^{-1} of its original value in an unaccelerated state.

$$\tau_v = \frac{m}{6 \cdot \pi \cdot \sigma \cdot \mu} \tag{1}$$

τ_v = characteristic time of particle
m = mass of individual particle
σ = particle radius
μ = gas viscosity

This equilibration time can be compared with the characteristic time (τ) for the flow to further characterize the gas-particle interaction. For example, if $\tau_v >> \tau$, the particle moves through the flow field in a time scale short enough that the motion of the particle does not alter appreciably. In this case, the particle motion is dictated almost exclusively by

19

its state before entering the system, independent of the properties of the gas. For the opposite case, when $\tau_v << \tau$, the particle adapts to the local motion of the gas very quickly upon entering the system and moves only a very short distance before gaining equilibrium with the gas. In this case, the particle motion is relatively independent of its previous history and largely dependent on the motion of the local gas.

The thermal behavior of the gas-particle mixture follows similar patterns to the kinetic phenomena described above. The structure of a normal shock wave exists in the region between complete equilibrium of gas and particles and the complete independence of gas and particles described above. Complete equilibrium exists both ahead of and behind the normal shock, a necessity of continuity. Therefore, conservation relations apply across the shock in terms of the modified gas properties for the gas-particle mixture described in Appendix B. The only deviation from this is that the existence of the shock structure is based on the upstream Mach number computed from the true gas properties, not the modified mixture properties.

The shock structure itself consists of a gas-dynamic shock followed by a relatively thick zone in which equilibration processes take place. In order to separate these two zones, the relaxation time of the particles must be long compared to the molecular collision time of the gas. This assumption is reasonable since relating these two time quantities involves forming a ratio of the particle substance density to the density of the base gas. For fresh water mist in air, this ratio is high enough to allow significant leeway in the other factors involved such as particle radius and mean free path yet still meet the requirements of the assumption.

Marble postulates that the gas-dynamic shock structure is unaffected by the particle cloud, though the shock may be thin relative to the particle radius. Because the volume fraction of the particles is negligible, at any time less than 1% of the shock front is being punctured by particles. Therefore, the particles pass through the shock front unaffected by the shock and retain their initial conditions upon entering the equilibration zone.

It is in this equilibration zone where Marble postulates the particles have their greatest effect. The relaxation lengths (obtained by integrating particle speed over the relaxation time) for both velocity and temperature determine the thickness of the equilibration zone. The thickness of this zone subsequently determines the shape of the exponential decay following the shock front. The generalized shape behaves as $\exp[-x/(M_3\Lambda)]$ where M_3 is the localized Mach number in the equilibration zone and Λ is the total relaxation length of the gas-particle mixture for either velocity or temperature equilibration. Solutions for Λ include a first order dependence on the relaxation length of the particles and a series of terms including a factor of η, the particle mass loading, which represent the gas-particle interaction. Figure 3 shows the spatial structure of the relaxation zone. It can be observed that the effect of the particles essentially extends the equilibration zone, allowing more time and space to dissipate the shock energy.
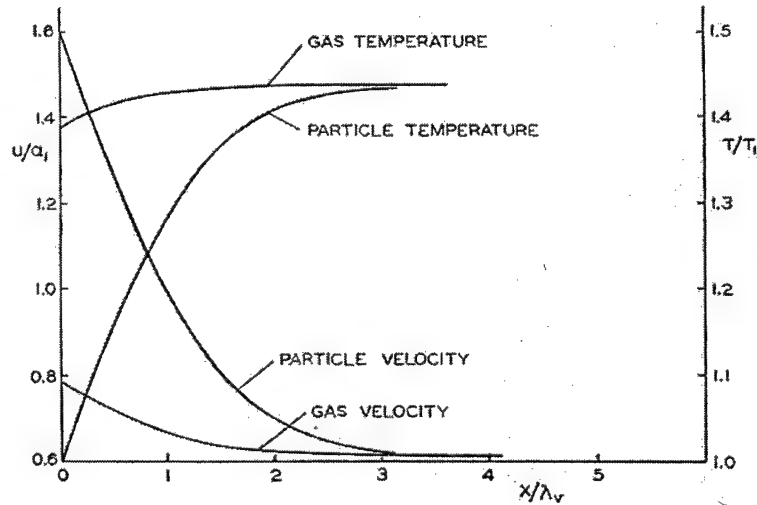
Figure 3: Spatial Structure of Shock Relaxation Zone (Marble (1970))

To this point, no consideration is given to the effect of different sized particles and collisions between particles. As long as the expected time between collisions of particles is equal to or longer than the equilibration time for the particles, a particle will essentially lose the scattering velocity obtained through a collision encounter before it experiences another

21

collision. This assumption simplifies the problem by always considering the starting conditions to be equivalent to the equilibrium slip condition.

Sommerfield (1985) discusses the decay of incident shock waves upon encountering gas-particle mixtures from both a velocity and a peak pressure standpoint. The general premise is that shock waves initiated within or propagating into a gas-particle mixture will have differing characteristics from the pure gas case due to the inertia and heat capacity of the particles. There exists a transition region as a shock wave encounters a gas-particle mixture where the velocity of the shock wave changes from the initial value to a lower, equilibrium value.

Building on the work of Marble (1970), Sommerfield also develops "equivalent gas" properties for the gas-particle mixture based on the loading ratio (by mass and specific heat) of particles to gas. Depending on the properties of the gas-particle mixture, the shock wave is refracted and reflected (as a shock or a rarefaction wave) at the interface. For the case of ship geometry and a water mist filled space, this interface coincides with a breached bulkhead or portion of ship hull, so the shock front would also be modified due to the geometry of the hull as it deforms.

The velocity equilibration zone following a shock is extended by the presence of a gas-particle mixture. Due to the heat capacity and inertia of the particle or droplets in the mixed media, the velocity of a transmitted shock wave does not change instantaneously. A transition region develops where the shock velocity is slowly reduced from its initial to its equilibrium value obtained from the equivalent gas analysis. During this deceleration process, peak pressures in the shock front are increased slightly due to basic Bernoulli flow considerations. As velocity decreases, pressure must increase to maintain equilibrium. This pressure increase occurs before equilibration of the gas-particle mixture begins to dissipate the energy of the shock front.

In terms of mitigation effects, the reduction in velocity represents a reduction in the overall strength or energy of the shock front. Although it is not instantaneous, if the

velocity of the shock is reduced prior to the next impingement on a structure, the energy of the wave on this structure is effectively reduced. However, enough time and space must elapse to allow the enhancement of peak pressures due to the shock deceleration to pass before mitigation effects take over and peak pressures are reduced. The depth of mist necessary to achieve mitigation and not enhancement must be quantitatively defined to properly design a mitigation system.

These theoretical developments help to explain the phenomena recorded from Outa et al (1976) and Sommerfield (1985) from shock tube testing. The results of these tests and numerical simulations by Schwer et al (2002 & 2003) provide background of the mitigative effects of water mist. The next section studies previously published experimental and numerical results and places them in the context of the water mist-air mixture behavior.

Experimental Results

Outa et al (1976) measure the time history of a shock wave initiated in the pure gas section of a shock tube and subsequently interacting with a dusty gas and decaying through the mixture until equilibrium is achieved. A graphical representation of the decay of the shock wave as it moves through the heterogeneous zone of a shock tube test is shown in Figure 4. The bend in the shock front on this time versus distance plot represents the slowing of the wave propagation as the mixed media is encountered.
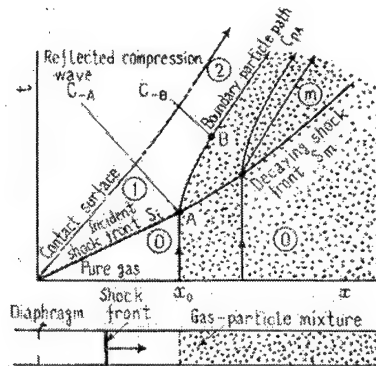
Figure 4: Wave Diagram of Shock Tube Flow Showing Decay of Incident
Shock Front Through Gas-Particle Mixture (Outa et al (1976))

23

A particle loading ratio of less than two consisting of 3-9 μm diameter white carbon particles are used in these shock tube tests. The loading ratio for the current U.S. Navy water mist fire suppression system is 2.0. Therefore, this loading ratio has good applicability to the water mist problem, although the mist droplets are significantly larger than these particles. Through testing and theoretical calculations, Outa establishes trends for the effects of particle diameter on pressure, temperature and velocity. These results are shown in Figure 5 below. The pressure plot in this figure is the most relevant to this problem. Particle sizes below 15 μm appear to delay (in a spatial sense) the arrival of the peak pressure but do not appear to cause a significant decrease in the peak pressure itself. However, for the 30 μm particle size, the pressure equilibrium value seems to be lower than for the other cases, indicating a mitigation effect.
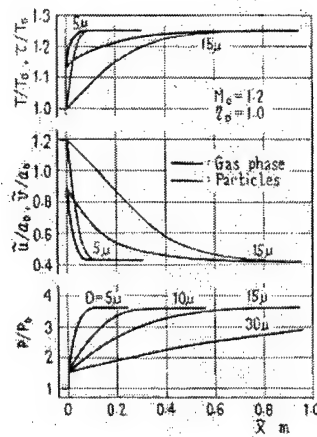
Figure 5: Effect of Particle Diameter on Temperature, Velocity, and Pressure
(Outa et al (1976))

Outa conducted shock tube tests for various mass loadings. Figure 6 shows plots of the shock as it passes various locations along the length of the seeded section of the shock tube. The traces show a discontinuity in the leading edge of the pressure trace as the shock front passes the sensor. This is representative of the steep pressure increase at the start of the shock wave. Comparing the traces along the 2 meters of shock tube accounted for by the various traces shows the weakened pressure wave passing through the gas-particle mixture. The mitigating effects of the particles are obvious from the pressure drops

24

observed between the four traces in each plot series. The total mitigation due to the mixed media is represented by the difference in the pressure between the upper left-most trace and the lower right-most trace in each row of plots. These traces are from the x locations corresponding to the start and end of the mixed-gas section of the shock tube. The three rows represent three different mass loading cases at slightly different Mach numbers. The low mass flow loading case ($\eta_o = 0.6$, top plot) shows the least mitigation, reducing the peak pressure by about 20% over the length of the test section. In contrast, the $\eta_o = 2.1$ case shows a reduction of the unmitigated shock pressure by 30%.
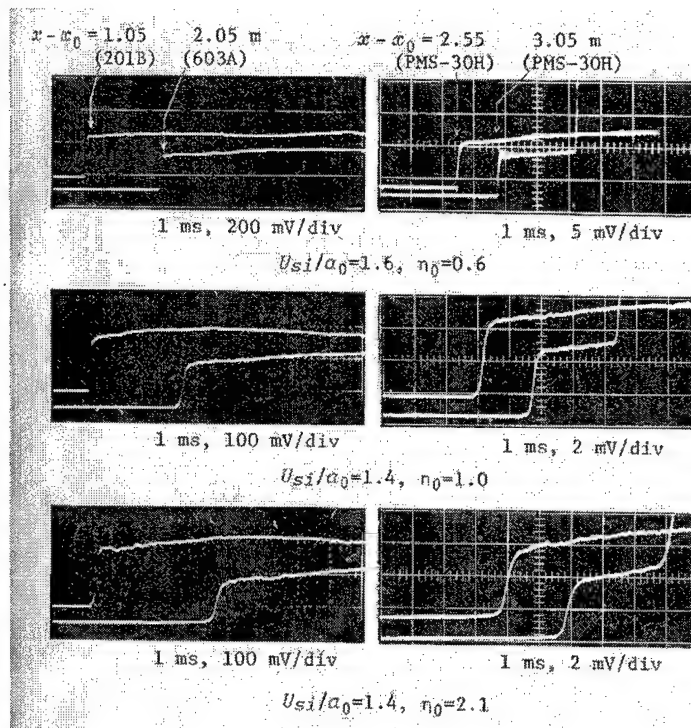
Figure 6: Pressure Traces Showing Variations of Wave Form Along Tube
(Outa et al (1976))

To better demonstrate the pressure reductions achieved by the gas-particle mixture, Outa plots the experimental results of the shock pressure against the expected, unmitigated shock structure. Figure 7 shows the experimental pressure trace and calculated stationary wave forms at a section where the leading front is still decaying. The experimental

25

pressure, as indicated by the open circles, approaches an equilibrium value behind the shock front. This pressure is significantly lower than those calculated for stationary waves. The peak pressure is again reduced by about 30% from the expected pressure prior to the shock encountering the gas-particle mixture.
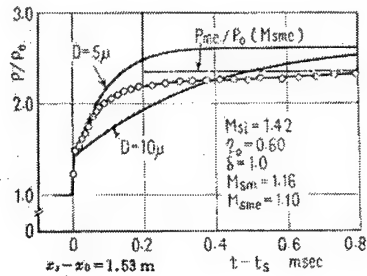
Figure 7: Experimental Pressure Trace and Calculated Wave Forms (Outa et al (1976))

Sommerfield (1985) repeats many of the experimental results presented above using a similar shock tube arrangement. These experiments were conducted using glass spheres with a median particle diameter of 27 μm rather than carbon dust as above. The particle size used by Sommerfield duplicates a feasible droplet size for water mist systems using current nozzle technology. The droplet size for a mitigation system must be optimized to achieve the desired mitigation effects for a given system design. The choice of droplet size for the proposed mitigation system will be discussed later in this report. However, it is noted at this point that the particle size used in Sommerfield's experiments corresponds directly to the proposed droplet size for a water mist mitigation system. In addition, the density of the glass spheres used is not significantly different from the density of a fresh water mist droplet. The resulting pressure traces, shown in Figures 8 and 9 below, clearly demonstrate the mitigating effects of the particle mixture used by Sommerfield.

26
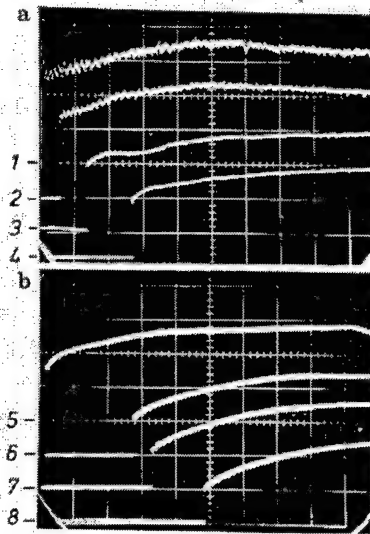
Figure 8: Pressure Traces for $M_{so} = 1.49$, $\eta = 0.63$ (Sommerfield (1985))

The first experimental results shown are for a mass loading ratio of 0.63. Figure 8 shows a total of 8 pressure traces, representing 8 locations along the seeded portion of the shock tube. The numbers on the left side of the trace show the zero mark (pre-shock pressure) for each location as a reference point. The pressure jump as the shock passes causes a sharp discontinuity in the pressure trace from this initial value to the more readily observed trace above. The first notable feature on the plot is the decay of the sharp shock front as it moves through the gas-particle mixture. This decay is even more evident in Figure 9, the results of a similar experiment at a mass loading ratio of 1.33, over double the loading shown in the previous result.
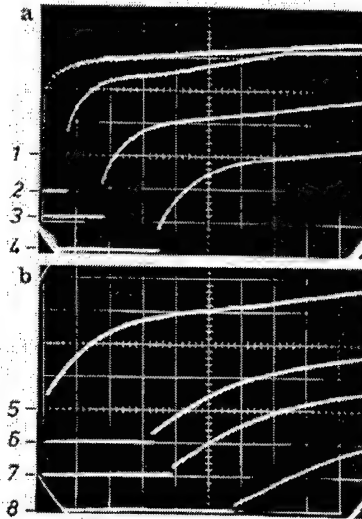
Figure 9: Pressure Traces for $M_{so} = 1.127$, $\eta = 1.33$ (Sommerfield (1985))

The decay of the shock front observed in these traces represents the effects of the deceleration of the shock wave as it encounters the gas-particle mixture. The net effect of this velocity reduction is observed in the pressure traces as a delay in the arrival of the peak overpressure from the shock. Rather than an instantaneous increase to peak pressure followed by decay as observed in a pure gas, the pressure increases more gradually in the seeded gas, resulting in a delay in the arrival of the peak pressure.

The distance between the first and last pressure gauges recorded in these plots is approximately 4 meters. The peak pressure between these traces is reduced by 28.6% for the lower mass loading case. A reduction by 20% results between the first and the 4th sensor, a distance of 1.25 meters. For the high mass loading case, the total reduction over the length of the tube is slightly lower than that for the lower mass loading case. The decay of the shape of the shock front is greater for this case, but it appears that the lower mass loading provides better overall pressure mitigation characteristics. This observation correlates to the theoretical development of the deceleration zone presented in the previous section. The higher mass loading causes more deceleration of the shock front, extending this zone of the overall structure and therefore extending the pressure enhancing zone and leaving less time for pressure mitigation to occur before the system reaches equilibrium.

28

Compared to the ratios studied by Sommerfield (η=0.63-1.33), current U.S. Navy water mist systems provide higher mass loadings (η=2.0) of water. Scaling this mass loading for blast mitigation purposes without sacrificing the back fit capability to current Navy systems is an important factor in making such a system feasible. Recognizing that the mass loading for the current Navy system is much greater than most commercial systems using smaller droplet sizes, the mass loading is recalculated based on a smaller concentration of water mist. The concentration is reduced to ¼ of the current Navy design based on data from commercial water mist systems and the reduction of the mean mist diameter applied by a factor of four from the baseline Navy design. This concentration is more representative of the mist applied through the smaller aperture nozzles needed for this droplet size. For the purposes of calculating the behavior of shock waves through a representative mist-filled space, a mass loading ratio of 0.512 is used.

Based on these experimental and theoretical calculations, mitigation on the order of 30% reduction of the peak overpressure of an impinging shock should be possible. Proper droplet size and mass loading of the water mist are essential to achieving this mitigation. For further investigation into the mitigation possibilities of water mists, numerical simulations must be used.

MITIGATION EFFECTS

As observed by Schwer and Kailasanath (2003), shock tube tests leave many unanswered questions about the behavior of seeded gases and shock fronts. In experiments where the driven section and the driver section of the shock tube are of similar size, the mitigation effects are small. The primary effects observed are a reduction in the velocity of the shock front, and a reduction of the pressure at the shock front. The overall maximum overpressure occurs slightly behind the shock front due to the deceleration of the shock and the equilibration zone behind the shock. The maximum overpressure, occurring further back in the shock structure, is initially increased in computer simulations of this setup. This effect is due to the "compression" of the shock front due to its deceleration upon impingement with the seeded gas.

The constitutive equations presented by Outa et al (1976) and Sommerfield (1985) were adapted to the specific case of the air-water mist system by Schwer et al (2003). The result of these calculations is an accurate numerical modeling tool for use in predicting the mitigation effects and behavior of a shock wave passing through an air-water mist mixture. Integrated into this simulation are the relevant factors to simulate the use of liquid droplets rather than the dry particles used in all laboratory testing to date.

Results from Schwer's simulations indicate that overall mitigation is tied to the location of the maximum overpressure. For shock waves traveling through seeded gases, the maximum overpressure location no longer coincides with the shock front location due to deceleration effects. As shown in the experimental results above, at higher mass loading ratios the sharp shock front decays, resulting in a delay in the arrival of the peak overpressure. From Schwer's numerical model, Figure 10 provides a distance-time plot showing the arrival of the shock front and the arrival of the peak pressure for a variety of particle sizes at a mass loading of 0.5. The split between location of the shock front and location of the peak overpressure is closely correlated to the particle size. Larger particles cause a longer delay of the arrival of the peak pressure in these numerical simulation results.

Schwer's numerical simulation results shown are well correlated to the pressure traces shown above. The differential in arrival time of the peak overpressure is easily observed in Figure 9, although the correlation presented by the data in Figures 8 and 9 relate to mass loading ratio, not to particle size. These two factors exhibit the largest influence on the mitigation characteristics of a mixed-media and therefore are the main design variables for creating a feasible mitigation system using water mist.
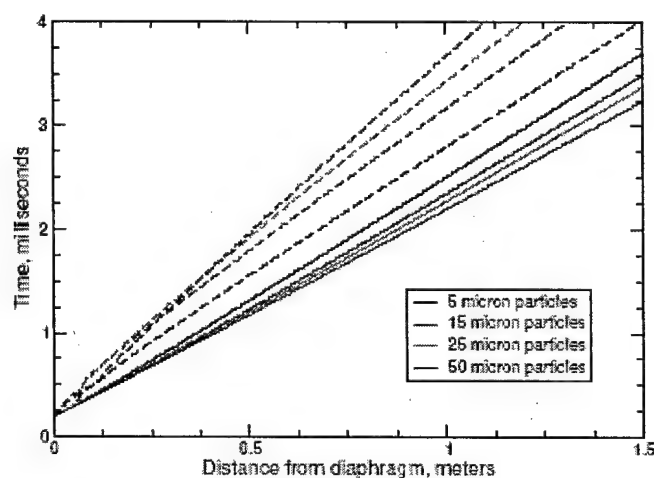
Figure 10: Location of Shock Front (solid) and Maximum Overpressure
(dashed) for Different Particle Sizes (Schwer et al (2003))

Although the effects of the seeded gas on the shock wave velocity and shock front pressure rise are obvious from these experimental and numerical results, the maximum overpressure initially increases for many cases simulated using this shock tube arrangement. It is theorized by Schwer et al (2003) that the relative sizes of the driver and driven sections of the shock tube arrangement are the root cause of this increase. The setup used has a driver section 3.5 meters in length and a driven section 4.0 meters in length, simulating a blast front of the same size as the medium through which it travels. However, explosive shocks act much more like a point load in a large medium. The driver section of a real-world explosion is significantly smaller than the surrounding, "driven" section, which experiences the effects of the shock front. Therefore, a more realistic model was simulated numerically by Schwer using a driver section $1/20^{th}$ the size of the driven section.

31

The simulations run by Schwer with this more realistic geometry demonstrate a closer correlation to the actual mitigation levels achieved in a laboratory setting. The maximum overpressure was measured for a variety of particle sizes and plotted as a function of distance along the seeded gas portion of the tube. The effects of droplet size on peak overpressure for a constant mass loading ratio are shown in Figure 11. From the plot on the left, the optimal droplet size appears to be between 20 and 40 μm, with the 40 μm droplet size beginning to exhibit a lag in the equilibration time behind the shock front. The plot on the right demonstrates that the mitigating effects of larger droplets (100 μm) such as those used in the current Navy design are not as pronounced as for the smaller droplet size.
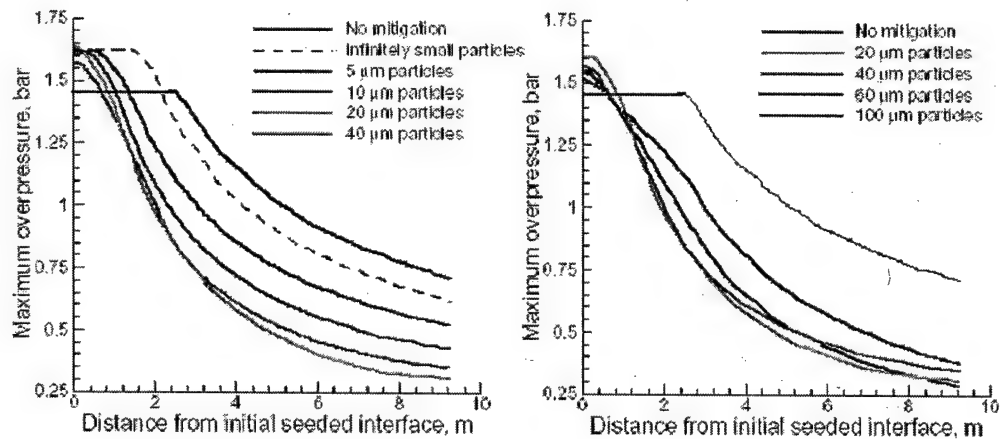
Figure 11: Snapshots of Pressure Profiles as 5 ms intervals for $M_o = 1.49$, $\eta = 0.63$ (Schwer et al (2002))

The peak pressure observed just as the shock front crosses into the mixed gas area is slightly higher than the no-particles case due to the deceleration of the shock front. However, the reduction in peak pressure as the shock front travels through the seeded gas is dramatic. For most particle sizes, the majority of the mitigation of pressure has occurred after the shock has traveled through 5 meters of the seeded mixture. The level of mitigation itself is dependent on particle size. Mitigation appears to increase with particle size to a maximum for the 25 μm particles. The results for the 60 μm particles show a

slower decay to the maximum mitigation level, although the pressure at a distance of 8 meters is nearly equal to that achieved for the 25 μm particles.

In comparing the results presented in Figure 10 to those presented in Figure 11, it appears that the overall mitigation is tied to the location of the maximum overpressure. The mitigation is achieved by a reflected rarefraction wave dissipating the shock pressure. Situations where the maximum overpressure is farther behind the shock front result in the reflected rarefraction wave dissipating the pressure sooner, allowing for greater overall mitigation. To some extent, larger droplet sizes achieve greater mitigation under these assumptions. However, these results are for a limited, shock tube geometry. The optimizations are still based on geometry and mass loading of the real-world space through which the shock wave travels and the shape and size of the initial shock. In order to investigate the dependencies of these factors, a more realistic, spherical blast equivalent to 4.67 lb of TNT was simulated by Schwer et al (2003).

The results of Schwer's simulation of this geometry for unmitigated and mitigated blasts on a time basis are shown in Figure 12. These simulations were conducted for the same mass loading (0.5) as above and for an initial droplet size of 25-30 μm. Both the time delay and pressure reduction effects of the water mist impingement are observed. The mitigation effect is not observed at the earliest time interval (125 μsec), but is obvious by the next increment (375 μsec). This plot also shows the travel of the shock wave corresponding to the time intervals. The first mitigation effects are observed on the second time interval, at a distance of 0.8 meter from the initial encounter with the seeded gas. Although this model represents a geometry not validated by laboratory experiments, it does provide a rough estimate of the depth of mist necessary to achieve mitigation effects.

33
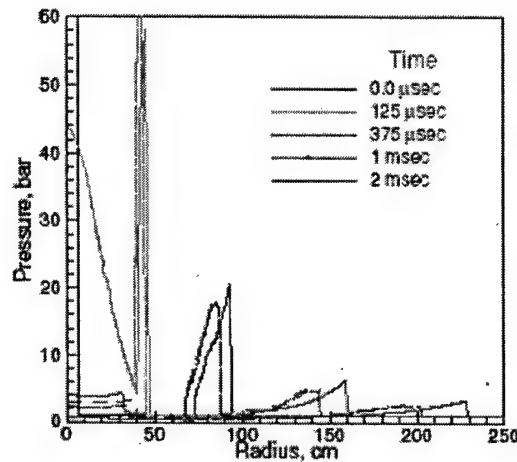
Figure 12: Blast Pressure Profile at Different Times for Unmitigated (Solid)
and Mitigated (Dashed) Tests (Schwer et al (2003))

Vaporization effects were also considered as part of Schwer's numerical simulations. The results of the simulations support the theoretical calculations from Appendix A, namely that vaporization plays a minimal role in the overall mitigation effects of the water mist. Figure 13 shows Schwer's comparison of the peak overpressures for the pure gas, the seeded gas without vaporization effects, and the seeded gas including vaporization effects. The vaporization effect does not appear at all until the shock has traveled about a meter through the seeded gas. This corresponds to the minimum time required for any heat transfer to occur from the blast wave. Although this distance also corresponds to the depth of mist required to overcome the pressure enhancement zone due to shock deceleration, the relatively small deviation from vaporization shown in Figure 13 supports the theory that the effects observed are not due primarily to vaporization. The overall blast pressure is reduced somewhat due to vaporization, but the majority of the reduction is due to momentum and energy transfer and not heat transfer and vaporization.

34
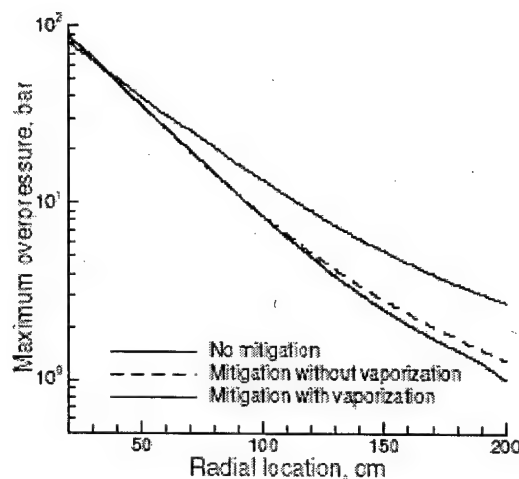
Figure 13: Maximum Overpressure Showing Effect of Vaporization (Schwer et al (2003))

The preliminary results for mitigation effects using water mist indicate that the highest degree of mitigation is achieved for mists in the range of $20 - 25$ µm mean diameter. The mass loading used also has a significant effect on the overall mitigation achieved. Experimental results show that mitigation of peak pressure is maximized for mass loadings between 0.5 and 1.0. Larger mass loadings achieve greater distortion of the shock front itself, modifying the abrupt, discontinuous pressure jump at the onset of an unmitigated shock to a more gradual build to peak pressure.

Before a mitigation system can be designed based on these optimized parameters for water mist, an understanding of the level of mitigation necessary to make a system feasible for Naval applications must be developed. The first step in this process is to look at the structure of ship hulls and bulkheads and develop a representative blast load to be mitigated. The next chapter develops and analysis of the blast resistance of stiffened panels and provides a background for quantifying the level of mitigation needed.

BLAST RESISTANCE OF STIFFENED PANELS

Blast effects are intimately connected to the structural design of warships. Navy design guidelines lay forth requirements to withstand certain levels of static and dynamic loading on various portions of a ship structure. Although resistance to blast from outside sources other than underwater and nuclear explosion is not strictly defined for all U.S. Navy ships, a fundamental and detailed understanding of shock wave loading and the associated structural response of the ship is required for effective warship design. In addition to aiding in proper design of warships, a full understanding of the behavior of ship structures to blast loading defines the role that a mitigation system might play. The level of mitigation necessary to make such a system practical is determined by the reduction in loading required to maintain the integrity of the ship.

Analysis of the behavior of a floating, multi-degree-of-freedom system such as a ship under blast loading is best accomplished through study of live fire data. The late 1940 s produced a number of landmark studies into the failure of ships under explosive force. The experiences of two World Wars provided ample data on torpedo attack and underwater explosions. Taylor (1948) and Cole (1948) conducted comprehensive analyses of submerged blast waves and their effects on thin plates. Their research formed the technical basis of all current blast damage prediction methods. Although most subsequent research into this failure mode, conducted by ONR, has been classified confidential, open-source study has been conducted on blast loading of steel structures and stiffened panels.

Nonaka (2000) looked at shear failure of steel beams and concrete structures using the World Trade Center bombing in February 1993 as an example. Rudrapatna et al (1999 and 2000) conducted blast loading tests of square plates and small, stiffened plates. These tests provided background for the possible deflection modes of a larger scale stiffened panels. Shin et al (2003) defined design guidelines for explosive confinements using analysis of shock transmission and reflection, important to understanding the proper loading to apply in the context of this problem. Schleyer et al (2000) provided background on numerical

36

modeling of pulse pressure loading. Ramajeyathilagam et al (2000) provided shock pressure pulse loading models including equations for the shape of the time dependent pressure pulse, peak pressure, and decay constant based on the weight of explosive. Nurick et al (1995) studied deformation and tearing for small square plates with a single stiffener milled into the test sample. Again, this study provided a good idea of mode shapes for larger scale stiffened panel deflection. Klaus (1985) looked at numerical modeling of panel walls subject to blast loading. Finally, Houlston et al (1985) developed and validated finite element models for blast loading of stiffened panels by comparison to experimental work done on blast loaded square plates. Houlston's work is quite relevant to this study, although only carries the analysis to plastic deflections, not to full failure of a panel.

The behaviors of plates, stiffened panels, and other steel structures have been extensively documented through this substantial body of literature. Ship structures are comprised of stiffened panels, composed of steel plate with evenly spaced steel stiffeners in the longitudinal direction. Larger structural members such as girders and frames support each panel. For the particular case looked at here, the confining end conditions will be at the frames and girders and the panel affected will be a stiffened panel with uniform size stiffeners. These assumptions are reasonable considering the fabrication of typical naval combatants. Specific panel geometries installed on representative ships are presented in a later section of this report.

When transverse loading of any kind is applied to such a stiffened panel, the panel will deflect to support the load as expected by statics and Hooke's Law. The dynamics of blast loading conditions modify the behavior of the panel; time dependencies and impulse effects become factors in the deformation and yield characteristics of the panel. Regardless of the dynamics of the problem, the yield behavior of the material will have certain ramifications on the panel deformation.

As part of the panel yields, it can no longer support shear stresses and bending moments. The stresses and moments on the panel are therefore transferred outward to the non-yielding portion of the panel until the energy of the blast wave is absorbed or reflected.

37

The yield zone continues to grow until this equilibrium is achieved. Stiffeners or girders will slow the spread of the yielding zone since they will require greater stress concentrations to yield and will absorb more strain energy in yielding.

Despite understanding the yield mechanisms and dependencies of the problem, no simple, reliable method of predicting hull plate blast damage has been developed. Although computer codes for the prediction of blast damage are available, most codes provide prediction of elastic and plastic deformation only. Prediction of fracture onset and propagation is not well validated against actual results, so the codes provide little more than a rough estimate of potential damage. As a result, nearly all of the definitive blast damage prediction is conducted using scaled, live fire tests, requiring substantial time and resources. For the purposes of this study, prediction of the overpressure required to fail a bulkhead or boundary is necessary. In order to make such a prediction, "failure" itself must be quantitatively defined.

Once the definition of failure is understood, the loading that causes this level of damage must be defined. Prediction of the level of blast loading a structure can withstand is central to understanding the level of mitigation necessary to preserve the integrity of the structure. To establish a clear criterion for the level of mitigation to be achieved, a representative blast load must be analyzed and compared to the loading that the ship structure can resist. The shock loading created by various explosives is well defined in open-source literature. Therefore, with information on loading and failure mechanisms of ship structures and data on the potential blast loads encountered, the level of mitigation that must occur to prevent failure can be defined.

A confined space mitigation system such as water mist is not likely to prevent damage to the outer hull of a ship. The goal is to protect the next layer of watertight boundaries in the ship to prevent the spread of damage. Confined space geometries provide added challenges to determining the actual level of blast overpressure propagating through the space. This phenomenon has been studied in open-source literature for blast mitigation in civilian, land-based structures. Explosions confined by a chamber or room

38

result in rapidly increasing gas pressures, which eventually decay by venting out of either a newly breached bulkhead or through the entry point. Under these conditions, shock reflections occur such that the overall effect can be greater than the incident shock.

A study must be undertaken as to the dynamic pressure (blast) loading that typical U.S. Navy ship's interior bulkheads and decks can withstand. The underlying assumption in this study is that preserving the integrity of a bulkhead or deck minimizes the spread of damage past that boundary. Prevention of first yield, however, is a very conservative, unrealistic expectation when dealing with blast loading. Mere plastic deformation does not define failure in this sense. Significant (macroscopic) tearing or cracking of the plate or weldment material will be considered failure for the purposes of this study. Under this definition, the boundary in question will no longer be watertight or structurally sound. Full buckling of a panel would also be considered failure since the boundary could no longer provide resistance to normal ship loads. Buckling in this sense is likely accompanied by cracks or fractures along the panel edges and therefore is included in the definition above.

Blast Load Prediction

The first step in determining the level of mitigation necessary to preserve the integrity of boundaries is to determine the blast profile to be resisted. This profile consists of three major components: duration of overpressure phase, peak overpressure, and impulse magnitude. For explosions close to the target, pressure-driven effects occur quickly. The characteristic duration of a high explosive detonation is measured in microseconds (10^{-6}). The pressure-driven effects of such an explosion occur on similar time scales.

Air-blast loading associated with explosions is commonly subdivided into (1) loading due to the impinging shock front, its reflections, and the greatly increased static pressure behind the front, all commonly known as overpressure; and (2) the dynamic pressures due to the particle velocity and mass transfer of the air. Pressure loadings are customarily characterized in terms of scaled range, given by:

$$Z = R/W^{1/3} \qquad (2)$$

Z = scaled range
R = radial distance between explosion center and target
W = explosive weight (TNT equivalent)

Units for charge weight and distance in this expression should be either pounds and feet or kilograms and meters. Using this scaled range factor, constant values of Z result in constant parameters for explosive effects (peak pressure, positive duration, etc.).

The explosive effects parameters such as peak pressure and positive duration are dependent on the size and type of the explosive. However, characterization of the shape of the blast profile is somewhat standard and often parameterized. For the purposes of this study, the preliminary estimates of the blast loading encountered by USS COLE will be used as a representative case.

Appendix C contains calculations for a 500 kilogram TNT equivalent explosion at a standoff distance of 10 meters using various methods for parameterizing the blast loading. The time and distance dependent shape of the actual pressure profile of the shock wave is an important parameter to understanding the blast loading to apply to a panel. The shape of the incident wave is given by Taylor (1941) as:

$$P_i = P_o \, e^{-n(t-x/c)} \qquad (3)$$

Pi = pressure in incident wave
Po = peak overpressure
t = time elapsed
x = distance from blast center, measured perpendicular to impinging plate

This shape reflects an exponential decay from the peak overpressure based on both time elapsed since the blast and distance from the blast center. The empirical constant n in Equation 3 is a decay constant representing the nature of the decay. Ramajeyathilagam et al (2000) give an empirical equation for calculating the inverse of this decay constant ($\Theta = 1/n$) as follows:

40

$$\theta(R, W) := 92.5 \cdot W^{\frac{1}{3}} \cdot \left(\frac{W^{\frac{1}{3}}}{R} \right)^{-0.22}$$

(4)

W = charge weight (kg TNT)
R = radial stand-off distance (m)

The peak overpressure used to determine the shape of the incident wave can be calculated using empirical formulae or charts as shown in Appendix C. Nonaka (2000) calculates peak overpressure using a log-based empirical formula and an equivalent mass of Sinkiri Dynamite. The resulting overpressure for the representative 500 lb TNT explosive is 130.3 psi or 89,850 Pa. Remennikov, A. (2004) uses the scaled range (see Equation 2, above) as an input to a graphical representation of various blast parameters (Figure 14). The resulting overpressure is approximately 145 psi or 10^6 Pa. Given the error inherent in reading values off the log-log graph shown in Figure 14, these results are remarkably close to those calculated using Nonaka's empirical formula. Ramajeyathilagam, K. et al (2000) use an empirical constant multiplied by the cube root of the scaled range (Z). This calculation returns an overpressure of 7000 psi, over two orders of magnitude greater than Nonaka's formulation. It is believed that there is an error in the empirical constant used in this formulation, resulting in this drastic difference.
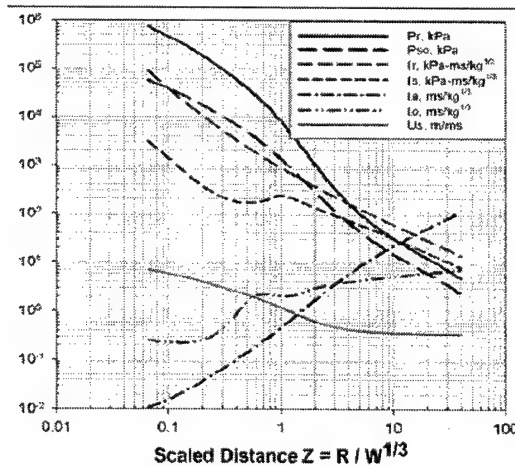

Figure 14: Blast Parameters Based on Scaled Distance

41

For the purposes of this report, the overpressure used to calculate loading on ship structures will be 130.3 psi with a positive phase pulse duration of 0.2 thousandths of a second. To simplify the loading used for theoretical calculations, this pulse was assumed to be a square pulse of constant pressure over the positive phase duration. Although this square pulse is an accurate model of the leading edge of a normal shock structure, the decay experienced in this sharp discontinuity due to the mist mixture is not accounted for. The effect of the shape change in the shock front is minimal on the way the shock is applied to the structure for analysis. The dynamic effects modeled in this study accounted for a short duration pulse at peak pressure. The time duration of the pulse itself is not significantly altered by the change in shape of the shock, so the effects of this change are negligible.

The shock described is the loading desired to be resisted by a ship structure for the purposes of this report. The remaining problem in determining the mitigation level needed is to define what level of shock will cause failure of a ship's structure. The first step in developing an answer to this question is to understand how ship subdivisions are designed in current practice.

Naval Design Standards

When the structural arrangements of ships are designed, bulkheads and decks are designed to withstand the typical global and local loads applied to them without yield. These loads are due to large-scale ship motions such as hogging and sagging, weather conditions such as icing and green water, hydrostatic pressure on the hull, and the weight of equipment and payloads. Combatants must also comply with a series of Design Data Sheets (DDS's) and with the General Specifications for Ships of the United States Navy (Gen Specs). DDS's are design guidelines that outline a systems-based approach to the mitigation of damage. Specific DDS's relevant to ship survivability and structural design include: DDS 072-1 (1972) "Shock design values," DDS 072-3 (1988) "Conventional weapons protection (fragments)," DDS 072-4 (1986) "Hull, mechanical, and electrical systems survivability," DDS 072-6 (1987) "Shaped charge warhead weapon effects data," DDS 072-7 (1988) "Conventional airblast (proximity)," DDS 072-8 (1986) "Conventional airblast (contact and internal) design and analysis methodology," DDS 079-1 (1975)

"Stability and buoyancy of U.S. Naval surface ships," DDS 100-4 (1982) "Strength of structural members," DDS 100-6 (1987) "Longitudinal strength calculation," DDS 100-7 (1984) "Structure to resist weapons firing effects," and DDS 100-9 (1991) "Nuclear airblast design for surface ship structures." DDS's 072-1, 072-3, 072-6, 072-7, and 072-8 are classified Confidential and therefore cannot be further discussed in this study. They set forth some of the major design criteria for blast loading on ship structures and therefore in many respects define the strength of ship boundaries. Although the design guidelines themselves are classified, the resulting structures of current surface combatants provide a good example of the type of structure that fulfills the requirements of the DDS's.

Most of the requirements set forth in the unclassified design guidelines are general in nature. For example, DDS 072-4 defines three major design principles for HM&E survivability: separation of redundant systems, isolation of non-redundant systems, and concentration, localization and shielding/armoring of vital non-redundant systems from areas of potential hazard. It then lays forth a 5-step procedure for designing a total system for redundancy and separation, two of the key survivability characteristics. DDS 079-1 contains key parameters for proper stability characteristics dependent on ship type and mission. It defines requirements for parameters such as intact and damaged heel and trim angles and righting arm curves in various conditions.

DDS 100-4 characterizes some important factors for stiffened panel calculations that are relevant to this study. First, it delineates a method of calculating buckling loads of plating panels under combined compressive and shear loading. It also identifies the Navy standard strength curves for selected common hull materials. These curves include column strength, ultimate compressive strength, and strength under combined compressive and shear loads for high strength steel (HS) and ordinary steel (OS).

DDS 100-7 and the Gen Specs define requirements for hull structures based on the proximity of the structure to own ship's weapons systems. For example, these guidelines set forth an empirical formula relating a static equivalent pressure to the booster motor thrust, angle of incidence, and area of impingement for missile blast loading from a

43

missile being launched from own-ship launchers. The intention of these guidelines was to protect ship bulkheads from the blast loads experienced behind the Mark 26 deck-mounted missile launcher. Although these launchers have been phased out of US Naval platforms in favor of the in-hull Vertical Launch System (VLS), the empirical calculation of equivalent static head pressure based on rocket blast loading is a useful tool. The DDS defines the static equivalent pressure applied by a missile launch as:

$$P = \frac{T \cdot \left(\sin(\alpha) + \frac{0.0225}{\sin(\alpha)} \right)}{A} \tag{5}$$

P = static equivalent pressure (psi)
T = total thrust of missile (lbs)
α = angle of incidence (deg)
A = impingement area of surface (in^2)

Equation 5 is not a direct function of distance from the missile to the bulkhead or deck in question; the area of impingement is calculated based on the projected area of a 3° divergence blast cone from the axis of the missile to the surface. Therefore, the distance is accounted for by documenting the impingement area and angle of incidence of the blast load to the surface in question. As the distance from the missile increases, this projected area also increases, reducing the static equivalent pressure experienced.

DDS 100-7 also provides guidelines for plate panel design to withstand the equivalent pressures of missile and gun blasts. Empirical formulas and tabulated values of the relevant constants are provided for two loading cases. The formulas are developed assuming simply supported edges on the plates. Plate dimensions are determined by the locations of stiffeners and girders. The first loading case assumes that the blast load is uniform over the entire plate, indicating that the impingement area is larger than the area of plating between stiffeners. The second loading case assumes a more concentrated load in a central rectangular area of the larger plate section.

Similar expressions are developed for gun blast loads based on the geometry from the structure being assessed to the gun muzzle and on the caliber of the gun itself. DDS

100-7 also delineates a method for design of deck and bulkhead stiffeners once the loading is understood. It treats the stiffeners as pinned-pinned beams, therefore rendering panel stiffeners as non-continuous members. If panel stiffeners are considered continuous, some level of fixity could be assumed for the end conditions. The maximum moment in the stiffener is calculated assuming either a uniform or a concentrated load condition. Under a uniform load condition, the required section modulus equals the maximum moment over the maximum allowable stress. This maximum moment is calculated as shown in Equations 6 and 7.

$$W = P \cdot n \tag{6}$$

$$M = \frac{W \cdot L^2}{8} \tag{7}$$

W = distributed load on stiffener (lbf)
P = static equivalent blast pressure (psi)
n = length of minor axis of impingement area (in)
L = stiffener length (in)

For a concentrated load case, the force applied is calculated as the static equivalent pressure times the area over which it is applied, similar to the formulation in Equation 6. This force is then applied as a point force at a pre-determined location along the stiffener. The maximum moment is defined using the distances from the load to each of the pinned ends times the force over the length. This point load method is a very conservative approach to design where the blast impingement area is significantly less than the stiffener length. It is much more common to assume the blast to be uniformly distributed over the stiffener for blast loadings.

Design of major supporting structures such as girders follow similar procedures to those for stiffeners. Again, structural members are conservatively assumed to have pinned connections at support points and are subjected to either uniform or concentrated loads depending on the geometry of the blast zone.

DDS 100-9 defines a procedure for "the design of surface ship structure to resist in-air, non-contact tactical nuclear weapons explosions of low- to medium-yield." This design guideline is based on a blast and shock wave originating just above the water surface

45

with the blast wave front perpendicular to the water surface. The ship structure, including intermediate stiffeners between girders, frames, and transverse bulkheads, is designed to support the reflected overpressure from a blast and to resist the shearing, tearing, buckling, or collapse loads that exist on various faces of a structure as a blast load passes over it. The reflected overpressure is the resulting pressure occurring when the incident overpressure wave strikes a surface parallel to the blast front and is reflected. This pressure includes the incident overpressure plus the instantaneous pressure loading of the reflected shock front. DDS 100-9 uses a closed box as its global structural model and therefore looks at loads resulting on all outward faces of this structure as the blast travels over and around it. The maximum loading will occur when a blast impinges perpendicular to a panel. This loading represents the relevant load case for the stiffened panel problem presented in this chapter. Although this report primarily focuses on conventional blast loading, the shock wave formation of a conventional blast is not significantly different from that of a larger, nuclear blast at greater stand-off distances.

Empirical formulas are provided in DDS 100-9 for the peak reflected pressure and stagnation pressure a structure must withstand. These pressures are calculated based on the peak incident overpressure in the shock and the ambient pressure of the surrounding atmosphere as shown in Equations 8a, 8b, and 8c.

$$P_r = 2 \cdot P_o \cdot \left(\frac{7 \cdot P_a + 4 \cdot P_o}{7 \cdot P_a + P_o} \right) \qquad q_0 = \frac{5}{2} \cdot \left(\frac{P_o^2}{7 \cdot P_a + P_o} \right) \qquad P_s = P_o + q_0 \qquad (8\ a,b,c)$$

P_r = maximum reflected overpressure (psi)
P_o = peak incident overpressure (psi)
P_a = ambient atmospheric pressure (psi)
q_o = dynamic pressure (psi)
P_s = stagnation pressure (psi)

The dynamic pressure referred to in Equations 8 a, b, and c is the result of the gross violent movement of air associated with the blast wind. It is smaller in magnitude than the blast wind itself when the incident overpressure is less than 70 psi, but is additive to the incident overpressure on vertical surfaces. Therefore, the stagnation pressure is equal to the peak incident overpressure plus the dynamic pressure, as shown above.

46

DDS 100-9 also lays out guidelines and empirical equations for calculating the beam resistance provided by a given plate-stiffener combination (stiffened panel). It uses the geometry of the plate and stiffeners to determine plastic section moduli at the mid-span and at the support. These moduli then combine with the dynamic yield stress of the material and the length of the stiffened panel to provide an overall resistance. The resistance of the overall stiffened panel is given as follows:

$$R_p = \frac{8 \cdot \sigma_{dy}}{L} \cdot \left(Z_{PS} + Z_{PM}\right)$$

(9)

R_p = panel resistance (lbf)
σ_{dy} = dynamic yield stress (psi)
L = length of stiffener (in)
Z_{PS} = plastic section modulus at support (in^3)
Z_{PM} = plastic section modulus at mid-span (in^3)

The yield stress used in this equation is a dynamic yield stress, including accounting for allowable plastic flow and dynamic load effects. It will be discussed further in the next section of this report. This intrinsic resistance of the stiffened panel is then compared with the resistance necessary to withstand the desired blast loading. The required plastic load resistance for the blast is determined by applying the stagnation pressure (see Equation (8c)) over the breadth and length of the stiffened panel and dividing by an empirical force factor. This empirical factor is dependent on the natural period of the stiffener, the duration of the positive phase pressure pulse, and the ductility factor (μ). The ductility factor is a dimensionless quantity determined in ship specifications that represents the amount of permanent set or plastic deformation that is allowable for various portions of the ship structure under blast loading. Equation 10 shows the formula for determining the normalizing force factor for the required plastic load resistance.

$$F_1 = \frac{T_n}{\pi \cdot \tau} \cdot \left(2 \cdot \mu - 1\right)^{0.5} + \frac{2 \cdot \mu - 1}{2 \cdot \mu \cdot \left[1 + \left(0.7 \cdot \frac{T_n}{\tau}\right)\right]}$$

(10)

F_1 = empirical factor for normalizing plastic load resistance
T_n = natural period of stiffener (sec)
τ = positive phase duration (sec)
μ = ductility factor (dimensionless)

47

The major design parameter for the stiffened panel is that its intrinsic resistance be greater than the required plastic load resistance for a blast designated in the ship design specifications.

All of these design guidelines provide preliminary rules for current ship structural design. In addition to serving as a design tool to derive required plate thicknesses and stiffener moduli, the empirical relationships developed can also be used to evaluate existing structures. By reversing the design procedures, an existing panel can be analyzed to determine the blast pressure loading it can resist without failure. This method will be discussed further in following sections of this report.

Beam Theory and Dynamic Loading

Thus far, the methods of calculating the allowable loading on a stiffened panel have been empirical, derived from live fire data. To validate these results, an extensive study of the dynamic load limit of a stiffened panel was completed. The first step in this theoretical analysis was to define the maximum allowable stress in the panel before it is considered to have failed. As discussed, first yield is far too conservative a measure when blast loading is considered. First yield is defined as the elastic limit of a material, or the stress at which permanent deflection will result upon unloading. This point can be observed as the first knuckle in the stress-strain curve for steel shown in Figure 15. Due to the shape of a typical stress-strain curve for metals, a significant amount of plastic deformation can occur before the material approaches its fracture point. Strain hardening occurs during the first phase of this plastic deformation, such that the material is able to withstand still-increasing amounts of stress. The ultimate tensile strength of the material is defined as the highest stress the material can resist, corresponding to the highest point on the curve in Figure 15. Once this ultimate tensile strength is reached, the material continues to strain to fracture with no increase in applied stress. Since these results are obtained for an idealized specimen in a laboratory setting, using the ultimate tensile strength would be a bit risky as a measure of the fracture point of the material. Therefore, a quantity referred to as flow stress is used to indicate a representative stress for probable fracture.

48
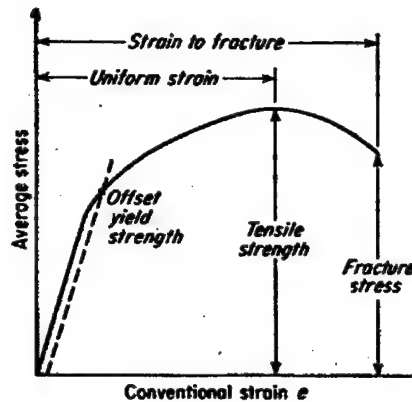
Figure 15: Typical Stress-Strain Curve for Steel

Flow stress equals the average between the yield stress and the ultimate tensile strength for ductile materials such as steel. It represents a stress high enough that continued increase in applied stress is likely to cause flowing plastic deformation and therefore lead to collapse or fracture of the material. The flow stress, σ_o, is used throughout the analysis presented here to represent the degree of stress that represents failure in a stiffened panel.

In order to analyze panel geometry for plastic collapse, the bending moment representing the collapse condition must be defined. Jones (1997) defines the plastic collapse moment of any solid rectangular cross section as:

$$M_o = \frac{\sigma \cdot B \cdot H^2}{4}$$

(11)

Mo = plastic collapse moment
σ = stress
B = breadth of plate
H = thickness of plate

For the case examined here, the stress used in this formulation of plastic collapse moment is the flow stress. This moment is equated with the maximum internal moment across the breadth of the stiffened panel, a function of the loading. Solving for the load gives the maximum pressure the stiffened panel can support before plastic collapse.

49

Looking at a simplified geometry of the stiffened panel and treating it as a deep beam allow calculation of the internal moment as a function of loading. In two dimensions, the panel is modeled as a beam supported at the ends by large structural members such as girders. A single stiffener was added at the center of the beam to represent the supports on the panel. Actual panels encompass multiple stiffeners, but to simplify the mode shape and loading for this first estimate, a single stiffener case was used. A dishing mode shape was assumed for this simplified structure as shown in Figure 16. Based on the assumed deflected shape of the structure, the center section of the beam was modeled to better define the boundary conditions. This modeled portion was cut at the zero-slope point of the deflected shape to allow modeling by a fully clamped end condition.
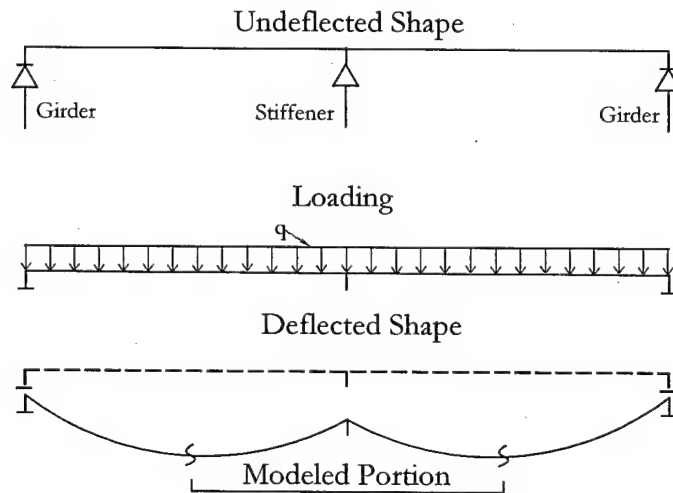
Figure 16: Simplified Stiffened Panel Mode Shape

The modeled portion of the beam shown above was approximated as a two-dimensional beam with clamped end conditions to enforce the zero-slope deflection at this point. To properly represent the reaction forces on this modeled beam, the reaction force at the stiffener was assumed to carry the entire distributed load for the length of the modeled portion. The portions of the distributed load applied to the left and right of the modeled section of panel were assumed to be supported by the girders (or stiffeners) on

either end of the panel. This loading model represents a worst-case scenario where the stiffener is modeled as a large point load at the center of the beam. Figure 17 is a graphical representation of this model.
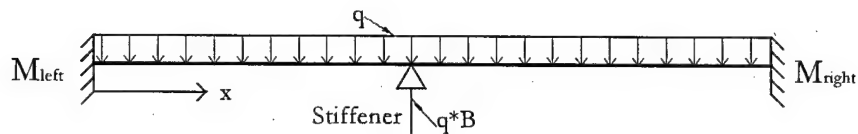
Figure 17: Modeled Portion of Stiffened Panel

Superposition of the uniform load and point load cases from beam tables allow calculation of the total moment on the beam as a function of x-location. The development of this total moment is shown in Appendix E. The representative geometry and loading case used in the first section of Appendix E demonstrates the location of the maximum moment. As can be seen in Figure 18, the maximum moment occurs at the point of inflection produced (in both the deflection and the moment diagrams) at the point load representing the stiffener. For this simplified panel geometry, the maximum moment is located at the mid-span of the beam. Therefore, the exact moment at this point along the beam can be calculated and equated to the plastic collapse moment for the stiffened panel to solve for the maximum loading.

Figure 18: Bending Moment in Modeled Stiffened Panel

51

The remaining two sections of Appendix E show the calculation of the maximum load supported by a stiffened panel as installed on the DDG-51 class and DD(X) class ships. Further discussion of the geometry of a representative stiffened panel for each platform is included in the next section of this report. Using the method described, the maximum uniform load, q, is determined for each geometry. Since the end goal of this calculation is a determina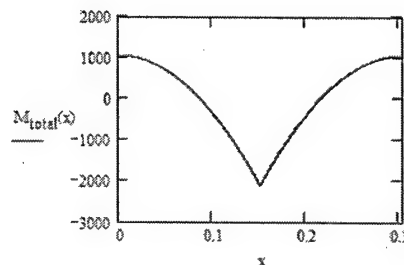tion of the static pressure the panel can resist, this uniform load is divided by the length of the panel to re-introduce the third dimension to the problem and provide a result in terms of static pressure.

This solution to the stiffened panel problem does not include any time-dependent or dynamic effects. Shock waves from blast loading propagate on a very short (microsecond) time scale. The positive pressure phase from the shock is only applied to the panel for approximately 2×10^{-4} seconds, and the peak pressure calculated in the section above represents the instantaneous maximum pressure reached during this positive phase. Therefore, the effects of dynamic loading must be considered when studying blast effects.

The problem of the dynamic load condition can be modeled using some common strain-rate inclusion formulas such as the Cowper-Symonds relation (Equation 12). This relation outputs a "corrected" dynamic yield stress from input parameters including the static yield stress, the strain rate, and material constants. The strain to fracture or rupture of steel is used in this case to represent the desired maximum deflection for the panel. This strain is applied over the time period of the positive phase of shock pressure to obtain a strain rate. Empirical constants representing the material properties of steel are included in the relation. Strain rates typical for achieving the fracture strain in steel over the time period characteristic of a blast load will increase this dynamic yield stress by a factor of two.

$$\sigma_{odyn} := \sigma_{og} \cdot \left[1 + \left(\frac{\varepsilon_{dot}}{D} \right)^{\frac{1}{n}} \right]$$

(12)

σ_{odyn} = dynamic yield stress
σ_{og} = plastic flow stress
ε_{dot} = strain rate (= rupture strain/pulse time)

52

$$D = \text{material constant } (= 40 \text{ Hz for steel})$$
$$n = \text{material constant } (= 5 \text{ for steel})$$

The Cowper-Symonds relation is typically used to modify yield stress to include dynamic considerations. In this case, plastic flow stress is used in place of yield stress to represent the fracture condition imposed for this problem. It is unknown how these strain rates will affect the plastic flow stress of the material. It is possible that the steel will become effectively more brittle as a result of the high strain rate, therefore decreasing the fracture stress of the steel. Since calculations for plastic collapse moments are all based on the plastic flow stress, this is the important parameter to consider strain rate effects on. Plastic flow stress is calculated as a numerical average between the yield and fracture stresses for the material and therefore could likely remain close to constant under high strain-rate conditions.

According to Brokenbrough and Johnson (1974), strain rate effects are also temperature dependent. For temperatures from −50°F to room temperature, increasing strain rate increases both yield strength and tensile strength in most steels, including high strength alloys and heat treated steels. However, at high temperatures (600°F) these effects are quite different. Increasing strain rate at high temperatures has very little effect on the initial yield strength of most steels. At the same high temperature, the ultimate tensile strength of all steels tested actually decreases with increasing strain rate. This is an interesting point to notice since many blast loads involve significant heat output as well as shock propagation. For the purposes of this study, however, it is assumed that the shock front propagates much faster than the heat from the blast can transfer to the steel. The thermal conductivity of air is approximately 0.024 Joules per meter-second-°Celcius and the thermal conductivity of steel is approximately 46 J/(m s °C). Based on these values, a minute amount of blast heat will have conducted from the air to the steel of the ship structure. Uniform heating effects such as those described above will not be a factor since heat would have to transfer to and through the steel material before these strain rate effects would be observed. Since the rate of heat transfer from air to steel is much slower than the shock front propagation, these high temperature effects can be neglected. Therefore, the assumption that both yield and tensile strengths increase with strain rate holds.

53

Plastic Collapse of Plates and Stiffened Panels

To achieve more accurate results for the stiffened panel problem, Jones (1997) derives upper and lower bounds for a variety of panels and boundary conditions. The derivation of these bounds for a sample geometry is presented in Appendix F. The lower bound for a simply supported rectangular plate is calculated by deriving the bending moments in the x, y and cross directions and substituting these into Equation 13, the governing differential equation of equilibrium for the plate. Solving for p in this expression gives the static pressure to plastic collapse.

$$\frac{\partial^2}{\partial x^2}M_x + 2 \cdot \frac{\partial}{\partial x}\frac{\partial}{\partial y}M_{xy} + \frac{\partial^2}{\partial y^2}M_y + p = 0 \qquad (13)$$

The upper bound for the simply supported case is developed using a kinematically admissible transverse velocity profile. This profile, shown in Figure 19, assumes that regions I and II remain rigid, with plastic flow concentrated in the plastic hinges that form at the region boundaries. The admissibility of this profile is supported by observed failure modes in laboratory testing.
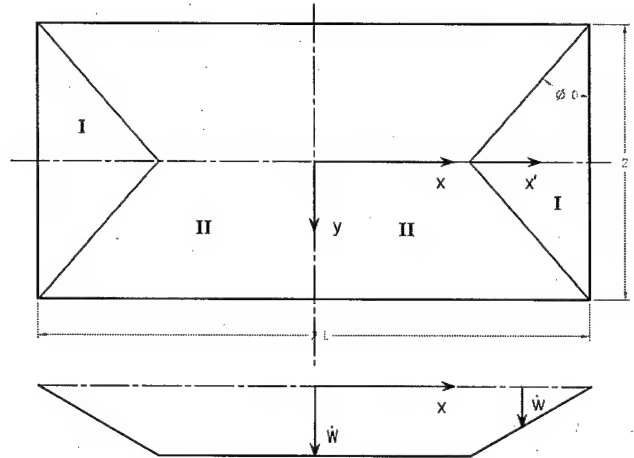

Figure 19: Kinematically Admissible Transverse Velocity Profile

An energy method is applied by deriving the internal energy dissipation in the plate, and the external work due to the uniform applied pressure. Equating these energies and solving obtain the upper bound for collapse pressure. This energy method is also used to solve for the collapse pressure in a partially restrained boundary condition case. To approximate the partially restrained boundary condition, a moment between zero and the plastic collapse moment, M_o, is applied to the outer bound of the plate. This applied moment gives additional energy dissipation around the plate boundaries, which is added to the internal energy dissipation. This total energy is then equated to the external work energy (which remains the same from the simply supported case) and the plastic collapse pressure is obtained.

Jones also looks at the dynamic plastic behavior of plates by including an inertia term in the governing equations of equilibrium. As a representative case, the static pressure derived above is applied as a uniform rectangular pulse of duration τ. To simplify calculation, the plate is assumed to be square. The square geometry allows use of symmetry when assuming a kinematically admissible velocity profile. For cases where the applied peak pressure is greater than twice the static collapse pressure for the plate, the velocity profile must be divided into three distinct phases. The displacement solutions for each of these phases are added together to arrive at an overall displacement for the dynamic load case. The result of these derivations is presented in the first section of Appendix F.

For the purposes of this study, this method of establishing net displacement based on a representative dynamic load is helpful to visualize the amount of permanent displacement a structure which does not rupture will undergo under these blast conditions. For example, using a plate thickness of 0.4375 inch, a one foot by one foot plate will deflect 0.435 inch, or approximately one plate thickness. When the size of the simply supported plate is increased to more typical ship dimensions of 9 ft square, the resulting displacement is 7.62 feet. For a ship deck, this would represent a deflection spanning to within 2 feet of the overhead of the compartment. Some form of collapse or fracture failure of the structure would most certainly accompany deflections of this size.

55

Further Considerations

The theoretical methods presented above for solving the stiffened panel problem do not consider all factors influencing the final failure pressure of the panel. Each of the methods used operates on a series of assumptions affecting the outcome achieved. These methods were chosen based on increasing complexity of the model used without resorting to numerical methods. It is recognized that many other factors must be considered to obtain truly accurate results. Often the affects of these conditions are only understood qualitatively and cannot be accurately modeled through empirical or simple first-principals based calculations.

For example, the method of attachment of the stiffeners is likely to play a major role in this problem. Welding causes interesting modifications to the properties of the steel. In addition, most high-strength steels are worked to increase the yield strength of the steel, but in the process, the ductile zone of the member is reduced. This is especially true in the heat affected zone surrounding a weld. Therefore, although the stiffeners increase the overall strength of the panel until the onset of yield, the region of strain which the material can withstand after the onset of yield (usually about 8-10x the yield strain for steel) can be significantly reduced due to the heat affected region. For example, steel ruptures when the strain reaches a fracture strain, ε_f, typically about 20% for bare steel. However, this strain is significantly less for material in a heat-affected zone. Paik et al (2003) show that actual weldment material has an even lower ε_f value, typically around 8%.

DDG-51 and DD(X) Structural Analysis

The question still remains; what is the level of mitigation necessary to make a blast mitigation system feasible? In order to determine a quantitative level of success for mitigation, real-world data for the strength of ship structures must be studied in comparison to a representative blast loading. Two candidate platforms were studied to determine their intrinsic blast resistance and the amount of mitigation necessary to prevent the spread of damage from a blast: the DDG-51 class destroyer and the DD(X) next-generation destroyer.

56

The Arleigh Burke Class (DDG-51) destroyer represents the current state-of-the-art in Naval combatant design. Its structure includes a side shell and transverse bulkheads composed of high strength steel and a weather deck, longitudinal bulkheads, and stiffeners composed of ordinary or medium strength steel. The material properties for these steel components are listed in full in Appendix D. Analyzing the structure of this platform is very relevant since much of the impetus of designing blast mitigation systems results from the aftermath of the bombing of the USS Cole, an Arleigh Burke Class destroyer.

DD(X) is the next generation of Naval destroyer, currently in the detailed design phase. Although this ship does not yet exist in the operating fleet, it is a prime candidate for future installation of a blast mitigation system due to some of the ship's unique design features. In the current design of DD(X), the side shell, weather deck, transverse bulkheads and internal frames are all composed of high strength steel with mild steel stiffeners. The longitudinal bulkheads, however, are composed of HY100 with HSLA-80 stiffeners. This stronger material is used as armor plating inboard of the Peripheral VLS cells to protect the ship from incoming blasts impacting the missile cells and causing collateral damage inboard of the launchers. Due to the advanced, tumblehome hull form used for this ship, the missile launchers are installed along the side hull rather than along centerline. The additional structure in the longitudinal bulkheads is both heavy and costly. However, there is space outboard of the missile launchers (due to the reverse curvature of the hull) which could potentially house a mitigation system. If blast pressures could be reduced outboard of the missile cells, a further layer of protection would be added to the hull. This protection could allow for a reduction in the weight and cost of the longitudinal bulkheads and reactive armor plating needed in the current design.

For purposes of comparison, the structural arrangement of the side hull panels was analyzed for both the DDG and the DD(X). A variety of analyses akin to those presented above are calculated for each of these ships in Appendices E-I. Since most of the calculations presented do not specifically account for the support of the stiffeners in the panel, two geometries were considered: one using the panel as a whole and a second using a

57

narrower panel spanning from frame to frame in width, but only from stiffener to stiffener in height. Figure 20 shows the relevant dimensions for each ship.
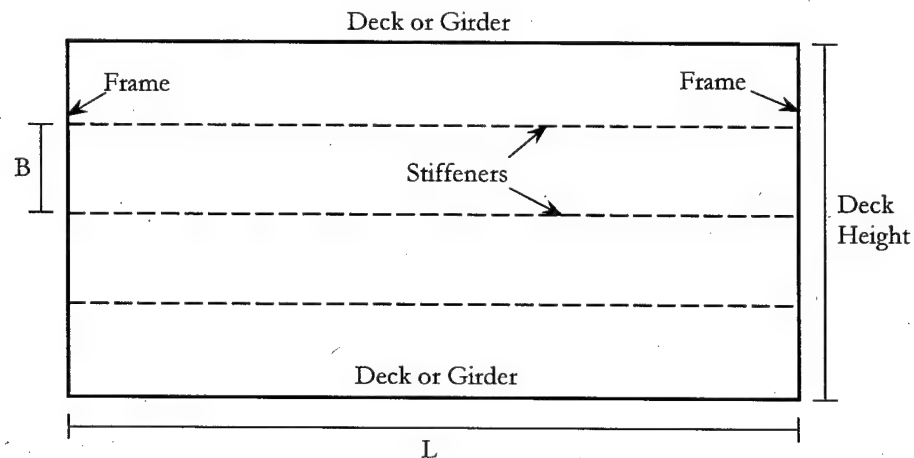

Figure 20: Stiffened Panel Structural Arrangement

	DDG-51	*DD(X)*
H (plate thickness)	0.3438 in	0.4375 in
L (frame spacing)	8.0 ft	7.54 ft
D (Deck height)	9.13 ft	9.99 ft
Stiffeners per panel	3	4
B (stiffener spacing)	27.39 in	23.99 in

Table 1: Stiffened Panel Properties

Each of the methods of deriving collapse pressure for a stiffened panel described above was applied to the panels installed on these ships. In order to fully understand the geometry of these stiffened panels, the calculations were completed considering the panel to span from frame to frame horizontally and girder to girder vertically (L x D). From the dimensions shown in Table 1, it is observed that the geometry represents a nearly square panel for both ships. These calculations were then repeated considering the panel to span

58

from frame to frame and from stiffener to stiffener (L x B). This panel has a much higher aspect ratio. The calculations involved in these analyses are presented in the corresponding appendices to this report. A summary of the findings of all calculations are presented in Table 2 and in Appendix I.

When calculating the panel strength from girder to girder and frame to frame, the minimum pressure calculated is the result of the simply supported beam bending method. The maximum pressure from the first principles calculations is that resulting from the inclusion of a kinematically admissible velocity profile with a fully clamped boundary condition. The results from the empirical calculation methods used in the U.S. Navy design data sheets are two orders of magnitude greater than any of the first principle method results. Discovering the source of this discrepancy will be central to any future work on this problem.

For the higher aspect ratio geometry between stiffeners, the beam bending method was calculated assuming the span to be twice the B dimension since the model for these calculations places one stiffener at mid-span and another at each end of the panel. Using the deep beam approximations where the span is significantly shorter than the depth, as is the case using the stiffener spacing, the bending moment calculations result in higher estimates of the resistance, especially when dynamic considerations are included. For this geometry, the values calculated for using the Design Data Sheets are still approximately an order of magnitude greater than those calculated using first principles.

		Units	DDG - 51 Class	DD(X)
	T (PlateThickness)	in	0.3438	0.4375
	L (Frame Spacing)	ft	8	7.54
	H (Deck Height)	ft	9.13	9.99
	Stiffeners per panel		3	4
	Stiffener Spacing	ft	3.043	2.498
Plate Between Decks and Girders/Frames	Static Failure Pressure (Moment calculation)	Pa	1.23E+04	1.67E+04
	Dynamic Failure Pressure (Moment + strain rate effects)	Pa	3.65E+04	4.93E+04
	Simply Supported Lower Bound (Johansen Yield Condition)	Pa	2.83E+04	4.53E+04
	Simply Supported Upper Bound (Energy Method with Velocity Profile)	Pa	2.83E+04	4.55E+04
	Fully Clamped Lower Bound (Statically Admissible Stress Field)	Pa	3.78E+04	6.12E+04
	Fully Clamped Upper Bound (Energy Dissipation Method)	Pa	5.66E+04	9.10E+04
	Partially Clamped (50%) (Energy Method)	Pa	4.25E+04	6.83E+04
	DDS 100-7 (blast loading)	Pa	1.57E+06	2.32E+06
	DDS 100-9 (air blast / nuclear)			
	For Max Deflection w/o rupture	Pa	2.55E+07	2.94E+07
	For Ship Specifications	Pa	5.75E+06	6.66E+06
Plate Between Stiffeners and Girders/Frames	Static Failure Pressure (Moment calculation)	Pa	4.93E+04	1.04E+05
	Dynamic Failure Pressure (Moment + strain rate effects)	Pa	1.46E+05	3.08E+05
	Simply Supported Lower Bound (Johansen Yield Condition)	Pa	1.80E+05	3.71E+05
	Simply Supported Upper Bound (Energy Method with Velocity Profile)	Pa	1.83E+05	3.76E+05
	Fully Clamped Lower Bound (Statically Admissible Stress Field)	Pa	2.84E+05	5.94E+05
	Fully Clamped Upper Bound (Energy Dissipation Method)	Pa	3.65E+05	7.53E+05
	Partially Clamped (50%) (Energy Method)	Pa	2.74E+05	5.65E+05
	DDS 100-7 (blast loading)	Pa	2.48E+06	4.53E+06
	DDS 100-9 (air blast / nuclear)			
	For Max Deflection w/o rupture	Pa	2.55E+07	2.94E+07
	For Ship Specifications	Pa	5.75E+06	6.66E+06

Table 2: Comparison of Stiffened Panel Calculations

For the purposes of this investigation, the peak overpressure applied to the panel in question is 130.3 psi or 8.985×10^5 Pa. The static equivalent pressure applied to the panel is 312.4 psi or 2.154×10^6 Pa. This peak overpressure is below the failure pressure calculated using the U.S. Navy Design Data Sheets. The static equivalent pressure is less than the failure pressures calculated using the DDS's for all cases other than the DDG-51 panel spanning from frame to frame and girder to girder.

The results of the stiffened panel problem provide a starting point to investigate the level of mitigation that can be achieved using water mist. The ideal situation would be to reduce the representative 500 lb TNT blast load on a ship bulkhead to a level below any of the pressures calculated above. This most conservative expectation is unlikely to be met by any mitigation system. However, achieving a level of mitigation which reduces the pressure loading to below the levels calculated using the dynamic considerations is a realistic goal for a feasible system.

SCALING AND DESIGN

Matching of Ship Failure Loads to Mitigation Level Achieved

Based on the calculated load resistances of stiffened panels for two representative ships, a desired mitigation level can be identified. Evaluation of the feasibility of a water mist blast mitigation system for shipboard use begins with a comparison of the mitigation levels achieved through applying water mist to the mitigation necessary to prevent failure of ship structures. The same energy comparison method presented in Appendix A was also used to establish necessary mitigation levels for each of the shipboard panel geometries discussed. As a minimum, the failure pressure calculated using the fully clamped boundary condition and the energy method (Appendix F) were used to establish the amount of energy that must be absorbed from the impinging shock front. Results of these calculations are presented in Table 3 below.

	Units	DDG-51 Full panel	DDG-51 Between Stiffeners	DD(X) Full Panel	DD(X) Between Stiffeners
Δ **Pressure**	Pa	2.087×10^6	1.479×10^6	2.037×10^6	4.317×10^5
$P_{reduced}/P_{original}$	% Reduction of Peak Overpressure	96.9%	68.7%	94.6%	20%
Δ **Energy**	J/m^2	1.435×10^5	1.017×10^5	1.401×10^5	2.966×10^4

Table 3: Required Mitigation for Prevention of Ship Panel Failure

From this table, it is observed that the mitigation necessary based on the full panel geometry is not possible with the levels of mitigation observed in laboratory experiments and numerical simulations. Even under the most liberal failure loading case calculated, the full panel geometry would require peak overpressures to be reduced to between 3 and 5% of their unmitigated values. This is about an order of magnitude greater mitigation than is achieved using water mist. It should be noted that these full panel calculations did not include the strengthening effects of the stiffeners in the panel and therefore are conservative.

It is possible and quite feasible to mitigate the blast to the level which prevents failure as calculated for the panel spanning from frame to frame and stiffener to stiffener. This stiffener to stiffener calculation is likely to be a closer approximation to the actual strength of the stiffened panel structure installed on U.S. Navy ships. Based on this consideration, the water mist blast mitigation system could be a useful defense to protect ships from blast loading on the side hull. However, the correct mist parameters must be designed to achieve the mitigation needed. In addition, the space used for the water mist system must provide adequate depth to allow the mist to exhibit its mitigation properties. A space providing only 1 or 2 meters of water mist prior to the shock front encountering the next bulkhead will actually enhance the peak overpressures of the shock front, creating a negative effect. This necessary depth, along with the proper mist properties, are essential to a feasible design.

Mist Parameters

It has been demonstrated that significant mitigation of the peak overpressures experienced in blast loading can be accomplished using water mist. Based on experimental results, it appears that peak overpressure can be reduced by 30% of its original value with a well-designed mitigation system using optimal droplet size and mass loading ratios. Numerical results for an optimized seeded gas indicate that pressure reductions as great as 35% are possible. For a constant mass loading of 0.63 and optimized droplet size of 26-28 μm, the maximum overpressure is reduced as shown in Figure 21. This figure shows an idealized pressure reduction, not accounting for the inherent decay of the shock pulse through air. The no particles case in this figure represents a pure vacuum, but does show the dramatic effect the water mist could theoretically have on peak overpressures due to shock.
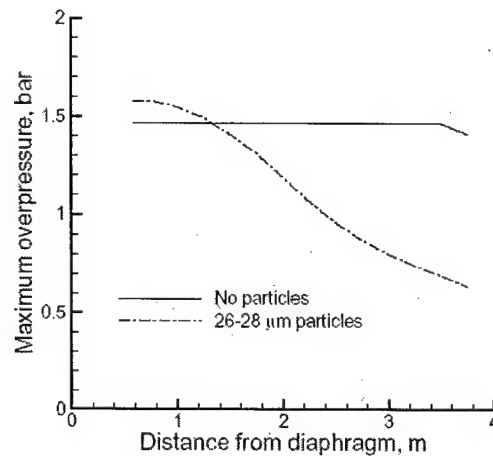
Figure 21: Maximum Overpressure as a Function of Distance through Seeded
Gas for M_o = 1.49, η = 0.63 (Schwer et al (2002))

One of the major design parameters in designing a mitigation system for shipboard applications is optimizing the mean droplet size of the water mist. For feasibility, the necessary nozzles to facilitate creation of the optimized droplet size should be readily available. Based on study of commercial water mist systems, the minimum practical mist size is about 15μm. The current U.S. Navy water mist system uses 100 μm droplets. From the experimental and numerical results presented in this report, the optimal droplet size falls between 20 and 40 μm. Therefore, the proposed mitigation system will use a mean droplet size of 25-30 μm.

The mass loadings used in both the shock tube tests and the numerical simulations play a major role in the resulting mitigation. Some question exists as to whether a mitigation system should be designed for a specific mass loading or for a specific numerical particle density. For perfectly uniform droplets in a homogeneous mixture of mist, the difference between holding mass loading constant and holding number density of droplets constant would be identical. However, for a dynamic mist undergoing settling, introduction of new mist through the nozzles, the number of particles in a volume may not be constant for a constant mass loading and vice versa.

Schwer et al (2002) investigated the effect of which of these parameters is held constant in numerical simulations. The results of these simulations are presented in Figure 22 for a variety of droplet sizes. The plot on the left in this figure shows results for a constant mass loading, as many of the previous figures in this report have shown. The figure on the right shows the results from holding a constant number density of particles. The resulting mass loadings for each particle size are shown in the plot. These results play into the scaling of concentration used in this study based on the droplet size. The theory behind Schwer's calculations was to neutralize the increased effect of vaporization for smaller droplets by reducing the total number of drops in the mixture. This method proved invalid since these vaporization effects are a function of surface area of the droplets to a greater extent than they are a function of total number of droplets.
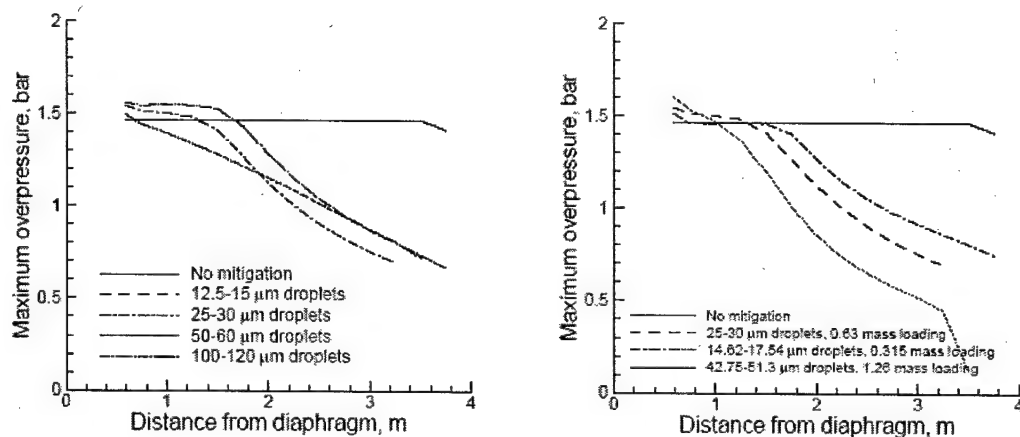

Figure 22: Maximum Overpressure for Different Droplet Sizes with Mass Loading Held Constant ($\eta = 0.63$) (left) and Number Density Held Constant (Schwer et al (2002))

Based on the results of the shock tube tests and numerical simulations presented, mitigation is most effective for mass loadings between 0.5 and 1.0. A large amount of data exists proving the mitigation properties for a representative Mach number for blast loads and a mass loading of 0.63. Therefore, this mass loading will be used for the proposed design, although it is recognized that this mass loading is predominantly a function of nozzle geometry and pressure on the system. For shipboard installations, optimization of

65

the mass loading can only be achieved to an order of magnitude estimate. The actual mass loading will be highly dependent on the current fire suppression system usage and pressure.

Current U.S. Navy Water Mist Fire Suppression System

The U.S. Navy has developed a machinery space water mist system that utilizes a modified high-pressure spray nozzle. According to the CPSMA (1997), The system is designed to produce high volumes of 100 mm droplet (mean diameter) sprays with very high spray momentum to achieve rapid suppression of large hydrocarbon pool or spray (Class B) fires. These nozzles emit 2 gpm at 1000 psi on a grid system. This system produces water flow application rates ($0.06 - 0.07$ gpm/ft^2) three to four times higher than commercially available systems. Although the mitigation effects are not observed to the same extent for droplet sizes in the 100 μm range used in the current U.S. Navy water mist system, modification to smaller nozzle apertures such as those used on many commercially available water mist systems could make such a system feasible for installation on ships.

Input parameters into the design of a water mist blast mitigation system include the shape and size of the space to which the mist is applied and the pressure, flow application rate, and droplet size of the water mist itself. The 1000 psi system currently being tested for U.S. Navy platforms in a machinery room setting provides a good starting point for a feasible back fit design for future platforms. The mass loading (mass of particles/mass of air) for this system is on the order of 2.0, whereas the mass loading for the proposed mitigation system is 0.63. Therefore, the Navy system must be modified to reduce mass loading, a result that will be achieved simultaneously with reducing the mean droplet size applied to the space.

Proposed DD(X) Design

Based on the feasibility of the water mist fire suppression system already being used on Naval platforms to include a blast mitigation system, a design is proposed for the next generation destroyer, DD(X). DD(X) is a prime candidate for a blast mitigation system due to the geometry of the tumblehome hull form and the peripheral vertical launch system (PVLS). The sides of the hull slope inward from a maximum beam below the waterline.

66

Vertical launch missile cells are positioned directly inboard of the side hull in this design, creating a dead space outboard of the missiles due to the slope of the hull. Figure 23 shows the design of the PVLS modules, including the dead space outside of the launcher This dead space is approximately 2.5 meters deep in the athwartships direction at its deepest point, close to the waterline.
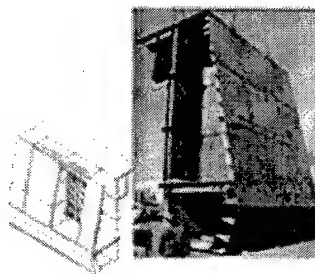

Figure 23: PVLS Module and Outboard Hull Design

The ship is designed with a bit more side-hull protection as a consequence of the location of the missile launchers. In order to protect the ship from damage due to unintentional detonation of the missiles housed in these launchers, current design uses reactive armor and heavy plating inboard of the launcher. This reactive armor is shown in Figure 24 along the back side of the module. This design is necessary to protect the ship, but costly in terms of space and weight. The proposed mitigation system provides an alternative means to partially reduce blast loading on the side hull of DD(X) could produce significant savings for the ship design.
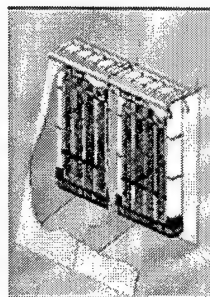

Figure 24: PVLS Schematic Diagram

67

Figure 24 also shows the geometry of the space outboard of the missile launcher. This triangular space is the proposed location of the blast mitigation system. Potential concerns include the dimensions of this space being adequate to allow for mitigation of the impinging blast. The dimensions of the space at its deepest point fall close to the threshold where the water mist begins exhibiting mitigation effects. Therefore, a close look at the exact dimension necessary on a large scale application to achieve mitigation effects is essential to the continuation of this design. Unfortunately, enhancing this issue, the top portion of this space does not provide the same depth. In terms of a system to protect against small boat threats, this is not a major issue. The top of this space is well above the waterline of the ship and outside the reach of an impinging blast wave, but depth of the proposed installation is still a major concern for future work.

This blast mitigation system is applicable for back fit or installation on any Naval platform using the water mist fire suppression system. DD(X) is proposed here due to the inherent dead space just inside the hull, but since the water mist blast mitigation system only requires the installation of additional nozzles in the spaces directly inboard of the hull, it could be installed on any platform.

The premise of operation for such a blast mitigation system would be to light off the mist nozzles in the spaces inboard of the hull when an incoming threat was eminent. This could mean an incoming missile threat in an at-sea scenario or an approaching small boat in a littoral or in port scenario. Constant operation of the nozzles would not be necessary; further investigation would be required to define a cycling process to maintain the necessary mass loading of mist in the air.

CONCLUSIONS AND RECOMMENDATIONS

The recent trend of using fine water mist systems to replace the legacy HALON-1301 fire suppression systems warrants further study into other applications of the water mist systems. Shock tube testing and numerical simulations indicate that fine mists (20-30 μm droplet size) may reduce peak overpressures of a shock wave traveling through a space by up to 70%. Such pressure reductions could be used to mitigate the destructive effects of a shock wave (initiated by an explosive device) traveling through a structure. Although the mitigation effects are not observed to the same extent for droplet sizes in the 100 μm range used in the current U.S. Navy water mist system, modification to smaller nozzle apertures such as those used on many commercially available water mist systems could make such a system feasible for installation on ships.

Currently these blast mitigation effects have only been demonstrated in small-scale shock tube tests and computer simulations. Uncertainty exists as to the scalability of such a system. The intention of this research was to fully investigate the applicability of such a blast mitigation system for shipboard use. A study of the degree of mitigation necessary to make a system practical for shipboard installation was conducted. In addition, a theoretical study of the mechanisms of blast mitigation using water mists was undertaken to explain the phenomena and possible methods of scaling and application. Current research into water mist blast mitigation was thoroughly reviewed and examined for trends to aid in guiding the direction of future work. Based on these studies, it was determined that water mist systems do provide enough peak blast pressure reduction to warrant possible installation on warships.

These trends provide the necessary information to design a scalable blast mitigation system with applicability to real-world shipboard spaces. Given the recent trend toward tumblehome hull forms in future Naval Combatant designs, there exists strong applicability of this system in the "dead" spaces created by the shaping of the tumblehome hull. The end goal was a feasible design of a blast mitigation system to be used in the outermost

spaces of Naval Combatants to protect interior vital system spaces. However, concerns over the depth of mist that a shock wave must travel through in order to achieve mitigation limit the applicability of this system based on current data.

A blast mitigation system for installation on U.S. Navy ships using water mist is a still a viable future technology. Based on the strength characteristics of a current and a future destroyer, the mitigation system would be required to reduce peak overpressures from a blast by between 30% and 80% of the initial blast loading pressure. Depending on the strength of the stiffened panels in the ship, this mitigation could reduce the loading on the ship structure to a level that makes the probability of plastic collapse or failure of the panel minimal. More research into the applicability of scaling the current laboratory and numerical results to a shipboard space are needed to continue design of the system.

Recommendations for Future Work

Further development of a water mist mitigation system would require quantitative mitigation results for the proposed design using shock tube testing on an actual water mist. All laboratory data presented here was for some form of dry particle-air mixture. The results for water droplets are all based on numerical simulations validated against the dry particle results. A method of suspending a representative water mist in the driven section of a shock tube must be developed to accomplish this testing. Outa et al (1976) discuss the difficulties involved in developing a technique for injecting particles to achieve a satisfactorily uniform dispersion in the gas during shock tube testing. These conditions are amplified by the requirement to create the water mist and ensure that the mean droplet diameter of the mist meets the design specifications for the mitigation system. Design and testing of a method to run shock tube simulations on water mists of varying concentrations and droplet diameters should be accomplished. The results of such testing would validate numerical simulations of the mitigation effects and allow more detailed design of a full-scale mitigation system.

Scaling of these shock tube tests to a more typical shipboard space must be investigated to further validate current numerical models. This could be accomplished by

running live fire tests with water mist in a space and recording pressure profiles along various locations inside the space. This data would be invaluable to determining the spatial effects of using the water mist in a space that has a breadth and height comparable to its depth.

In addition, a close study must be conducted to quantify the exact depth of space required to achieve mitigation effects from a water mist using the parameters optimized for the proposed system in this report. Actual shipboard spaces should be used to model the scaling effects of moving from a small shock tube to a large (in terms of breadth and height) space. The important parameter to achieve out of these tests is the necessary depth required to ensure that the mist provides adequate mitigation effects and does not cause enhancement of peak overpressures under any conditions. Determining this depth parameter will define whether the mitigation system is feasible for future installation.

Future work in the problem of blast loading and mitigation systems for ships should also include more analysis into the stiffened panel problem. Based on the theoretical calculations presented in this report, the loading to failure of a typical ship stiffened panel is on the order of 10^5 Pascals. However, the failure loading calculated using the empirical formulations in U.S. Navy Design Data Sheets is about two orders of magnitude greater than this. Although the theoretical calculations used in this analysis involve many simplifying assumptions including mode shape and velocity profile, a wide variety of methods were studied. Of the parameters varied among these methods, boundary conditions had the largest effect on the resulting pressure load to failure. None of these parameters or assumptions account for a discrepancy as large as that between the theoretical results and the empirical results. The cause of this discrepancy should be identified and understood before lending further credence to the results for the actual strength of stiffened panels under dynamic blast loading.

Finally, for further development of the specific design proposed for DD(X), the stiffened panel analysis presented should be repeated using the scantlings of the armor plated bulkhead located immediately behind the PVLS. The specific geometry of the space

outboard of the PVLS launcher should be entered into numerical simulation tools to establish a mitigation pattern for this proposed installation. Based on the mitigation levels likely using a water mist system, the longitudinal bulkhead could be optimized. By optimizing this bulkhead, an analysis could be conducted on the difference in ship displacement, cost, and fabricability based on the installation of the blast mitigation system. A significant savings in terms of ship design impact would provide the true determination of the feasibility of the water mist blast mitigation system.

BIBLIOGRAPHY

[1] Gunder, J. (2000), "At Least Six Sailors Killed in Small Boat Attack on USS Cole," Navy Wire Service, 13 Oct 2000, Navy Office of Information.

[2] Navy Office of Information (2000), "Injured Cole Sailors Welcomed Home After Explosion in Aden," Navy Wire Service, 17 Oct 2000, Navy Office of Information.

[3] Gloekler, M. (2001), "Navy Announces Results of USS Cole Investigation," CNO Public Affairs, 19 Jan 2001, Navy Office of Information.

[4] Kandaras, C.A. (1996), Statement Before the Subcommittee on Defense of the Senate Appropriations Committee on the FY1997 Department of the Navy Environmental Budget, 8 May 1996, Navy Public Affairs Library.

[5] Outa, E., Tajima, K., Morii, H. (1976), "Experiments and analyses on shock waves propagating through a gas-particle mixture," Bulletin of the JSME, Vol. 19, pp 384-394.

[6] Sommerfield, M. (1985), "The unsteadiness of shock waves propagating through gas-particle mixtures," Experiments in Fluids, Vol. 3, pp197-206.

[7] Commission on Physical Sciences, Mathematics, and Applications (1997), Fire Suppression Substitutes and Alternatives to Halon for U.S. Navy Applications, National Academies Press, pp. 85-95.

[8] Clift, R., Grace, J.R., Weber, M.E. (1978), Bubbles, Drops, and Particles, Academic Press, New York.

[9] Crowe, C., Sommerfield, M., Tsuji, Y. (1998), Multiphase Flows with Droplets and Particles, CRC Press, Boston.

[10] Taylor, G.I. (1948), "The Pressure and Impulse of Submarine Explosion Waves on Plates," The Scientific Papers of Sir Geoffrey Ingram Taylor, Vol. 3, No. 31, pp287-303.

[11] Cole, R.H. (1948), Underwater Explosions, Princeton University Press.

[12] Nonaka, T (2000), "Shear failure of a steel member due to blast," International Journal of Impact Engineering, Vol. 24, pp231-238.

[13] Rudrapatna, N.S., Vaziri, R., Olson, M.D. (1999), "Deformation and failure of blast-loaded square plates," International Journal of Impact Engineering, Vol. 22, pp449-467.

[14] Rudrapatna, N.S., Vaziri, R., Olson, M.D. (2000), "Deformation and failure of blast-loaded stiffened plates," International Journal of Impact Engineering, Vol. 24, pp457-474.

[15] Shin, H., Lee, W. (2003), "Material design guidelines for explosive confinements to control impact shock-induced detonations based on shock transmission/reflection analysis," International Journal of Impact Engineering, Vol. 28, pp465-478.

[16] Schleyer, G.K., Hsu, S.S. (2000), "A modeling scheme for predicting the response of elastic-plastic structures to pulse pressure loading," International Journal of Impact Engineering, Vol. 24, pp759-777.

[17] Ramajeyathilagam, K., Vendhan, C.P., Rao, V.B.(2000), "Non-linear transient dynamic response of rectangular plates under shock loading," International Journal of Impact Engineering, Vol. 24, pp999-1015.

[18] Nurick, G.N., Olson, M.D., Fagnan, J.R., Levin, A. (1995), "Deformation and tearing of blast-loaded stiffened square plates," International Journal of Impact Engineering, Vol. 16, pp273-291.

[19] Klaus, M.H. (1985), "Response of a panel wall subjected to blast loading," Computers and Structures, Vol. 21, pp129-135.

[20] Houlston, R., Slater, J.E., Pegg, N., DesRochers, C.G. (1985), "On analysis of structural response of ship panels subjected to air blast loading," Computers and Structures, Vol, 21, pp273-289.

[21] Board on Infrastructure and the Constructed Environment Commission on Engineering and Technical Systems National Research Council (1995), Protecting Buildings from Bomb Damage: Transfer of Blast-Effects Mitigation Technologies from Military to Civilian Applications, National Academy Press.

[22] Remennikov, A. (2004), "Evaluation of blast loads on commercial buildings: From hand calculations to GIS-based numerical simulations," Second National Engineering & Security Research Forum, Melbourne, Australia.

[23] Design Data Sheet 072-4 (1986), "Hull, mechanical, and electrical systems survivability," Department of the Navy, Naval Ship Engineering Center.

[24] Design Data Sheet 079-1 (1975), "Stability and buoyancy of U.S. Naval surface ships," Department of the Navy, Naval Ship Engineering Center.

[25] Design Data Sheet 100-4 (1982), "Strength of structural members," Department of the Navy, Naval Ship Engineering Center.

[26] Design Data Sheet 100-6 (1987), "Longitudinal strength calculation," Department of the Navy, Naval Ship Engineering Center.

[27] Design Data Sheet 100-7 (1984), "Structure to resist weapons firing effects," Department of the Navy, Naval Ship Engineering Center.

[28] Design Data Sheet 100-9 (1991), "Nuclear airblast design for surface ship structures." Department of the Navy, Naval Ship Engineering Center.

[29] Department of the Navy, Naval Sea Systems Command (1991), General Specifications for Ships of the United States Navy.

[30] Saibel, E. (1946), "A thermodynamic criterion for the fracture of metals," Physical Review, Vol. 69, p667.

[31] Jones, N. (1997), Structural Impact, Cambridge University Press.

[32] Brockenbrough, R.L., Johnston, B.G.(1974), USS Steel Design Manual, United States Steel Corporation, Pittsburg.

[33] Paik, J.K., Thayamballi, A.K. (2003), Ultimate Limit State Design of Steel-Plated Structures, John Wiley & Sons, LTD, West Sussex, England.

[34] Marble, F.E. (1970), "Dynamics of dusty gases," Annual Review of Fluid Mechanics, Vol. 2, pp397-446.

[35] Schwer, D.A., Kailasanath, K. (2003), "Mitigation of Blast Waves from Explosives using Water Mist," Proceedings of the Third Joint Meeting of the U.S. Sections of the Combustion Institute.

[36] Schwer, D., Kailasanath, K. (2002), "Shock Wave Mitigation Using Glass Particles and Water Droplets in Shock Tubes," NRL/MR/6410-03-8658, Naval Research Lab, Washington D.C.

[37] Kailasanath, K., Tatem, P.A., Williams, F.W., Mawhinney, J. (2002), "Blast Mitigation Using Water – A Status Report," NRL/MR/6410-02-8606, Naval Research Lab, Washington D.C.

[38] Shames, I.H. (1989), Introduction to Solid Mechanics, Prentice-Hall.

[39] Huges, O. (1988), Ship Structural Design, The Society of Naval Architects and Marine Engineers.

[40] Riley, W.F. and L. Zachary (1989), Introduction to Mechanics of Materials, John Wiley and Sons.

[41] Tedesco, J., W. McDougal and C.A. Ross (1999), <u>Structural Dynamics Theory and Application</u>, Addison Wesley Longman.

APPENDIX A: PROPERTIES OF WATER MIST

Properties of Water Mist:

$\rho s/\rho$ is normally ~ 10^3. For fresh water mist in room temperature air:

$$\rho_{water} := 1000\frac{kg}{m^3} \qquad \rho_{air} := 1.293\frac{kg}{m^3} \qquad \frac{\rho_{water}}{\rho_{air}} = 773.395$$

$$C_{water} := 1.00\frac{cal}{gm\cdot K} \qquad C_{air} := 0.25\frac{cal}{gm\cdot K} \qquad C_{ratio} := \frac{C_{water}}{C_{air}} \qquad C_{ratio} = 4$$

$$HeatofVap := 539\frac{cal}{gm} \qquad HeatofVap = 2.257\times 10^6\frac{J}{kg}$$

Mass loading for current U.S. Navy water mist fire suppression is as follows:

$$FlowAppRate := 0.065\frac{gal}{min\cdot ft^2} \qquad FlowAppRate = 2.648\frac{L}{min\cdot m^2}$$

$$MassAppRate := FlowAppRate\cdot\rho_{water} \qquad MassAppRate = 0.044\frac{kg}{m^2 s}$$

Remove the time dependency by assuming a settling rate of 1 meter per minute.

$$Concentration := MassAppRate\cdot 1.0\frac{min}{m} \qquad Concentration = 2.648\frac{kg}{m^3}$$

To vaporize this amount of mist:

$$Energy_{vap} := HeatofVap\cdot Concentration \qquad Energy_{vap} = 5.977\times 10^6\frac{J}{m^3}$$

This assumes the water mist is already at 100C. To get from room temperature, must calculate heat transfer to droplets:

$$k_{air} = 0.024\frac{W}{m\cdot K} \qquad k_{water} = 0.586\frac{W}{m\cdot K} \qquad h_{air} := 18\cdot\frac{BTU}{hr\cdot ft^2\cdot R} \qquad h_{air} = 102.209\frac{W}{m^2\cdot K}$$

$$Nu(D) := h_{air}\cdot\frac{D}{k_{air}} \qquad Nu\left(25\cdot 10^{-6}\cdot m\right) = 0.107 \qquad Nu_{25} := 0.107 \qquad Nu_{100} := 0.428$$

For a representative temperature shift, use ΔT = 80C $\qquad\qquad$ $\Delta T := 80 \cdot K$

$$Q_{cdot}(D) := Nu(D) \cdot \pi \cdot D \cdot k_{water} \cdot \Delta T \qquad\qquad Q_{cdot}\left(25 \cdot 10^{-6} \cdot m\right) = 3.943 \times 10^{-4} W \qquad\qquad \text{per drop}$$

Now need to know how many drops are in 1 m^3:

$$Mass_{drop}(D) := \rho_{water} \cdot \frac{\pi \cdot D^3}{6} \qquad\qquad Mass_{drop}\left(25 \cdot 10^{-6} \cdot m\right) = 8.181 \times 10^{-12} kg$$

$$n_{drops}(D) := \frac{Concentration}{Mass_{drop}(D)} \qquad\qquad n_{drops}\left(25 \cdot 10^{-6} \cdot m\right) = 3.237 \times 10^{11} \frac{1}{m^3}$$

$$Power_{temp}(D) := n_{drops}(D) \cdot Q_{cdot}(D) \qquad\qquad Power_{temp}\left(25 \cdot 10^{-6} \cdot m\right) = 1.277 \times 10^8 \frac{W}{m^3}$$

The time period for transfer of this heat to the droplets remains to be known. This time dependence is the primary reason that it is likely that vaporization is not a major contributing factor to the overall energy absorption. However, for example, assume the heat transfer does occur over the time of the shock pulse:

$$\tau := 0.2 \cdot 10^{-3} \cdot s$$

$$Energy_{temp}(D) := \tau \cdot Power_{temp}(D) \qquad\qquad Energy_{temp}\left(25 \cdot 10^{-6} \cdot m\right) = 2.553 \times 10^4 \frac{J}{m^3}$$

$$Energy_{total}(D) := Energy_{vap} + Energy_{temp}(D) \qquad\qquad Energy_{total}\left(25 \cdot 10^{-6} \cdot m\right) = 6.002 \times 10^6 \frac{J}{m^3}$$

For comparison, calculate the specific energy in the representative pressure pulse impinging on this volume:

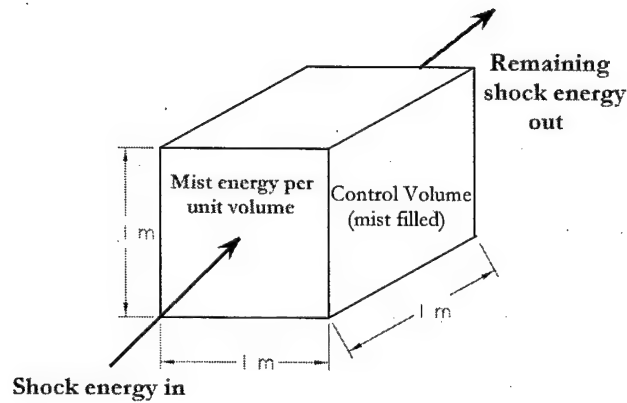$$Po := 130.3 \cdot psi \qquad \theta o := 772.5 \cdot 10^{-6} \cdot sec \qquad t_{do} := 0.029 \, sec \qquad P_i(t) := Po \cdot e^{\frac{-\left(t - t_{do}\right)}{\theta o}}$$

$$Area := 1 \cdot m^2 \qquad\qquad Volume := 1 \cdot m^3 \qquad\qquad Speed\_of\_sound := 344 \cdot \frac{m}{s}$$

$$Energy_{wave} := \int_{0.029 \cdot sec}^{10 \cdot sec} P_i(t) \cdot Speed\_of\_sound \; dt$$

$$Energy_{wave} = 2.387 \times 10^5 \frac{J}{m^2} \qquad\qquad Energy_{mist} := 6.002 \, 10^6 \cdot \frac{J}{m^3}$$

$$NetEnergy := Energy_{wave} \cdot Area - Energy_{mist} \cdot Volume \qquad\qquad NetEnergy = -5.763 \times 10^6 J$$

78

This method shows that the energy of vaporization of the water mist is over an order of magnitude greater than the energy of the pressure wave. For verification, use the static equivalent pressure from DDS 100-9 in a rectangular pulse form to recalculate wave energy:

$$P_a := 14.7 \cdot psi \qquad P_1 := Po$$

$$P_r := 2 \cdot P_1 \cdot \left(\frac{7 \cdot P_a + 4 \cdot P_1}{7 \cdot P_a + P_1} \right) \qquad q_o := \frac{5}{2} \cdot \left(\frac{P_1^2}{7 \cdot P_a + P_1} \right) \qquad P_s := \left(P_1 + q_o \right)$$

$$P_r = 697.429 psi \qquad q_o = 182.012 psi \qquad P_s = 312.312 psi$$

$$P_r = 4.809 \times 10^6 \, Pa \qquad q_o = 1.255 \times 10^6 \, Pa \qquad P_s = 2.153 \times 10^6 \, Pa$$

$$Energy2_{wave} := P_s \cdot \tau \cdot Speed\_of\_sound \qquad Energy2_{wave} = 1.481 \times 10^5 \, \frac{J}{m^2}$$

This wave energy is slightly lower than that calculated above for the exponential decay, but of the same order, validating the results above.

Recognizing that the mass loading for the current Navy system is much greater than most commercial systems using smaller droplet sizes, recalculate based on a smaller concentration of water mist which is more representative of the mist applied through the smaller aperture nozzles needed for this droplet size (reduce concentration to 1/4 since reducing mist diameter by a factor of 4):

$$\text{Concen} := \frac{\text{Concentration}}{4}$$

To vaporize this amount of mist:

$$\text{Energy}_{vap2} := \text{HeatofVap} \cdot \text{Concen} \qquad\qquad \text{Energy}_{vap2} = 1.494 \times 10^6 \frac{J}{m^3}$$

This assumes the water mist is already at 100C. Based on results of previous calculations, neglect the effect of raising the temperature of the drops from room temperature. Even at this reduced mass loading, the specific energy of vaporization of the mist is an order of magnitude greater than the energy of the impinging wave.

APPENDIX B: DYNAMICS OF GAS-PARTICLE MIXTURES

From Marble (1970):

Ideal Gas Properties: Particle Cloud:

velocity	u_i	particle radius	σ
temperature	T	velocity	u_{pi}
density	ρ	temperature	T_{pi}
		particle mass	m
		number particles/unit volume	n_m
		density	$\rho_p = n_p \cdot m$

Due to non-interaction, all particles in a local volume have the same velocity vector and temperature - individual variables could deviate randomly because of Brownian motion (particles too large) or random initial conditions (damped early in the history of the problem) or due to multiple particles sizes in mix (assume uniform here).

Continuity:
(volume of particles considered negligible)

$$\frac{\partial}{\partial t}\rho + \frac{\partial}{\partial x_i}\left(\rho \cdot u_i\right) = 0$$

$$\frac{\partial}{\partial t}\rho_p + \frac{\partial}{\partial x_i}\left(\rho_p \cdot u_{pi}\right) = 0$$

By motion equilibruim for local gas motion/acceleration, during the coupled motion of the gas and particle cloud, the particles adjust to the slip values (difference between gas velocity and particle velocity) corresponding to the local gas acceleration, while traveling a distance small compared to the characteristic dimensions of the problem. (Similar formulation for thermal equilibrium).

Force exerted by a single particle moving through the gas: $f_p = 6 \cdot \pi \cdot \sigma \cdot \mu \cdot \left(u_p - u\right)$

Force per unit volume with n non-interacting particles: $F_p = n \cdot 6 \cdot \pi \cdot \sigma \cdot \mu \cdot \left(u_p - u\right)$

where $\tau_v = \dfrac{m}{6 \cdot \pi \cdot \sigma \cdot \mu}$ $F_p = \rho_p \cdot \dfrac{\left(u_p - u\right)}{\tau_v}$

is the characteristic time, or the time required by a particle to reduce its velocity relative to the gas (slip velocity) by e^{-1} of its original value

81

Limiting form of system results as τ goes to 0. In this case, slip velocity (up-u) also goes to 0, but the volumetric particle force remains finite. This limit results in:

$$u_{pi} = u_i \qquad \text{and therefore} \qquad \frac{D\left(\frac{\rho_p}{\rho}\right)}{Dt} = \text{Constant}$$

In words, this means that particles are "fixed" to their initial mass of gas. If the initial particle distribution is uniform, $\rho_p/\rho = \kappa = $ constant. Equations of Motion become:

$$\frac{\partial}{\partial t}u_i + u_j \cdot \frac{\partial}{\partial x_j}u_i = \frac{-1}{(1+\kappa)\rho} \cdot \frac{\partial}{\partial x_i}\rho + \frac{1}{(1+\kappa)}\rho \cdot \frac{\partial}{\partial x_j}\tau_{ij}$$

Under this model, the system behaves like a perfect gas with modified properties:

Density becomes: $\qquad \rho' = (1+\kappa)\rho$

Kinematic Viscosity: $\qquad v' = \frac{\mu}{(1+\kappa)}\rho = \frac{v}{(1+\kappa)}$

Reynolds Number: $\qquad Re' = \frac{u_o \cdot L}{v'} = \frac{(1+\kappa) \cdot u_o \cdot L}{v}$

Mach Number: $\qquad M' = \frac{u_o}{a'} = \frac{u_o}{a} \cdot \sqrt{\frac{(1+\kappa)\left(1 + \frac{\kappa \cdot c}{c_v}\right)}{1 + \frac{\kappa \cdot c}{c_p}}}$

Effective flow operates under larger Reynolds and Mach numbers

Shock structure consists of complete equilibrium of gas and particles ahead of and behind the normal shock. A zone of gas-dynamic shock and a zone in which velocity and temperature equilibration occur compose the shock structure itself. To separate these zones, the velocity and temperature relaxation times must be long compared with the molecular collision time of the gas.

82

$$\frac{\rho_s}{\rho} \cdot \left(\frac{\sigma}{1}\right)^2 > 1$$

ρs = density of the substance constituting the particles
ρ = density of gas
σ = particle radius
1 = mean free path

$\rho s / \rho$ is normally $\sim 10^3$. For fresh water mist in room temperature air:

$$\rho_s := 1000 \cdot \frac{kg}{m^3} \qquad \rho := 1.293 \cdot \frac{kg}{m^3} \qquad \frac{\rho_s}{\rho} = 773.395$$

Marble postulates that the gas-dynamic shock structure is unaffected by the particle cloud even though the shock may be thin relative to the particle radius. Because the volume fraction of the particles is negligible, at any time less than 1% of the shock front is being punctured by particles.

Sommerfield extends Marble's postulations using numerical calculations and experimental results. He first postulates based on loading ratios of the gas-particle mixture for both mass and specific heat:

$$C_{water} := 1.00 \cdot \frac{cal}{gm \cdot K} \qquad C_{air} := 0.25 \cdot \frac{cal}{gm \cdot K} \qquad C_{ratio} := \frac{C_{water}}{C_{air}} \qquad C_{ratio} = 4$$

Mass loading for current U.S. Navy water mist fire suppression is as follows:

$$FlowAppRate := 0.065 \cdot \frac{gal}{min \cdot ft^2} \qquad FlowAppRate = 4.414 \times 10^{-5} \, m \, s^{-1}$$

$$MassAppRate := FlowAppRate \cdot \rho_s \qquad MassAppRate = 0.044 kg \, m^{-2} \, s^{-1}$$

Remove the time dependency by assuming a settling rate of 1 meter per minute.

$$Concentration := MassAppRate \cdot 1.0 \cdot \frac{min}{m} \qquad Concentration = 2.648 kg \, m^{-3}$$

Therefore, the mass loading (mp/mg) is:

$$MassLoading := \frac{Concentration}{\rho} \qquad MassLoading = 2.048$$

Therefore, the current Navy system has a mass loading higher than that for which the studies at hand have calculated mitigation effects.

Recognizing that the mass loading for the current Navy system is much greater than most commercial systems using smaller droplet sizes, recalculate based on a smaller concentration of water mist which is more representative of the mist applied through the smaller apeture nozzles needed for this droplet size (reduce concentration to 1/4 since reducing mist diameter by a factor of 4):

$$\text{Concen} := \frac{\text{Concentration}}{4} \qquad\qquad \text{MassLoad} := \frac{\text{Concen}}{\rho} \qquad\qquad \text{MassLoad} = 0.512$$

APPENDIX C: BLAST LOAD PREDICTION

Blast Parameter Calculations for 500 lb TNT Equivalent Explosion

From Nonaka, T. (2000):

W = Explosive charge (kg) of Sinkiri Dynamite
D = Stand-off distance (m)

TNT Equivalent to Sinkiri: $\dfrac{1239}{1950} = 0.635$ $Sinkiri_{TNT} := 0.635$

example: 500kg TNT --->317.5kg Sinkiri

$500 \, kg \cdot Sinkiri_{TNT} = 317.5 kg$

$logp(D, W) := -1.575 \log\left(\dfrac{D}{\sqrt[3]{W}} \right) + 1.224$

$logp(10, 317.5) = 0.962$ $10^{0.962} = 9.162$

$9.162 \dfrac{kgf}{cm^2} = 8.985 \times 10^5 \, Pa$ Pressure = 9.162 kgf/cm^2 = .8985 MPa

From Ramajeyathilagam, K. et al (2000):

$P(t) = P_o \cdot e^{\dfrac{-(t - t_d)}{\theta}}$ for $0 \le t \le \theta$

Po is peak pressure of shock front in Pa
θ is decay constant in μs (10^-6 sec)
W is the charge weight in kg
R is the radial stand-off distance in m

For TNT: $P_0(R, W) := 52.16 \, 10^6 \cdot \left(\dfrac{W^{\frac{1}{3}}}{R} \right)^{\frac{1}{3}}$ $\theta(R, W) := 92.5 \, W^{\frac{1}{3}} \cdot \left(\dfrac{W^{\frac{1}{3}}}{R} \right)^{-0.22}$

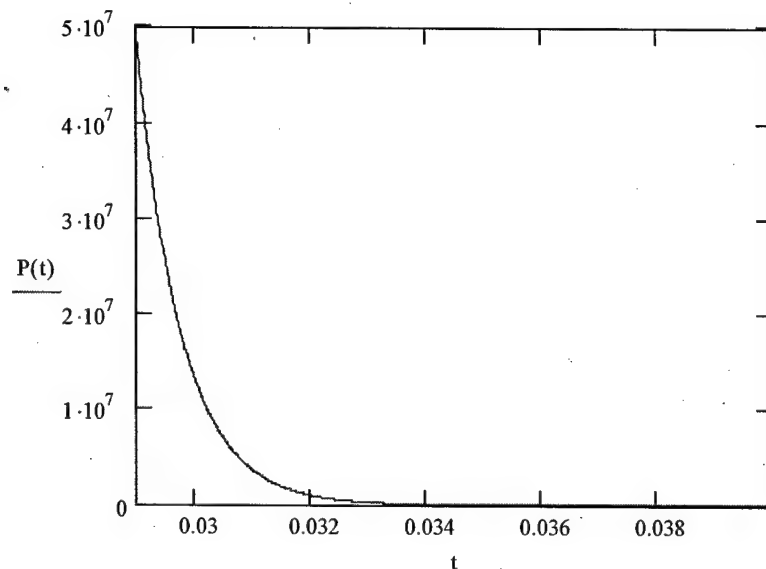$P_0(10, 500) = 4.829 \times 10^7$ Pa $\theta(10, 500) = 772.456$ μs

85

$$t_d(R, R_o, c) := \frac{R - R_o}{c}$$

td is the time delay for the pressure wave arrival at distance R
Ro is the shortest radial distance
c is the shock wave velocity

$$t_d(10, 0, 344) = 0.029$$

Can plug td into P(t) to get actual shock front pressure

$$P_{oi} := 4.829 \cdot 10^7 \qquad \theta i := 772.5 \cdot 10^{-6} \qquad t_{di} := 0.029 \qquad P(t) := P_{oi} \cdot e^{\frac{-(t - t_{di})}{\theta i}}$$

From General Specifications and DDS 100-7f, Missile Blast Pressure Equivalent:

$$P = \frac{T \cdot \left(\sin(\alpha) + \frac{0.0225}{\sin(\alpha)} \right)}{A}$$

P = static equivalent pressure (psi)
T = thrust of the missile (lbs)
α = angle of incidence (degrees)
A = impingement are of the surface (in^2)

From DDS 100-9, Nuclear airblast design for surface ships:

$$P_a := 14.7 \, psi \qquad P_1 = 130.316 psi$$

$$P_r := 2 \cdot P_1 \cdot \left(\frac{7 \cdot P_a + 4 \cdot P_1}{7 \cdot P_a + P_1} \right) \qquad q_o := \frac{5}{2} \cdot \left(\frac{P_1^2}{7 \cdot P_a + P_1} \right) \qquad P_s := \left(P_1 + q_o \right)$$

$$P_r = 697.541 psi \qquad\qquad q_o = 182.045 psi \qquad\qquad P_s = 312.362 psi$$

$$P_r = 4.809 \times 10^6 \, Pa \qquad\qquad q_o = 1.255 \times 10^6 \, Pa \qquad\qquad P_s = 2.154 \times 10^6 \, Pa$$

From Remennikov, A. (2004):

Empirical Method:

Radial Stand-off Distance (m): $\qquad R_o := 10 \qquad$ Charge Weight (kg): $\qquad W_o := 500$

Scaled Ground Distance: $\qquad Z := \dfrac{R_o}{W_o^{\frac{1}{3}}} \qquad\qquad Z = 1.26$

From Chart: $\qquad P_{so} := 1 \cdot 10^6 \cdot Pa \qquad\qquad P_{ro} := 1.4 \cdot 10^6 \cdot Pa$

      These static and reflected overpressures are close to those calculated by Nonaka above, validating that method of determining peak overpressure. The results using Ramajeyathilagam's empirical formula are over two orders of magnitude higher, although the general form of the equation is correct. An error is suspected in the empirical constant used in this formulation.

      As expected, the reflected overpressure from the graph is significantly lower than that calculated from DDS 100-9. This is due to the open, single face geometry used in the empirical method, vice the confined space. Based on these calculations, a representative blast, roughly equivalent to that experienced by the USS COLE (~500 lbs TNT) is as a comparison for the level of loading ship structures can resist without failure.

$$Po := 130.\overline{3} \qquad \theta o := 772.5 \, 10^{-6} \qquad t_{do} := 0.029 \qquad P_i(t) := Po \cdot e^{\dfrac{-\left(t - t_{do}\right)}{\theta o}}$$
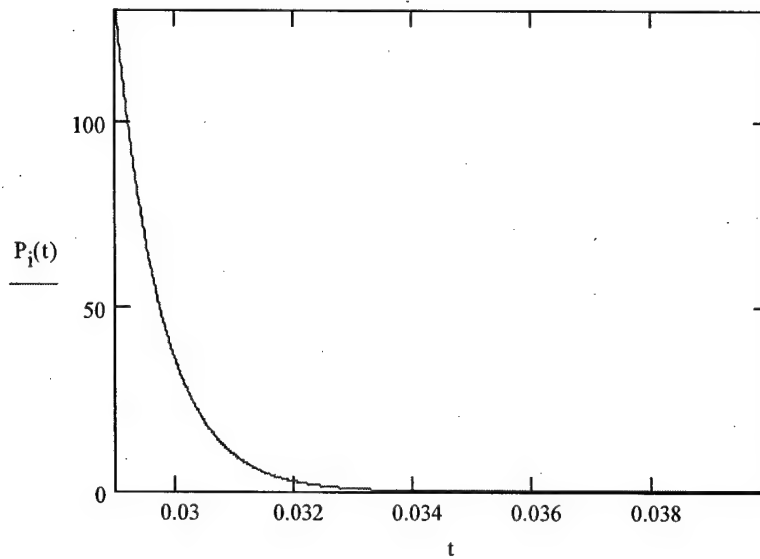
Reflected Overpressure

$P_r = 4.809 \times 10^6 \, Pa$

Dynamic Pressure

$q_o = 1.255 \times 10^6 \, Pa$

Static Equivalent Overpressure

$P_s = 2.154 \times 10^6 \, Pa$

APPENDIX D: MATERIAL CONSTANTS

Properties of Steels Used in Ship Structures

For Medium Steel (MS or OS) Components: $\nu := .30$

$\sigma_{yms} := 34 \cdot ksi$ $\sigma_{yms} = 2.344 \times 10^8 \, Pa$ $E_{ms} := 29.6 \, 10^3 \cdot ksi$ $E_{ms} = 2.041 \times 10^{11} \, Pa$

$\sigma_{ten\_ms} := 58 \cdot ksi$ $\varepsilon_{rupms} := 0.24$ $\rho_{ms} := 7833 \dfrac{kg}{m^3}$ $G_{ms} := \dfrac{E_{ms}}{2 \cdot (1 + \nu)}$

For High Strength Steel (HSS) Components:

$\sigma_{yhs} := 51 \cdot ksi$ $\sigma_{yhs} = 3.516 \times 10^8 \, Pa$ $E_{hs} := 29.6 \, 10^3 \cdot ksi$ $E_{hs} = 2.041 \times 10^{11} \, Pa$

$\sigma_{ten\_hs} := 70 \cdot ksi$ $\varepsilon_{ruphs} := 0.23$ $\rho_{hs} := 7833 \dfrac{kg}{m^3}$ $G_{hs} := \dfrac{E_{hs}}{2 \cdot (1 + \nu)}$

For HY-80 Components:

$\sigma_{y80} := 80 \cdot ksi$ $\sigma_{y80} = 5.516 \times 10^8 \, Pa$ $E_{80} := 29.6 \, 10^3 \cdot ksi$ $E_{80} = 2.041 \times 10^{11} \, Pa$

$\sigma_{ten\_80} := 95 \cdot ksi$ $\varepsilon_{rup80} := 0.20$ $\rho_{80} := 7833 \dfrac{kg}{m^3}$ $G_{80} := \dfrac{E_{80}}{2 \cdot (1 + \nu)}$

For HY-100 Components:

$\sigma_{y100} := 100 \cdot ksi$ $\sigma_{y100} = 6.895 \times 10^8 \, Pa$ $E_{100} := 29.6 \, 10^3 \cdot ksi$ $E_{100} = 2.041 \times 10^{11} \, Pa$

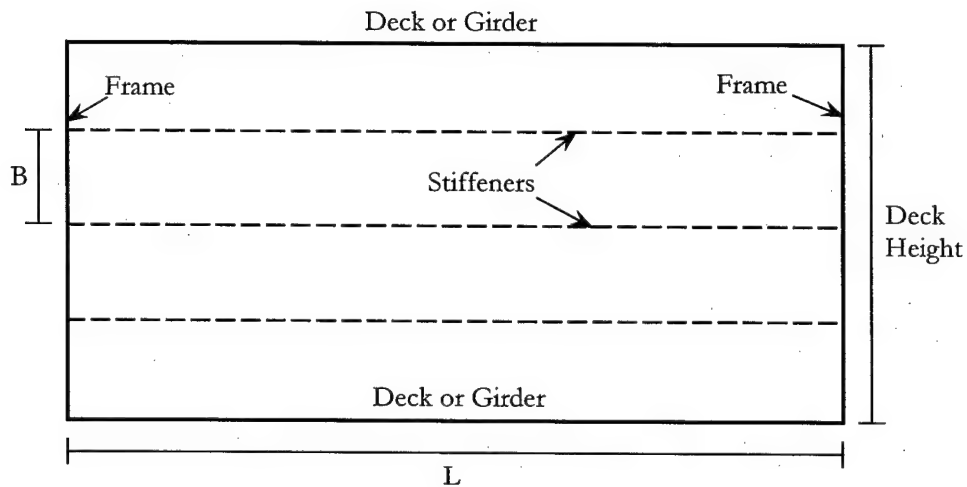$\sigma_{ten\_100} := 110 \cdot ksi$ $\varepsilon_{rup100} := 0.18$ $\rho_{100} := 7833 \dfrac{kg}{m^3}$ $G_{100} := \dfrac{E_{100}}{2 \cdot (1 + \nu)}$

Panel Characteristics for DDG-51 and DD(X)

Panel Geometry

Deck or Girder

Frame   Frame

B

Stiffeners

Deck Height

Deck or Girder

L

DDG-51	Panel Characteristics	**DD(X)**
$T_g := .3438\,in$	T = Plate thickness	$T_x := .4375\,in$
$B_g := 27.39\,in$	B = Stiffener spacing	$B_x := 23.99\,in$
$L_g := 8{\cdot}ft$	L = Frame spacing	$L_x := 7.546\,ft$
$H_g := 9.13{\cdot}ft$	H = Deck height	$H_x := 9.99\,ft$
$NoStiff_g := 3$	Number of Stiffeners	$NoStiff_x := 4$
$A_g := 1.81{\cdot}in^2$	Area of Stiffener	$A_x := 2.11{\cdot}in^2$
$BF_g := 3.94\,in$	Breadth of Flange	$BF_x := 3.94\,in$
$I_g := 6.5{\cdot}in^4$	Moment of Inertia	$I_x := 14.2{\cdot}in^4$

90

DDG-51

Panel Stiffener Characteristics

DD(X)

$D_g := 5.90 \text{ in}$ Depth of Web $D_x := 7.89 \text{ in}$

$TW_g := .170 \text{ in}$ Thickness of Web $TW_x := .170 \text{ in}$

$TF_g := .215 \text{ in}$ Thickness of Flange $TF_x := .205 \text{ in}$

$A_{webg} := TW_g \cdot (D_g - TF_g)$ Area of Web $A_{webx} := TW_x \cdot (D_x - TF_x)$

$A_{flag} := TF_g \cdot BF_g$ Area of Flange $A_{flax} := TF_x \cdot BF_x$

Plastic Flow Stress

$$\sigma_{og} := \frac{\left(\sigma_{yhs} + \sigma_{ten\_hs}\right)}{2}$$

$$\sigma_{ox} := \frac{\left(\sigma_{yhs} + \sigma_{ten\_hs}\right)}{2}$$

$\sigma_{og} = 6.05 \times 10^4 \text{ psi}$

$\sigma_{ox} = 6.05 \times 10^4 \text{ psi}$

$\sigma_{og} = 6.05 \times 10^4 \text{ psi}$

$\sigma_{ox} = 6.05 \times 10^4 \text{ psi}$

APPENDIX E: PLATE BENDING CALCULATIONS

Calculation of Bending Moment for a Stiffened Panel using Sample Geometry

Sample Plate Characteristics:

Thickness: $H := .4375 \, in$ $L := 12 \cdot in$ $B := 12 \cdot in$

$$\sigma_0 := \frac{\left(\sigma_{yhs} + \sigma_{ten\_hs}\right)}{2}$$ Plastic Flow Stress

Sample Blast Characteristics:

$p := 130.316 \, psi$ $p = 8.985 \times 10^5 \, Pa$

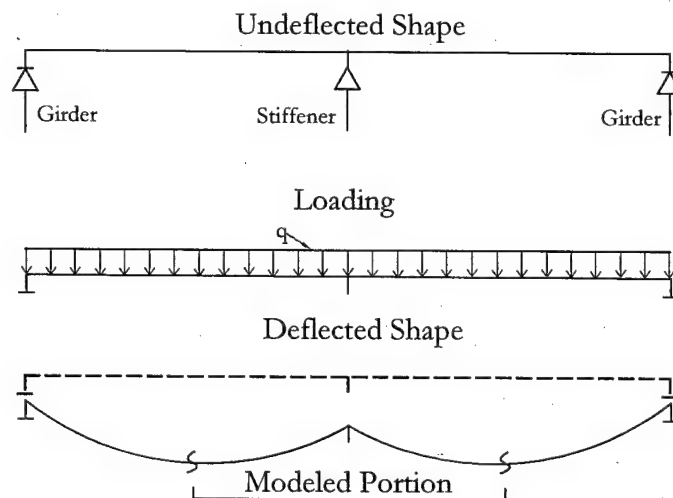$\tau := 0.2 \cdot 10^{-3} \cdot s$

Plastic Collapse Moment:

Plastic collapse moment of solid cross-section:
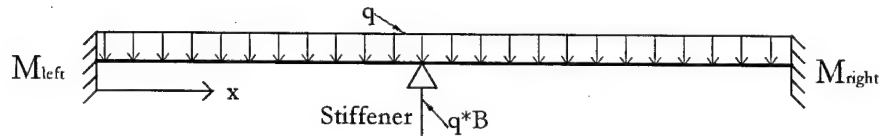
$$M_0 := \frac{\sigma_0 \cdot L \cdot H^2}{4}$$ $M_0 = 3.925 \times 10^3 \, N \cdot m$

Geometry:

Assuming a dishing mode shape between stiffeners and frames:

Undeflected Shape

Loading

Deflected Shape

92

Approximate the modeled portion of the stiffened panel as a beam (2D) with a fixed end condition to enforce the zero-slope inflection point mid-way between stiffener and frame:
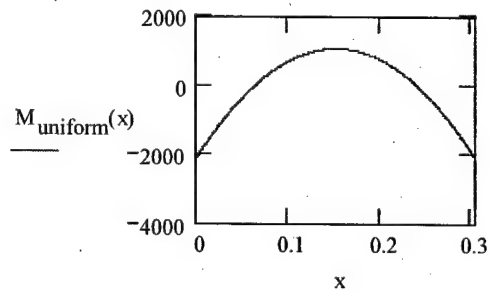

Assume that reaction force for the stiffener represents the entire distributed load, q (= pressure per unit width) * B (length between stiffener and next structural member).
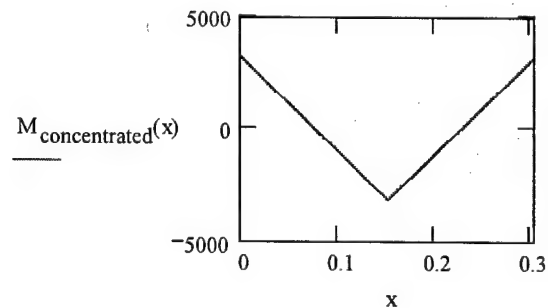
$$q := p \cdot L \qquad\qquad q = 2.739 \times 10^5 \frac{kg}{s^2} \qquad\qquad L = 0.305m$$

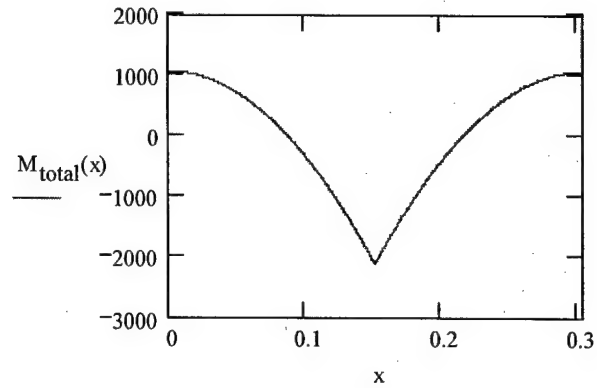From Beam tables, superposition of two loading cases to get the total moment:

$$M_{uniform}(x) := \frac{q}{12} \cdot \left(6 \cdot B \cdot x - B^2 - 6 \cdot x^2 \right)$$

$$M_{concentrated}(x) := \frac{-(q \cdot B)}{8} \cdot (4 \cdot x - B) \cdot \left(x \le \frac{B}{2} \right) + \left[-(q \cdot B) \cdot \left[\frac{x}{2} - \frac{B}{8} - \left(x - \frac{B}{2} \right) \right] \right] \cdot \left(x > \frac{B}{2} \right)$$

93

$$M_{total}(x) := M_{uniform}(x) + M_{concentrated}(x)$$

$$M_{center} := M_{total}\left(\frac{B}{2}\right)$$

$$M_{center} = -2.12 \times 10^3 \, N \cdot m$$

$$M_{ends} := M_{total}(B)$$

$$M_{ends} = 1.06 \times 10^3 \, N \cdot m$$

This representative loading case is used to show that the maximum moment will be at the at the point of inflection produced at the stiffener ($x = B/2$). Now, symbolically solving for this moment and setting equal to the plastic collapse moment, Mo:

$$M_o = 3.925 \times 10^3 \, N \cdot m$$

$$M_{unif} = \frac{q_o \cdot B^2}{24} \qquad M_{conc} = \frac{-q_o \cdot B^2}{8} \qquad M_{tot} = M_{unif} + M_{conc}$$

$$M_{tot} = M_o \qquad \text{For Plastic Flow / Failure}$$

$$M_{tot} = \frac{-1}{12} \cdot q_o \cdot B^2 \qquad \text{Neglect negative sign - Mo is for either pos or neg moment}$$

94

Calculation for Panel from Frame to Frame and Deck Girder to Deck Girder

Plastic Collapse Moment:

$$M_{og} := \frac{\sigma_{og} \cdot L_g \cdot H_g^2}{4} \qquad M_{og} = 1.939 \times 10^4 \ N \cdot m \qquad M_{ox} := \frac{\sigma_{ox} \cdot L_x \cdot H_x^2}{4} \qquad M_{ox} = 2.962 \times 10^4 \ N \cdot m$$

$$M_{unif} = \frac{q_0 \cdot B^2}{24} \qquad M_{conc} = \frac{-q_0 \cdot B^2}{8} \qquad M_{tot} = M_{unif} + M_{conc}$$

$$M_{tot} = M_0 \qquad \text{For Plastic Flow / Failure}$$

$$M_{tot} = \frac{-1}{12} \cdot q_0 \cdot B^2 \qquad \text{Neglect negative sign - Mo is for either pos or neg moment}$$

$$q_{og} := \frac{M_{og} \cdot 12}{B_g^2} \qquad q_{og} = 3.005 \times 10^4 \ \frac{kg}{s^2} \qquad q_{ox} := \frac{M_{ox} \cdot 12}{B_x^2} \qquad q_{ox} = 3.833 \times 10^4 \ \frac{kg}{s^2}$$

$$p_{og} := \frac{q_{og}}{L_g} \qquad p_{og} = 1.232 \times 10^4 \ Pa \qquad p_{ox} := \frac{q_{ox}}{L_x} \qquad p_{ox} = 1.667 \times 10^4 \ Pa$$

Now, determine the need for inclusion of dynamic terms by looking at kinetic energy

Average strain rate to rupture will be: $\qquad \tau := 0.2 \cdot 10^{-3} \cdot s$

$$\varepsilon_{dot} := \frac{\varepsilon_{ruphs}}{\tau} \qquad \varepsilon_{dot} = 1.15 \times 10^3 \ Hz$$

For strain rate effects, include Cowper-Symonds relation:

For steel: $\qquad D := 40 \cdot \frac{1}{s} \qquad n := 5 \qquad \sigma_{yhs} = 3.516 \times 10^8 \ Pa \qquad \sigma_{ten\_hs} = 4.826 \times 10^8 \ Pa$

$$\sigma_{odyn} := \sigma_{og} \cdot \left[1 + \left(\frac{\varepsilon_{dot}}{D} \right)^{\frac{1}{n}} \right] \qquad \begin{array}{l} \sigma_{og} = 4.171 \times 10^8 \ Pa \\[2mm] \sigma_{odyn} = 1.234 \times 10^9 \ Pa \qquad \sigma_{odyn} = 1.789 \times 10^5 \ psi \end{array}$$

95

$$M_{ogd} := \frac{\sigma_{odyn} \cdot L_g \cdot H_g^2}{4} \qquad M_{ogd} = 5.735 \times 10^4 \, \text{N} \cdot \text{m} \qquad M_{oxd} := \frac{\sigma_{odyn} \cdot L_x \cdot H_x^2}{4} \qquad M_{oxd} = 8.76 \times 10^4 \, \text{N} \cdot \text{m}$$

$$q_{ogd} := \frac{M_{ogd} \cdot 12}{B_g^2} \qquad q_{ogd} = 8.887 \times 10^4 \, \frac{\text{kg}}{\text{s}^2} \qquad q_{oxd} := \frac{M_{oxd} \cdot 12}{B_x^2} \qquad q_{oxd} = 1.134 \times 10^5 \, \frac{\text{kg}}{\text{s}^2}$$

$$p_{ogd} := \frac{q_{ogd}}{L_g} \qquad p_{ogd} = 3.645 \times 10^4 \, \text{Pa} \qquad p_{oxd} := \frac{q_{oxd}}{L_x} \qquad p_{oxd} = 4.929 \times 10^4 \, \text{Pa}$$

Calculation for Panel from Frame to Frame and Stiffener to Stiffener

(use 2*B as the span between stiffeners with one stiffener at midspan)

Plastic Collapse Moment:

$$M_{og} := \frac{\sigma_{og} \cdot L_g \cdot H_g^2}{4} \qquad M_{og} = 1.939 \times 10^4 \, N \cdot m \qquad\qquad M_{ox} := \frac{\sigma_{ox} \cdot L_x \cdot H_x^2}{4} \qquad M_{ox} = 2.962 \times 10^4 \, N \cdot m$$

$$M_{unif} = \frac{q_o \cdot B^2}{24} \qquad M_{conc} = \frac{-q_o \cdot B^2}{8} \qquad M_{tot} = M_{unif} + M_{conc}$$

$$M_{tot} = M_o \qquad \text{For Plastic Flow / Failure}$$

$$M_{tot} = \frac{-1}{12} \cdot q_o \cdot B^2 \qquad\qquad \text{Neglect negative sign - Mo is for either pos or neg moment}$$

$$q_{og} := \frac{M_{og} \cdot 12}{B_g^2} \qquad q_{og} = 1.202 \times 10^5 \, \frac{kg}{s^2} \qquad\qquad q_{ox} := \frac{M_{ox} \cdot 12}{B_x^2} \qquad q_{ox} = 2.393 \times 10^5 \, \frac{kg}{s^2}$$

$$p_{og} := \frac{q_{og}}{L_g} \qquad p_{og} = 4.929 \times 10^4 \, Pa \qquad\qquad p_{ox} := \frac{q_{ox}}{L_x} \qquad p_{ox} = 1.04 \times 10^5 \, Pa$$

Now, determine the need for inclusion of dynamic terms by looking at kinetic energy

Average strain rate to rupture will be: $\qquad \tau := 0.2 \cdot 10^{-3} \cdot s$

$$\varepsilon_{dot} := \frac{\varepsilon_{ruphs}}{\tau} \qquad \varepsilon_{dot} = 1.15 \times 10^3 \, Hz$$

For strain rate effects, include Cowper-Symonds relation:

For steel: $\quad D := 40 \frac{1}{s} \qquad n := 5 \qquad \sigma_{yhs} = 3.516 \times 10^8 \, Pa \qquad \sigma_{ten\_hs} = 4.826 \times 10^8 \, Pa$

$$\sigma_{odyn} := \sigma_{og} \cdot \left[1 + \left(\frac{\varepsilon_{dot}}{D} \right)^{\frac{1}{n}} \right] \qquad\qquad \sigma_{og} = 4.171 \times 10^8 \, Pa$$

$$\sigma_{odyn} = 1.234 \times 10^9 \, Pa \qquad\qquad \sigma_{odyn} = 1.789 \times 10^5 \, psi$$

97

$$M_{ogd} := \frac{\sigma_{odyn} \cdot L_g \cdot H_g^2}{4} \qquad M_{ogd} = 5.735 \times 10^4 \, N \cdot m \qquad M_{oxd} := \frac{\sigma_{odyn} \cdot L_x \cdot H_x^2}{4} \qquad M_{oxd} = 8.76 \times 10^4 \, N \cdot m$$

$$q_{ogd} := \frac{M_{ogd} \cdot 12}{B_g^2} \qquad q_{ogd} = 3.555 \times 10^5 \, \frac{kg}{s^2} \qquad\qquad q_{oxd} := \frac{M_{oxd} \cdot 12}{B_x^2} \qquad q_{oxd} = 7.078 \times 10^5 \, \frac{kg}{s^2}$$

$$p_{ogd} := \frac{q_{ogd}}{L_g} \qquad p_{ogd} = 1.458 \times 10^5 \, Pa \qquad\qquad p_{oxd} := \frac{q_{oxd}}{L_x} \qquad p_{oxd} = 3.077 \times 10^5 \, Pa$$

APPENDIX F: PLATE PLASTIC COLLAPSE CALCULATION

Dynamically Loaded Plate Analysis from Jones (1997) for Sample Geometry

Plate Characteristics:

Thickness: $H := 0.4375 \cdot in$ $L := 12 \cdot in$ $B := 12 \cdot in$

$$\frac{d^4}{dx^4}w(x,y) + 2 \cdot \frac{d^2}{dx^2}\frac{d^2}{dy^2}w(x,y) + \frac{d^4}{dy^4}w(x,y) = \frac{-p}{D}$$

$$D := \frac{E \cdot H^3}{12 \cdot \left(1 - \nu^2\right)} \qquad G := \frac{E}{2 \cdot (1 + \nu)} \qquad \sigma_o := \frac{\left(\sigma_y + \sigma_{ten}\right)}{2} \qquad \text{Plastic Flow Stress}$$

Blast Characteristics: $p_o := 130 \cdot psi$ $\tau := 0.2 \cdot 10^{-3} \cdot s$

Static Plastic Collapse Pressure of Rectangular Plates

Plastic collapse moment of solid cross-section:

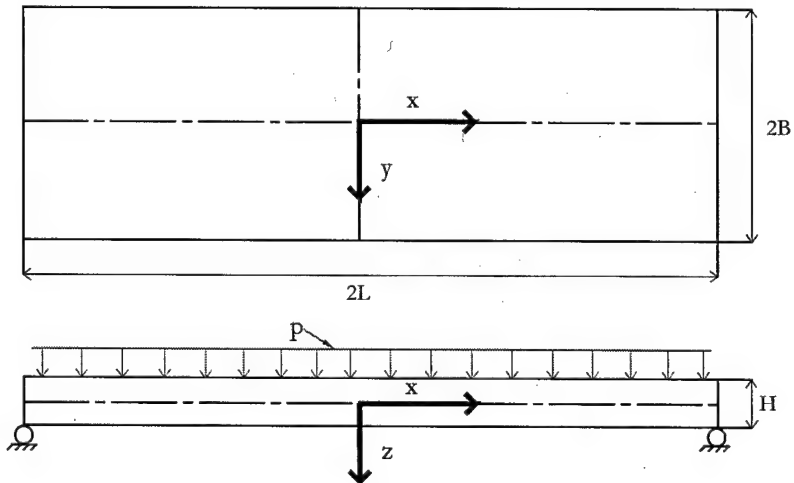$$M_o := \frac{\sigma_o \cdot B \cdot H^2}{4}$$

Use flow stress, σo, rather than yield stress to get plastic bending moment

Plastic collapse moment of solid x-section of unit width:

$$M_o := \frac{\sigma_o \cdot H^2}{4} \qquad M_o = 1.288\times 10^4 \, kg \, ms^{-2}$$

Simple Supports:

Lower bound (Johansen Yield Condition):

$$M_x(x) := M_0\left(1 - \frac{x^2}{L^2}\right) \qquad M_y(y) := M_0\left(1 - \frac{y^2}{B^2}\right) \qquad M_{xy}(x,y) := \frac{-M_0 \cdot x \cdot y}{B \cdot L}$$

Governing Equation:

$$\frac{\partial^2}{\partial x^2}M_x + 2 \cdot \frac{\partial}{\partial x}\frac{\partial}{\partial y}M_{xy} + \frac{d^2}{dy^2}M_y + p = 0$$

Substituting and solving for p:

$$p_{lower\_ss} := 2 \cdot M_0 \cdot \frac{\left[1 + \frac{L}{B} + \left(\frac{L}{B}\right)^2\right]}{L^2} \qquad p_{lower\_ss} = 8.317 \times 10^5 \, kg\,m^{-1}\,s^{-2}$$
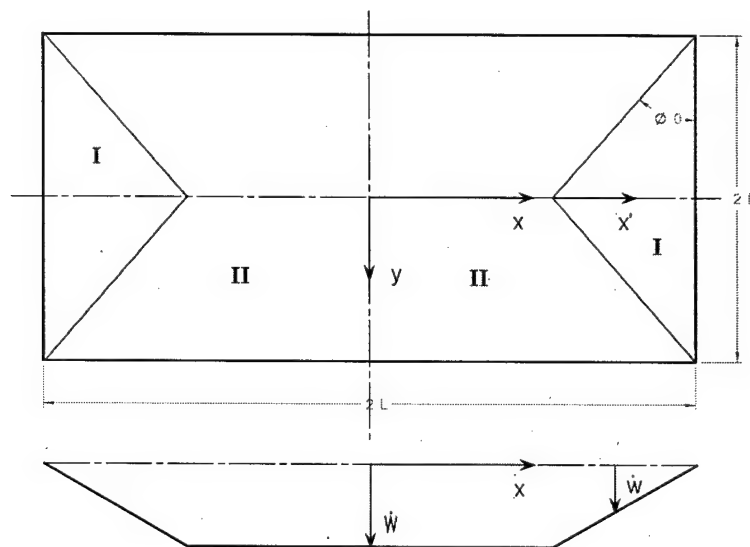
Upper bound (using energy method and kinematically admissable transverse velocity profile):

Velocity Profile:

Region I (triangles at ends) $w_{dot} = W_{dot} \cdot \dfrac{(B \cdot \tan(\phi) - x_{pr})}{B \cdot \tan(\phi)}$

Region II (center section) $w_{dot} = W_{dot} \cdot \dfrac{(B - y)}{B}$

Each of these regions remains rigid with plastic flow concentrated in the plastic hinges at the region boundaries.

100

Angular velocity at the outer boundaries (simply supported) are:

$$\frac{d}{dt}\theta = \frac{W_{dot}}{B \cdot \tan(\phi)}$$

Internal Energy Dissipation in plate:

$$D_{dot} = 4 \cdot M_o \cdot W_{dot} \cdot \left(\frac{L}{B} + \cot(\phi)\right)$$

External work due to uniform pressure p_upper:

$$E_{dot} = 2 \cdot B^2 \cdot W_{dot} \cdot p_{upper} \cdot \left(\frac{L}{B} - \frac{\tan(\phi)}{3}\right)$$

$$\beta := \frac{B}{L} \qquad \text{(aspect ratio of plate)}$$

Equating these energies and solving for p_upper:

$$p_{upper} = 6 \cdot M_o \cdot \frac{\left(1 + \frac{\beta}{\tan(\phi)}\right)}{B^2 \cdot (3 - \beta \cdot \tan(\phi))}$$

Assumptions are made to solve for ϕ, the angle of the plastic hinge line along which the velocity profile follows. Namely, the minimum p_upper occurs when the derivative of p_upper with respect to $\tan\phi$ is zero. Solving for $\tan\phi$, get:

$$\tan(\phi) = -\beta + \sqrt{3 + \beta^2} \qquad \text{which can then be substituted into the energy solution for p\_upper}$$

$$p_{upper\_ss} := \frac{6 \cdot M_o}{B^2 \cdot \left(\sqrt{3 + \beta^2} - \beta\right)^2} \qquad\qquad p_{upper\_ss} = 8.317 \times 10^5 \, Pa$$

Partially restrained supports (applying moment m to outer bound): $\qquad 0 \le m \le M_o$

m_supp determines the level of restraint on supports:
m=0 for simply supported, m=Mo for fully clamped

$$m_{supp} := 1.0 \cdot M_o$$

Gives additional internal energy dissapation around plate boundaries:

$$D_{dot\_b} = 4 \cdot m \cdot W_{dot} \cdot \left(\frac{B}{B \cdot \tan(\phi)} + \frac{L}{B}\right)$$

Add this to internal energy for the simple support case (from above) for:

$$D_{dot\_tot} = 4 \cdot M_o \cdot W_{dot} \cdot \left(\frac{L}{B} + \frac{1}{\tan(\phi)}\right) \cdot \left(1 + \frac{m}{M_o}\right)$$

The external work from p remains the same as above. Equating and solving for p:

$$p_{upper\_fc} := 6 \cdot M_o \cdot \frac{\left(1 + \dfrac{m_{supp}}{M_o}\right)}{B^2 \cdot \left(\sqrt{3 + \beta^2} - \beta\right)^2} \qquad\qquad p_{upper\_fc} = 1.663 \times 10^6 \, kg\,m^{-1}\,s^{-2}$$

For the fully clamped case, the lower bound is:

$$p_{lower\_fc} := 4 \cdot M_o \cdot \frac{\left(1 + \beta^2\right)}{B^2} \qquad\qquad p_{lower\_fc} = 1.109 \times 10^6 \, kg\,m^{-1}\,s^{-2}$$

For a fully clamped square plate, β goes to 1 and a numerical solution for the exact static collapse press can be found:

$$p_{c\_fc} := 10.71 \cdot \frac{M_o}{L^2} \qquad\qquad p_{c\_fc} = 1.485 \times 10^6 \, kg\,m^{-1}\,s^{-2}$$

Dynamic Plastic Behavior: Governing equations for rectangular plates

$$\frac{\partial}{\partial x} Q_x + \frac{\partial}{\partial y} Q_y + p = \mu \cdot \frac{\partial^2}{\partial t^2} w \qquad\qquad \text{note inclusion of inertia term in transverse direction}$$

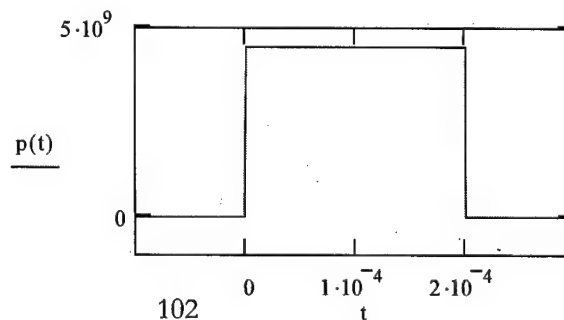$$\frac{\partial}{\partial x} M_x + \frac{\partial}{\partial y} M_{xy} - Q_x = 0 \qquad\qquad \text{Curvature Definitions in x and y directions:}$$

$$\frac{\partial}{\partial y} M_y + \frac{\partial}{\partial x} M_{xy} - Q_y = 0 \qquad \kappa_x = -\frac{\partial^2}{\partial x^2} w \qquad \kappa_y = -\frac{\partial^2}{\partial y^2} w \qquad \kappa_{xy} = -\frac{\partial}{\partial x}\frac{\partial}{\partial y} w$$

First look at the case of a rectangular pulse of pressure p_o lasting from time=0 until time=τ

$$\tau := 2.0 \cdot 10^{-4} \cdot s \qquad\qquad p(t) := p_o \cdot dunif(t, 0, \tau)$$

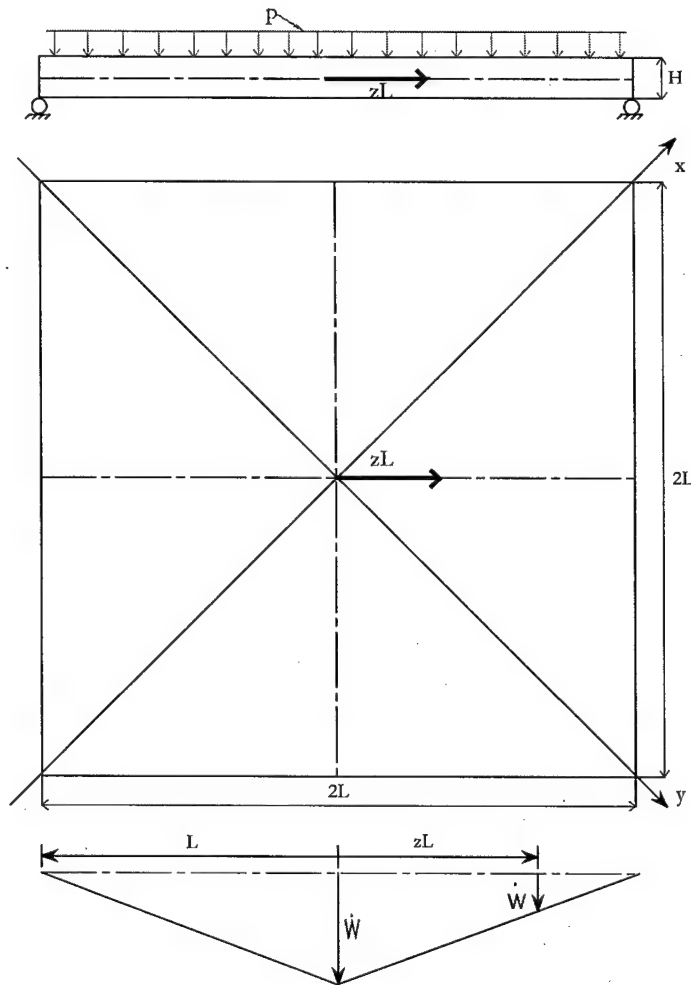102

Simply supported square plate: Static Collapse Pressure

$$p_{c\_ss} := \frac{6M_o}{L^2} \qquad p_{c\_ss} = 8.317 \times 10^5 \, kg\,m^{-1}\,s^{-2} \qquad \text{(from above)}$$

$$\frac{\partial}{\partial t} w = W_{dot} \cdot (1 - z) \qquad z(x,y) := \frac{(x + y) \cdot m}{\sqrt{2} \cdot L}$$

Plastic hinges form symmetrically along diagonal x and y axes, therefore can consider a single quadrant.

These equations are plugged in for each time period (0-τ, τ-T) where τ is the end of the pressure pulse and T is the end of motion in the plate.

$$\eta_{ss} := \frac{p_o}{p_{c\_ss}} \qquad \eta_{ss} = 1.078$$

For values of η greater than 2, a yield violation develops near the plate center, requiring a modification of the above transverse velocity field into three distinct phases:

$$w_{dot} = W_{dot} \qquad 0 \le z \le \zeta_0$$
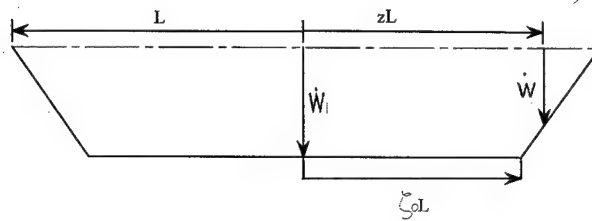
$$w_{dot} = W_{dot} \cdot \frac{(1-z)}{(1-\zeta_0)} \qquad \zeta_0 \le z \le 1$$
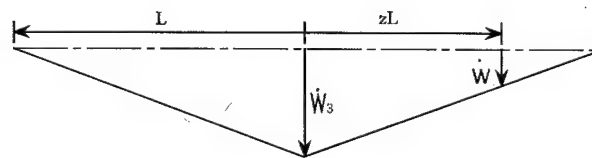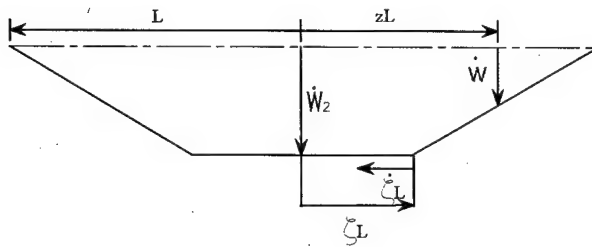
(solution admissable for η greater than 2):

$$W_{f2\_ss} := \eta_{ss} \cdot p_{c\_ss} \cdot \tau^2 \cdot \frac{(3 \cdot \eta_{ss} - 2)}{4 \cdot \mu} \qquad\qquad W_{f2\_ss} = 0.011m$$

104

DDG-51 Panel from Frame to Frame and Deck Girder to Deck Girder

Plate Characteristics:

Thickness: $H := 0.3438 \cdot in$ $L := 8.0 \cdot ft$ $B := 9.13 \cdot ft$

$$\frac{d^4}{dx^4} w(x,y) + 2 \cdot \frac{d^2}{dx^2} \frac{d^2}{dy^2} w(x,y) + \frac{d^4}{dy^4} w(x,y) = \frac{-p}{D}$$

For HSS Components:

$\sigma_y := 51 \cdot ksi$ $\sigma_y = 3.516 \times 10^8 \, kg \, m^{-1} \, s^{-2}$ $E := 29.6 \cdot 10^3 \cdot ksi$ $E = 2.041 \times 10^{11} \, kg \, m^{-1} \, s^{-2}$

$\sigma_{ten} := 70 \cdot ksi$ $\varepsilon_{rup} := 0.23$ $\rho := 7833 \cdot \frac{kg}{m^3}$ $\nu := .30$

$D := \dfrac{E \cdot H^3}{12 \cdot \left(1 - \nu^2\right)}$ $G := \dfrac{E}{2 \cdot (1 + \nu)}$ $\sigma_o := \dfrac{\left(\sigma_y + \sigma_{ten}\right)}{2}$ **Plastic Flow Stress**

Blast Characteristics:

$p_o := 1 \cdot 10^6 \cdot Pa$ $\tau := 0.2 \cdot 10^{-3} \cdot s$

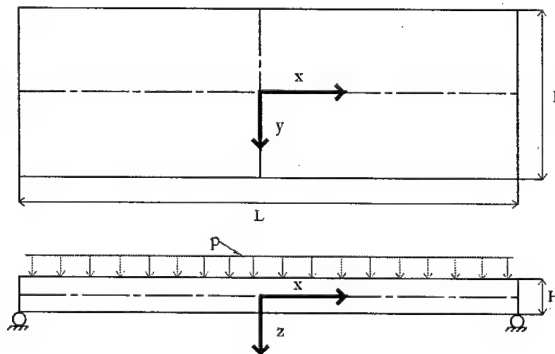Static Plastic Collapse Pressure of Rectangular Plates

Plastic collapse moment of solid cross-section:

$$M_o := \frac{\sigma_o \cdot B \cdot H^2}{4}$$

Plastic collapse moment of solid x-section of unit width:

$$M_o := \frac{\sigma_o \cdot H^2}{4} \qquad M_o = 7.952 \times 10^3 \, kg \, m \, s^{-2}$$

Simple Supports:

Lower bound (Johansen Yield Condition):   Define: $B_{pr} := \dfrac{B}{2}$ $L_{pr} := \dfrac{L}{2}$

$$M_x(x) := M_0\left(1 - \frac{x^2}{L_{pr}^2}\right) \qquad M_y(y) := M_0\left(1 - \frac{y^2}{B_{pr}^2}\right) \qquad M_{xy}(x,y) := \frac{-M_0 \cdot x \cdot y}{B_{pr} \cdot L_{pr}}$$

Governing Equation: $\dfrac{\partial^2}{\partial x^2}M_x + 2 \cdot \dfrac{\partial}{\partial x}\dfrac{\partial}{\partial y}M_{xy} + \dfrac{d^2}{dy^2}M_y + p = 0$

Substituting and solving for p:

$$P_{lower\_ss} := 2 \cdot M_0 \cdot \frac{\left[1 + \dfrac{L}{B} + \left(\dfrac{L}{B}\right)^2\right]}{L_{pr}^2} \qquad P_{lower\_ss} = 2.829\times 10^4 \, kg\,m^{-1}\,s^{-2}$$

Upper bound (using energy method and kinematically admissable transverse velocity profile):
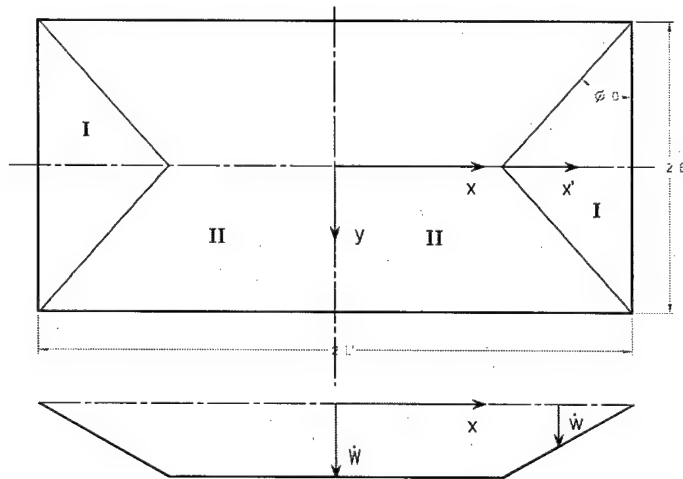
Velocity Profile:

Region I (triangles at ends) $w_{dot} = W_{dot} \cdot \dfrac{\left(B_{pr} \cdot \tan(\phi) - x_{pr}\right)}{B_{pr} \cdot \tan(\phi)}$

Region II (center section) $w_{dot} = W_{dot} \cdot \dfrac{\left(B_{pr} - y\right)}{B_{pr}}$

Each of these regions remains rigid with plastic flow concentrated in the plastic hinges at the region boundaries.

Angular velocity at the outer boundaries (simply supported) are:

$$\frac{d}{dt}\theta = \frac{W_{dot}}{B_{pr} \cdot \tan(\phi)}$$

Internal Energy Dissipation in plate:

$$D_{dot} = 4 \cdot M_o \cdot W_{dot} \cdot \left(\frac{L}{B} + \cot(\phi)\right)$$

External work due to uniform pressure p_upper:

$$E_{dot} = 2 \cdot B_{pr}^2 \cdot W_{dot} \cdot P_{upper} \cdot \left(\frac{L}{B} - \frac{\tan(\phi)}{3}\right)$$

$\beta := \frac{B}{L}$ (aspect ratio of plate)

Equating these energies and solving for p_upper:

$$P_{upper} = 6 \cdot M_o \cdot \frac{\left(1 + \frac{\beta}{\tan(\phi)}\right)}{B_{pr}^2 \cdot (3 - \beta \cdot \tan(\phi))}$$

Assumptions are made to solve for ϕ, the angle of the plastic hinge line along which the velocity profile follows. Namely, the minimum p_upper occurs when the derivative of p_upper with respect to tanφ is zero. Solving for tanφ, get:

$$\tan(\phi) = -\beta + \sqrt{3 + \beta^2}$$ which can then be substituted into the energy solution for p_upper

$$P_{upper\_ss} := \frac{6 \cdot M_o}{B_{pr}^2 \cdot \left(\sqrt{3 + \beta^2} - \beta\right)^2}$$ $P_{upper\_ss} = 2.831 \times 10^4 \, Pa$

Partially restrained supports (applying moment m to outer bound): $0 \le m \le M_o$■

m_supp determines the level of restraint on supports:
m=0 for simply supported, m=Mo for fully clamped $m_{supp} := 0.50 \cdot M_o$

Gives additional internal energy dissapation around plate boundaries:

$$D_{dot\_b} = 4 \cdot m \cdot W_{dot} \cdot \left(\frac{B_{pr}}{B_{pr} \cdot \tan(\phi)} + \frac{L}{B}\right)$$

Add this to internal energy for the simple support case (from above) for:

$$D_{dot\_tot} = 4 \cdot M_o \cdot W_{dot} \cdot \left(\frac{L}{B} + \frac{1}{\tan(\phi)}\right) \cdot \left(1 + \frac{m}{M_o}\right)$$

The external work from p remains the same as above. Equating and solving for p:

$$P_{upper\_pc} := 6 \cdot M_o \cdot \frac{\left(1 + \dfrac{m_{supp}}{M_o}\right)}{B_{pr}^2 \cdot \left(\sqrt{3 + \beta^2} - \beta\right)^2}$$

$$P_{upper\_pc} = 4.247 \times 10^4 \, kg \, m^{-1} \, s^{-2}$$

For the fully clamped case, the lower bound is:

$$P_{lower\_fc} := 4 \cdot M_o \cdot \frac{\left(1 + \beta^2\right)}{B_{pr}^2}$$

$$P_{lower\_fc} = 3.783 \times 10^4 \, kg \, m^{-1} \, s^{-2}$$

For the fully clamped case, the upper bound is:

$$P_{upper\_fc} := \frac{12 \cdot M_o}{B_{pr}^2 \cdot \left(\sqrt{3 + \beta^2} - \beta\right)^2}$$

$$P_{upper\_fc} = 5.663 \times 10^4 \, kg \, m^{-1} \, s^{-2}$$

DDG-51 Panel from Frame to Frame and Stiffener to Stiffener

Plate Characteristics:

Thickness: $H := 0.3438 \cdot in$ $L := 8.0 \cdot ft$ $B := 27.39 \cdot in$

$$\frac{d^4}{dx^4}w(x,y) + 2 \cdot \frac{d^2}{dx^2}\frac{d^2}{dy^2}w(x,y) + \frac{d^4}{dy^4}w(x,y) = \frac{-p}{D}$$

For HSS Components:

$\sigma_y := 51 \cdot ksi$ $\sigma_y = 3.516 \times 10^8 \, kg \, m^{-1} \, s^{-2}$ $E := 29.6 \cdot 10^3 \cdot ksi$ $E = 2.041 \times 10^{11} \, kg \, m^{-1} \, s^{-2}$

$\sigma_{ten} := 70 \cdot ksi$ $\varepsilon_{rup} := 0.23$ $\rho := 7833 \cdot \dfrac{kg}{m^3}$ $\nu := .30$

$D := \dfrac{E \cdot H^3}{12 \cdot \left(1 - \nu^2\right)}$ $G := \dfrac{E}{2 \cdot \left(1 + \nu\right)}$ $\sigma_0 := \dfrac{\left(\sigma_y + \sigma_{ten}\right)}{2}$ **Plastic Flow Stress**

Blast Characteristics:

$p_0 := 1 \cdot 10^6 \cdot Pa$ $\tau := 0.2 \cdot 10^{-3} \cdot s$ $p_0 = 1 \times 10^6 \, kg \, m^{-1} \, s^{-2}$

Static Plastic Collapse Pressure of Rectangular Plates (Jones p.37)

Plastic collapse moment of solid cross-section:

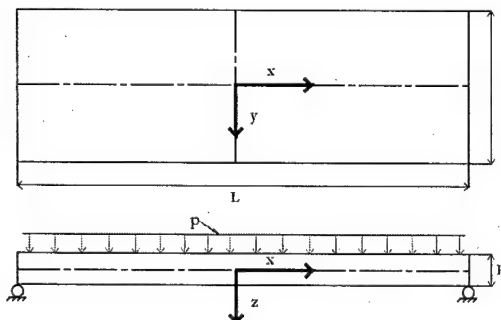$$M_0 := \frac{\sigma_0 \cdot B \cdot H^2}{4}$$

Plastic collapse moment of solid x-section of unit width:

$$M_0 := \frac{\sigma_0 \cdot H^2}{4} \qquad M_0 = 7.952 \times 10^3 \, kg \, m \, s^{-2}$$

Simple Supports:

Lower bound (Johansen Yield Condition):   Define: $B_{pr} := \dfrac{B}{2}$ $L_{pr} := \dfrac{L}{2}$

$$M_x(x) := M_0\left(1 - \frac{x^2}{L_{pr}^2}\right) \qquad M_y(y) := M_0\left(1 - \frac{y^2}{B_{pr}^2}\right) \qquad M_{xy}(x,y) := \frac{-M_0 \cdot x \cdot y}{B_{pr} \cdot L_{pr}}$$

Governing Equation:

$$\frac{\partial^2}{\partial x^2}M_x + 2 \cdot \frac{\partial}{\partial x}\frac{\partial}{\partial y}M_{xy} + \frac{d^2}{dy^2}M_y + p = 0$$

Substituting and solving for p:

$$P_{lower\_ss} := 2 \cdot M_0 \cdot \frac{\left[1 + \dfrac{L}{B} + \left(\dfrac{L}{B}\right)^2\right]}{L_{pr}^2} \qquad P_{lower\_ss} = 1.796 \times 10^5 \, kg\,m^{-1}\,s^{-2}$$

Upper bound (using energy method and kinematically admissable transverse velocity profile):
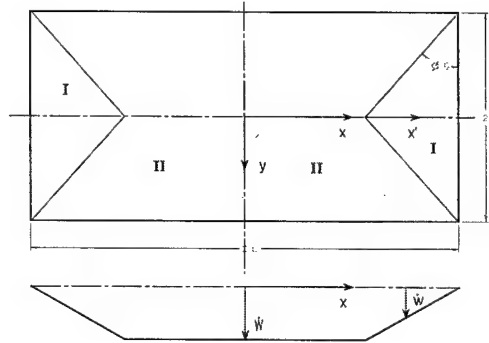
Velocity Profile:

Region I (triangles at ends) $w_{dot} = W_{dot} \cdot \dfrac{\left(B_{pr} \cdot \tan(\phi) - x_{pr}\right)}{B_{pr} \cdot \tan(\phi)}$

Region II (center section) $w_{dot} = W_{dot} \cdot \dfrac{\left(B_{pr} - y\right)}{B_{pr}}$

Each of these regions remains rigid with plastic flow concentrated in the plastic hinges at the region boundaries.

110

Angular velocity at the outer boundaries (simply supported) are:

$$\frac{d}{dt}\theta = \frac{W_{dot}}{B_{pr} \cdot \tan(\phi)}$$

Internal Energy Dissipation in plate:

$$D_{dot} = 4 \cdot M_o \cdot W_{dot} \cdot \left(\frac{L}{B} + \cot(\phi)\right)$$

External work due to uniform pressure p_upper:

$$E_{dot} = 2 \cdot B_{pr}^2 \cdot W_{dot} \cdot p_{upper} \cdot \left(\frac{L}{B} - \frac{\tan(\phi)}{3}\right)$$

$$\beta := \frac{B}{L} \quad \text{(aspect ratio of plate)}$$

Equating these energies and solving for p_upper:

$$p_{upper} = 6 \cdot M_o \cdot \frac{\left(1 + \frac{\beta}{\tan(\phi)}\right)}{B_{pr}^2 \cdot (3 - \beta \cdot \tan(\phi))}$$

Assumptions are made to solve for ϕ, the angle of the plastic hinge line along which the velocity profile follows. Namely, the minimum p_upper occurs when the derivative of p_upper with respect to $\tan\phi$ is zero. Solving for $\tan\phi$, get:

$$\tan(\phi) = -\beta + \sqrt{3 + \beta^2} \qquad \text{which can then be substituted into the energy solution for p\_upper}$$

$$p_{upper\_ss} := \frac{6 \cdot M_o}{B_{pr}^2 \cdot \left(\sqrt{3 + \beta^2} - \beta\right)^2} \qquad\qquad p_{upper\_ss} = 1.825 \times 10^5 \, Pa$$

Partially restrained supports (applying moment m to outer bound): $\qquad 0 \le m \le M_o$ ∎

m_supp determines the level of restraint on supports:
m=0 for simply supported, m=Mo for fully clamped $\qquad\qquad m_{supp} := 0.5 \cdot M_o$

Gives additional internal energy dissapation around plate boundaries:

$$D_{dot\_b} = 4 \cdot m \cdot W_{dot} \cdot \left(\frac{B_{pr}}{B_{pr} \cdot \tan(\phi)} + \frac{L}{B}\right)$$

Add this to internal energy for the simple support case (from above) for:

$$D_{dot\_tot} = 4 \cdot M_o \cdot W_{dot} \cdot \left(\frac{L}{B} + \frac{1}{\tan(\phi)}\right) \cdot \left(1 + \frac{m}{M_o}\right)$$

111

The external work from p remains the same as above. Equating and solving for p:

$$p_{pc} := 6 \cdot M_0 \cdot \frac{\left(1 + \dfrac{m_{supp}}{M_0}\right)}{B_{pr}^2 \cdot \left(\sqrt{3 + \beta^2} - \beta\right)^2}$$

$$p_{pc} = 2.737 \times 10^5 \, kg \, m^{-1} \, s^{-2}$$

For the fully clamped case, the lower bound is:

$$p_{lower\_fc} := 4 \cdot M_0 \cdot \frac{\left(1 + \beta^2\right)}{B_{pr}^2}$$

$$p_{lower\_fc} = 2.843 \times 10^5 \, kg \, m^{-1} \, s^{-2}$$

For the fully clamped case, the upper bound is:

$$p_{upper\_fc} := \frac{12 \cdot M_0}{B_{pr}^2 \cdot \left(\sqrt{3 + \beta^2} - \beta\right)^2}$$

$$p_{upper\_fc} = 3.649 \times 10^5 \, kg \, m^{-1} \, s^{-2}$$

DD(X) Panel from Frame to Frame and Deck Girder to Deck Girder

Plate Characteristics:

Thickness: $H := 0.4375 \cdot in$ $L := 7.54 \cdot ft$ $B := 9.99 \cdot ft$

$$\frac{d^4}{dx^4}w(x,y) + 2 \cdot \frac{d^2}{dx^2}\frac{d^2}{dy^2}w(x,y) + \frac{d^4}{dy^4}w(x,y) = \frac{-p}{D}$$

For HSS Components:

$\sigma_y := 51 \cdot ksi$ $\sigma_y = 3.516 \times 10^8 \, kg\,m^{-1}\,s^{-2}$ $E := 29.6 \cdot 10^3 \cdot ksi$ $E = 2.041 \times 10^{11} \, kg\,m^{-1}\,s^{-2}$

$\sigma_{ten} := 70 \cdot ksi$ $\varepsilon_{rup} := 0.23$ $\rho := 7833 \cdot \frac{kg}{m^3}$ $\nu := .30$

$D := \frac{E \cdot H^3}{12 \cdot \left(1 - \nu^2\right)}$ $G := \frac{E}{2 \cdot (1 + \nu)}$ $\sigma_0 := \frac{\left(\sigma_y + \sigma_{ten}\right)}{2}$ **Plastic Flow Stress**

Blast Characteristics:

$p_0 := 1 \cdot 10^6 \cdot Pa$ $\tau := 0.2 \cdot 10^{-3} \cdot s$ $p_0 = 1 \times 10^6 \, kg\,m^{-1}\,s^{-2}$

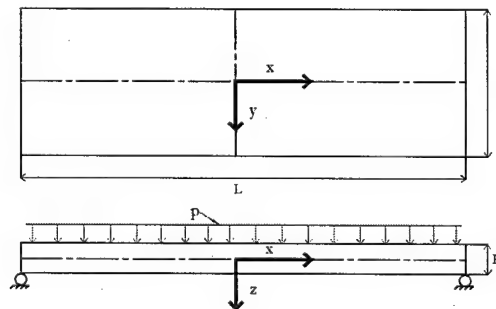Static Plastic Collapse Pressure of Rectangular Plates (Jones p.37)

Plastic collapse moment of solid cross-section:

$$M_0 := \frac{\sigma_0 \cdot B \cdot H^2}{4}$$

Plastic collapse moment of solid x-section of unit width:

$M_0 := \frac{\sigma_0 \cdot H^2}{4}$ $M_0 = 1.288 \times 10^4 \, kg\,m\,s^{-2}$

Simple Supports:

Lower bound (Johansen Yield Condition):   Define: $B_{pr} := \dfrac{B}{2}$ $L_{pr} := \dfrac{L}{2}$

$$M_x(x) := M_0 \left(1 - \dfrac{x^2}{L_{pr}^2} \right)$$ $$M_y(y) := M_0 \left(1 - \dfrac{y^2}{B_{pr}^2} \right)$$ $$M_{xy}(x,y) := \dfrac{-M_0 \cdot x \cdot y}{B_{pr} \cdot L_{pr}}$$

Governing Equation: $$\dfrac{\partial^2}{\partial x^2} M_x + 2 \cdot \dfrac{\partial}{\partial x} \dfrac{\partial}{\partial y} M_{xy} + \dfrac{d^2}{dy^2} M_y + p = 0$$

Substituting and solving for p:

$$p_{lower\_ss} := 2 \cdot M_0 \cdot \dfrac{\left[1 + \dfrac{L}{B} + \left(\dfrac{L}{B} \right)^2 \right]}{L_{pr}^2}$$ $p_{lower\_ss} = 4.534 \times 10^4 \, kg \, m^{-1} \, s^{-2}$

Upper bound (using energy method and kinematically admissable transverse velocity profile):

Velocity Profile:

Region I (triangles at ends) $$w_{dot} = W_{dot} \cdot \dfrac{(B_{pr} \cdot \tan(\phi) - x_{pr})}{B_{pr} \cdot \tan(\phi)}$$

Region II (center section) $$w_{dot} = W_{dot} \cdot \dfrac{(B_{pr} - y)}{B_{pr}}$$

Each of these regions remains rigid with plastic flow concentrated in the plastic hinges at the region boundaries.

114

Angular velocity at the outer boundaries (simply supported) are:

$$\frac{d}{dt}\theta = \frac{W_{dot}}{B_{pr} \cdot \tan(\phi)}$$

Internal Energy Dissipation in plate: $D_{dot} = 4 \cdot M_o \cdot W_{dot} \cdot \left(\frac{L}{B} + \cot(\phi)\right)$

External work due to uniform pressure p_upper: $E_{dot} = 2 \cdot B_{pr}^2 \cdot W_{dot} \cdot p_{upper} \cdot \left(\frac{L}{B} - \frac{\tan(\phi)}{3}\right)$

$\beta := \frac{B}{L}$ (aspect ratio of plate)

Equating these energies and solving for p_upper: $p_{upper} = 6 \cdot M_o \cdot \dfrac{\left(1 + \dfrac{\beta}{\tan(\phi)}\right)}{B_{pr}^2 \cdot (3 - \beta \cdot \tan(\phi))}$

Assumptions are made to solve for ϕ, the angle of the plastic hinge line along which the velocity profile follows. Namely, the minimum p_upper occurs when the derivative of p_upper with respect to $\tan\phi$ is zero. Solving for $\tan\phi$, get:

$$\tan(\phi) = -\beta + \sqrt{3 + \beta^2}$$ which can then be substituted into the energy solution for p_upper

$$p_{upper\_ss} := \frac{6 \cdot M_o}{B_{pr}^2 \cdot \left(\sqrt{3 + \beta^2} - \beta\right)^2}$$ $p_{upper\_ss} = 4.552 \times 10^4 \, Pa$

Partially restrained supports (applying moment m to outer bound): $0 \le m \le M_o$

m_supp determines the level of restraint on supports:
m=0 for simply supported, m=Mo for fully clamped $m_{supp} := 0.5 \cdot M_o$

Gives additional internal energy dissapation around plate boundaries:

$$D_{dot\_b} = 4 \cdot m \cdot W_{dot} \cdot \left(\frac{B_{pr}}{B_{pr} \cdot \tan(\phi)} + \frac{L}{B}\right)$$

Add this to internal energy for the simple support case (from above) for:

$$D_{dot\_tot} = 4 \cdot M_o \cdot W_{dot} \cdot \left(\frac{L}{B} + \frac{1}{\tan(\phi)}\right) \cdot \left(1 + \frac{m}{M_o}\right)$$

The external work from p remains the same as above. Equating and solving for p:

$$p_{pc} := 6 \cdot M_o \cdot \frac{\left(1 + \dfrac{m_{supp}}{M_o}\right)}{B_{pr}^2 \cdot \left(\sqrt{3 + \beta^2} - \beta\right)^2}$$

$$p_{pc} = 6.828 \times 10^4 \, kg \, m^{-1} \, s^{-2}$$

For the fully clamped case, the lower bound is:

$$p_{lower\_fc} := 4 \cdot M_o \cdot \frac{\left(1 + \beta^2\right)}{B_{pr}^2}$$

$$p_{lower\_fc} = 6.123 \times 10^4 \, kg \, m^{-1} \, s^{-2}$$

For the fully clamped case, the upper bound is:

$$p_{upper\_fc} := \frac{12 \cdot M_o}{B_{pr}^2 \cdot \left(\sqrt{3 + \beta^2} - \beta\right)^2}$$

$$p_{upper\_fc} = 9.104 \times 10^4 \, kg \, m^{-1} \, s^{-2}$$

116

DD(X) Panel from Frame to Frame and Stiffener to Stiffener

Plate Characteristics:

Thickness: $H := 0.4375 \cdot in$ $L := 7.54 \cdot ft$ $B := 23.99 \cdot in$

$$\frac{d^4}{dx^4} w(x,y) + 2 \cdot \frac{d^2}{dx^2} \frac{d^2}{dy^2} w(x,y) + \frac{d^4}{dy^4} w(x,y) = \frac{-p}{D}$$

For HSS Components:

$\sigma_y := 51 \cdot ksi$ $\sigma_y = 3.516 \times 10^8 \, kg \, m^{-1} \, s^{-2}$ $E := 29.6 \cdot 10^3 \cdot ksi$ $E = 2.041 \times 10^{11} \, kg \, m^{-1} \, s^{-2}$

$\sigma_{ten} := 70 \cdot ksi$ $\varepsilon_{rup} := 0.23$ $\rho := 7833 \cdot \frac{kg}{m^3}$ $\nu := .30$

$D := \frac{E \cdot H^3}{12 \cdot (1 - \nu^2)}$ $G := \frac{E}{2 \cdot (1 + \nu)}$ $\sigma_0 := \frac{(\sigma_y + \sigma_{ten})}{2}$ **Plastic Flow Stress**

Blast Characteristics:

$p_0 := 1 \cdot 10^6 \cdot Pa$ $\tau := 0.2 \cdot 10^{-3} \cdot s$ $p_0 = 1 \times 10^6 \, kg \, m^{-1} \, s^{-2}$

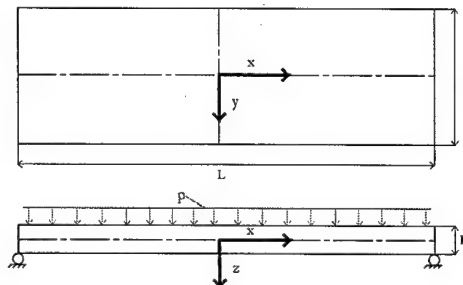Static Plastic Collapse Pressure of Rectangular Plates (Jones p.37)

Plastic collapse moment of solid cross-section:

$$M_0 := \frac{\sigma_0 \cdot B \cdot H^2}{4}$$

Plastic collapse moment of solid x-section of unit width:

$M_0 := \frac{\sigma_0 \cdot H^2}{4}$ $M_0 = 1.288 \times 10^4 \, kg \, m \, s^{-2}$

Simple Supports:

Lower bound (Johansen Yield Condition):   Define: $B_{pr} := \dfrac{B}{2}$ $L_{pr} := \dfrac{L}{2}$

$$M_x(x) := M_0 \left(1 - \frac{x^2}{L_{pr}^2} \right) \qquad M_y(y) := M_0 \left(1 - \frac{y^2}{B_{pr}^2} \right) \qquad M_{xy}(x,y) := \frac{-M_0 \cdot x \cdot y}{B_{pr} \cdot L_{pr}}$$

Governing Equation:
$$\frac{\partial^2}{\partial x^2} M_x + 2 \cdot \frac{\partial}{\partial x} \frac{\partial}{\partial y} M_{xy} + \frac{d^2}{dy^2} M_y + p = 0$$

Substituting and solving for p:
$$P_{lower\_ss} := 2 \cdot M_0 \cdot \frac{\left[1 + \frac{L}{B} + \left(\frac{L}{B} \right)^2 \right]}{L_{pr}^2} \qquad P_{lower\_ss} = 3.705 \times 10^5 \, kg\,m^{-1}\,s^{-2}$$

Upper bound (using energy method and kinematically admissable transverse velocity profile):
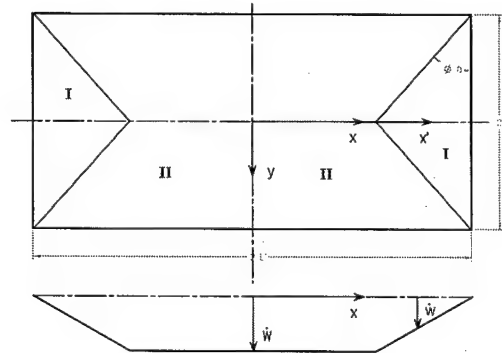
Velocity Profile:

Region I (triangles at ends)
$$w_{dot} = W_{dot} \cdot \frac{\left(B_{pr} \cdot \tan(\phi) - x_{pr} \right)}{B_{pr} \cdot \tan(\phi)}$$

Region II (center section)
$$w_{dot} = W_{dot} \cdot \frac{\left(B_{pr} - y \right)}{B_{pr}}$$

Each of these regions remains rigid with plastic flow concentrated in the plastic hinges at the region boundaries.

Angular velocity at the outer boundaries (simply supported) are:

$$\frac{d}{dt}\theta = \frac{W_{dot}}{B_{pr} \cdot \tan(\phi)}$$

Internal Energy Dissipation in plate:

$$D_{dot} = 4 \cdot M_o \cdot W_{dot} \cdot \left(\frac{L}{B} + \cot(\phi)\right)$$

External work due to uniform pressure p_upper:

$$E_{dot} = 2 \cdot B_{pr}^2 \cdot W_{dot} \cdot p_{upper} \cdot \left(\frac{L}{B} - \frac{\tan(\phi)}{3}\right)$$

$$\beta := \frac{B}{L} \quad \text{(aspect ratio of plate)}$$

Equating these energies and solving for p_upper:

$$p_{upper} = 6 \cdot M_o \cdot \frac{\left(1 + \frac{\beta}{\tan(\phi)}\right)}{B_{pr}^2 \cdot (3 - \beta \cdot \tan(\phi))}$$

Assumptions are made to solve for ϕ, the angle of the plastic hinge line along which the velocity profile follows. Namely, the minimum p_upper occurs when the derivative of p_upper with respect to $\tan\phi$ is zero. Solving for $\tan\phi$, get:

$$\tan(\phi) = -\beta + \sqrt{3 + \beta^2} \quad \text{which can then be substituted into the energy solution for p_upper}$$

$$p_{upper\_ss} := \frac{6 \cdot M_o}{B_{pr}^2 \cdot \left(\sqrt{3 + \beta^2} - \beta\right)^2} \qquad p_{upper\_ss} = 3.764 \times 10^5 \, Pa$$

Partially restrained supports (applying moment m to outer bound): $\qquad 0 \le m \le M_o$ ■

m_supp determines the level of restraint on supports:
m=0 for simply supported, m=Mo for fully clamped $\qquad m_{supp} := 0.5 \cdot M_o$

Gives additional internal energy dissapation around plate boundaries:

$$D_{dot\_b} = 4 \cdot m \cdot W_{dot} \cdot \left(\frac{B_{pr}}{B_{pr} \cdot \tan(\phi)} + \frac{L}{B}\right)$$

Add this to internal energy for the simple support case (from above) for:

$$D_{dot\_tot} = 4 \cdot M_o \cdot W_{dot} \cdot \left(\frac{L}{B} + \frac{1}{\tan(\phi)}\right) \cdot \left(1 + \frac{m}{M_o}\right)$$

The external work from p remains the same as above. Equating and solving for p:

$$p_{pc} := 6 \cdot M_o \cdot \frac{\left(1 + \dfrac{m_{supp}}{M_o}\right)}{B_{pr}^2 \cdot \left(\sqrt{3 + \beta^2} - \beta\right)^2}$$

$$p_{pc} = 5.646 \times 10^5 \, kg \, m^{-1} \, s^{-2}$$

For the fully clamped case, the lower bound is:

$$p_{lower\_fc} := 4 \cdot M_o \cdot \frac{\left(1 + \beta^2\right)}{B_{pr}^2}$$

$$p_{lower\_fc} = 5.939 \times 10^5 \, kg \, m^{-1} \, s^{-2}$$

For the fully clamped case, the upper bound is:

$$p_{upper\_fc} := \frac{12 \cdot M_o}{B_{pr}^2 \cdot \left(\sqrt{3 + \beta^2} - \beta\right)^2}$$

$$p_{upper\_fc} = 7.528 \times 10^5 \, kg \, m^{-1} \, s^{-2}$$

APPENDIX G: CALCULATIONS BASED ON DDS 100-7

Calculation for Panel from Frame to Frame and Deck Girder to Deck Girder

Uniform load over a x b plate - values at center :

$$\sigma_{max} = \frac{\beta \cdot P \cdot b^2}{h^2} \qquad y_{max} = \frac{-\alpha \cdot P \cdot b^4}{E \cdot h^3} \qquad React_{max} = \gamma \cdot P \cdot b$$

Maximum stress   Maximum displacement   Maximum reaction at long side (what stiffener must support)

Using flow stress for σmax and solving for P:

$$\frac{L_g}{B_g} = 0.876 \qquad \text{<--These get } \beta \text{ -->} \qquad \frac{L_x}{B_x} = 0.755$$
$$\text{(from table)}$$

$$\beta_g := .2874 \qquad\qquad \beta_x := .2874$$

Must redefine sizes in English units without unit calculations on:

$h_g := .3438$ inches $h_x := .4375$ inches

$b_g := 109.56$ inches $b_x := 119.88$ inches

$l_g := 96$ inches $l_x := 90.48$ inches

$$\sigma_{flow} := 6.05 \cdot 10^4 \qquad \text{psi}$$

$$P_{unifg} := \frac{\sigma_{flow} \cdot h_g^2}{b_g \cdot \beta_g} \qquad\qquad P_{unifx} := \frac{\sigma_{flow} \cdot h_x^2}{b_x \cdot \beta_x}$$

$$P_{unifg} = 227.106 \qquad\qquad P_{unifx} = 336.107$$

These pressures are both in psi

$$P_{dds\_g} := P_{unifg} \cdot psi \qquad\qquad P_{dds\_x} := P_{unifx} \cdot psi$$

$$P_{dds\_g} = 1.566 \times 10^6 \, Pa \qquad\qquad P_{dds\_x} = 2.317 \times 10^6 \, Pa$$

Calculation for Panel from Frame to Frame and Stiffener to Stiffener

Uniform load over a x b plate - values at center :

$$\sigma_{max} = \frac{\beta \cdot P \cdot b^2}{h^2} \qquad y_{max} = \frac{-\alpha \cdot P \cdot b^4}{E \cdot h^3} \qquad React_{max} = \gamma \cdot P \cdot b$$

Maximum stress   Maximum displacement   Maximum reaction at long side (what stiffener must support)

Using flow stress for σmax and solving for P:

$$\frac{L_g}{B_g} = 3.505 \qquad \text{<--These get } \beta \text{ --> } \qquad \frac{L_x}{B_x} = 3.775$$
(from table)

$$\beta_g := 0.7134 + \left(\frac{L_g}{B_g} - 3\right) \cdot (0.7410 - 0.7134) \qquad \text{(interpolation steps)}$$

$$\beta_x := 0.7134 + \left(\frac{L_x}{B_x} - 3\right) \cdot (0.7410 - 0.7134)$$

$$\beta_g = 0.727 \qquad\qquad \beta_x = 0.735$$

Must redefine sizes in English units without unit calculations on:

$h_g := .3438$ inches $h_x := .4375$ inches

$b_g := 27.3\text{?}$ inches $b_x := 23.99$ inches

$l_g := 96$ inches $l_x := 90.55$ inches

$$\sigma_{flow} := 6.05 \cdot 10^4 \qquad psi$$

$$P_{unifg} := \frac{\sigma_{flow} \cdot h_g^2}{b_g \cdot \beta_g} \qquad\qquad P_{unifx} := \frac{\sigma_{flow} \cdot h_x^2}{b_x \cdot \beta_x}$$

$$P_{unifg} = 358.955 \qquad\qquad P_{unifx} = 656.939$$

These pressures are both in psi

$$P_{dds\_g} := P_{unifg} \cdot psi \qquad\qquad P_{dds\_x} := P_{unifx} \cdot psi$$

$$P_{dds\_g} = 2.475 \times 10^6 \, Pa \qquad\qquad P_{dds\_x} = 4.529 \times 10^6 \, Pa$$

123

APPENDIX H: CALCULATIONS BASED ON DDS 100-9

Ambient Pressure

$P_a := 14.7\text{psi}$

Peak Incident Overpressure

$P_1 := 130.316\text{psi}$

Duration of Positive Phase

$\tau := 0.2 \cdot 10^{-3} \cdot \text{sec}$

Max Reflected Overpressure

$P_r := 2 \cdot P_1 \cdot \left(\dfrac{7 \cdot P_a + 4 \cdot P_1}{7 \cdot P_a + P_1} \right)$

Dynamic Pressure

$q_0 := \dfrac{5}{2} \cdot \left(\dfrac{P_1^2}{7 \cdot P_a + P_1} \right)$

Stagnation Pressure

$P_s := P_1 + q_0$

Peak Avg Pressure

$P_c := P_1 - 0.4 q_0$

$P_r = 697.538\text{psi}$

$q_0 = 182.044\text{psi}$

$P_s = 312.36\text{psi}$

$P_c = 57.498\text{psi}$

Get plastic section modulus at midspan, Zpm:

$A_{totg} := T_g \cdot B_g + A_g$

$A_{pltg} := T_g \cdot B_g$

$A_{totx} := T_x \cdot B_x + A_x$

$A_{pltx} := T_x \cdot B_x$

$\dfrac{A_{totg}}{2} = 5.613\text{in}^2$

$A_{pltg} = 9.417\text{in}^2$

$\dfrac{A_{totx}}{2} = 6.303\text{in}^2$

$A_{pltx} = 10.496\text{in}^2$

Both cases have Atot/2 < Aplt so they correspond to regime 1 in Table 3:

$d_{namg} := \dfrac{A_{totg}}{2 \cdot B_g}$

$d_{namx} := \dfrac{A_{totx}}{2 \cdot B_x}$

$Z_{1mg} := \dfrac{1}{2} \cdot B_g \cdot d_{namg}^2$

$Z_{1mx} := \dfrac{1}{2} \cdot B_x \cdot d_{namx}^2$

$Z_{2mg} := \dfrac{1}{2} \cdot B_g \cdot \left(T_g - d_{namg} \right)^2 + A_{webg} \cdot \left(\dfrac{D_g - TF_g}{2} + T_g - d_{namg} \right) + A_{flag} \cdot \left(D_g - \dfrac{TF_g}{2} + T_g - d_{namg} \right)$

$Z_{2mx} := \dfrac{1}{2} \cdot B_x \cdot \left(T_x - d_{namx} \right)^2 + A_{webx} \cdot \left(\dfrac{D_x - TF_x}{2} + T_x - d_{namx} \right) + A_{flax} \cdot \left(D_x - \dfrac{TF_x}{2} + T_x - d_{namx} \right)$

$Z_{PMg} := Z_{1mg} + Z_{2mg}$

$Z_{PMx} := Z_{1mx} + Z_{2mx}$

$Z_{PMg} = 8.745\text{in}^3$

$Z_{PMx} = 12.874\text{in}^3$

Get plastic section modulus at support, Zps:

$$A_{pltg} = 9.417in^2 \qquad\qquad A_{pltx} = 10.496in^2$$

$$A_{flag} = 0.847in^2 \qquad\qquad A_{flax} = 0.808in^2$$

Both cases have Aplt > Afla so they correspond to regime 1 in Table 4:

$$d_{nasg} := \frac{1}{2}\cdot\left(T_g + \frac{A_{flag}}{B_g}\right) \qquad\qquad d_{nasx} := \frac{1}{2}\cdot\left(T_x + \frac{A_{flax}}{B_x}\right)$$

$$Z_{1sg} := \frac{1}{2}\cdot B_g\cdot d_{nasg}^2 \qquad\qquad Z_{1sx} := \frac{1}{2}\cdot B_x\cdot d_{nasx}^2$$

$$Z_{2sg} := \frac{1}{2}\cdot B_g\cdot\left(T_g - d_{nasg}\right)^2 \qquad\qquad Z_{2sx} := \frac{1}{2}\cdot B_x\cdot\left(T_x - d_{nasx}\right)^2$$

$$Z_{3sg} := A_{flag}\cdot\left(D_g + T_g - \frac{TF_g}{2} - d_{nasg}\right) \qquad Z_{3sx} := A_{flax}\cdot\left(D_x + T_x - \frac{TF_x}{2} - d_{nasx}\right)$$

$$Z_{PSg} := Z_{1sg} + Z_{2sg} + Z_{3sg} \qquad\qquad Z_{PSx} := Z_{1sx} + Z_{2sx} + Z_{3sx}$$

$$Z_{PSg} = 5.855in^3 \qquad\qquad Z_{PSx} = 7.608in^3$$

Plastic Flow Stress / Dynamic Yield stress

$$\sigma_{dym} := \frac{\left(\sigma_{yms} + \sigma_{ten\_ms}\right)}{2} \qquad\qquad \sigma_{dyh} := \frac{\left(\sigma_{yhs} + \sigma_{ten\_hs}\right)}{2}$$

$$\sigma_{dym} = 4.6\times 10^4\,psi \qquad\qquad \sigma_{dyh} = 6.05\times 10^4\,psi$$

Ductility Factors
(μ1 per ship specifications, μ2 for max deflection without rupture)

$$\mu_1 := 1.5 \qquad\qquad \mu_2 := 20$$

Maximum beam resistance

$$R_{pg} := \frac{8\cdot\sigma_{dym}}{L_g}\cdot\left(Z_{PSg} + Z_{PMg}\right) \qquad\qquad R_{px} := \frac{8\cdot\sigma_{dym}}{L_x}\cdot\left(Z_{PSx} + Z_{PMx}\right)$$

$$R_{pg} = 5.597\times 10^4\,lbf \qquad\qquad R_{px} = 8.324\times 10^4\,lbf$$

Natural period of stiffeners

$$M_{tg} := \left(B_g \cdot T_g + A_g\right) \cdot L_g \cdot \rho_{ms} \qquad\qquad M_{tx} := \left(B_x \cdot T_x + A_x\right) \cdot L_x \cdot \rho_{ms}$$

$$M_{tg} = 304.99 \, lb \qquad\qquad\qquad M_{tx} = 323.017 \, lb$$

$$k_{ebarg} := \frac{307 \cdot E_{ms} \cdot I_g}{L_g^{\,3}} \qquad\qquad k_{ebarx} := \frac{307 \cdot E_{ms} \cdot I_x}{L_x^{\,3}} \qquad\qquad \text{for } \mu > 1$$

$$k_{ebarg} = 2.578 \times 10^7 \, \frac{lb}{sec^2} \qquad\qquad k_{ebarx} = 6.71 \times 10^7 \, \frac{lb}{sec^2}$$

$$K_{LM} := 0.66 \qquad \text{for } \mu > 1$$

$$T_{ng} := 2 \cdot \pi \cdot \left(\frac{K_{LM} \cdot M_{tg}}{k_{ebarg}}\right)^{0.5} \qquad\qquad T_{nx} := 2 \cdot \pi \cdot \left(\frac{K_{LM} \cdot M_{tx}}{k_{ebarx}}\right)^{0.5}$$

$$T_{ng} = 0.018 \, sec \qquad\qquad\qquad T_{nx} = 0.011 \, sec$$

For single pulse loading case, required resistance:

$$F_{1g} := \frac{T_{ng}}{\pi \cdot \tau} \cdot \left(2 \cdot \mu_1 - 1\right)^{0.5} + \frac{2 \cdot \mu_1 - 1}{2 \cdot \mu_1 \cdot \left[1 + \left(0.7 \cdot \frac{T_{ng}}{\tau}\right)\right]} \qquad F_{1x} := \frac{T_{nx}}{\pi \cdot \tau} \cdot \left(2 \cdot \mu_1 - 1\right)^{0.5} + \frac{2 \cdot \mu_1 - 1}{2 \cdot \mu_1 \cdot \left[1 + \left(0.7 \cdot \frac{T_{nx}}{\tau}\right)\right]}$$

$$F_{2g} := \frac{T_{ng}}{\pi \cdot \tau} \cdot \left(2 \cdot \mu_2 - 1\right)^{0.5} + \frac{2 \cdot \mu_2 - 1}{2 \cdot \mu_2 \cdot \left[1 + \left(0.7 \cdot \frac{T_{ng}}{\tau}\right)\right]} \qquad F_{2x} := \frac{T_{nx}}{\pi \cdot \tau} \cdot \left(2 \cdot \mu_2 - 1\right)^{0.5} + \frac{2 \cdot \mu_2 - 1}{2 \cdot \mu_2 \cdot \left[1 + \left(0.7 \cdot \frac{T_{nx}}{\tau}\right)\right]}$$

$$R_{r1g} := \frac{P_s \cdot B_g \cdot L_g}{F_{1g}} \qquad R_{r1g} = 6.425 \times 10^4 \, lbf \qquad R_{r1x} := \frac{P_s \cdot B_x \cdot L_x}{F_{1x}} \qquad R_{r1x} = 8.319 \times 10^4 \, lbf$$

$$R_{r2g} := \frac{P_s \cdot B_g \cdot L_g}{F_{2g}} \qquad R_{r2g} = 1.455 \times 10^4 \, lbf \qquad R_{r2x} := \frac{P_s \cdot B_x \cdot L_x}{F_{2x}} \qquad R_{r2x} = 1.885 \times 10^4 \, lbf$$

$$R_{r1g} = 2.858 \times 10^5 \, newton \qquad\qquad R_{r1x} = 3.7 \times 10^5 \, newton$$

$$R_{pg} = 2.49 \times 10^5 \, newton \qquad\qquad\qquad R_{px} = 3.702 \times 10^5 \, newton$$

$$R_{r2g} = 6.473 \times 10^4 \, newton \qquad\qquad R_{r2x} = 8.383 \times 10^4 \, newton$$

APPENDIX I: COMPARISON OF STIFFENED PANEL CALCULATIONS

		Units	DDG - 51 Class	DD(X)
	T (PlateThickness)	in	0.3438	0.4375
	L (Frame Spacing)	ft	8	7.54
	H (Deck Height)	ft	9.13	9.99
	Stiffeners per panel		3	4
	Stiffener Spacing	ft	3.043	2.498
Plate Between Decks and Girders/Frames	Static Failure Pressure (Moment calculation)	Pa	1.23E+04	1.67E+04
	Dynamic Failure Pressure (Moment + strain rate effects)	Pa	3.65E+04	4.93E+04
	Simply Supported Lower Bound (Johansen Yield Condition)	Pa	2.83E+04	4.53E+04
	Simply Supported Upper Bound (Energy Method with Velocity Profile)	Pa	2.83E+04	4.55E+04
	Fully Clamped Lower Bound (Statically Admissible Stress Field)	Pa	3.78E+04	6.12E+04
	Fully Clamped Upper Bound (Energy Dissipation Method)	Pa	5.66E+04	9.10E+04
	Partially Clamped (50%) (Energy Method)	Pa	4.25E+04	6.83E+04
	DDS 100-7 (blast loading)	Pa	1.57E+06	2.32E+06
	DDS 100-9 (air blast / nuclear)			
	For Max Deflection w/o rupture	Pa	2.55E+07	2.94E+07
	For Ship Specifications	Pa	5.75E+06	6.66E+06
Plate Between Stiffeners and Girders/Frames	Static Failure Pressure (Moment calculation)	Pa	4.93E+04	1.04E+05
	Dynamic Failure Pressure (Moment + strain rate effects)	Pa	1.46E+05	3.08E+05
	Simply Supported Lower Bound (Johansen Yield Condition)	Pa	1.80E+05	3.71E+05
	Simply Supported Upper Bound (Energy Method with Velocity Profile)	Pa	1.83E+05	3.76E+05
	Fully Clamped Lower Bound (Statically Admissible Stress Field)	Pa	2.84E+05	5.94E+05
	Fully Clamped Upper Bound (Energy Dissipation Method)	Pa	3.65E+05	7.53E+05
	Partially Clamped (50%) (Energy Method)	Pa	2.74E+05	5.65E+05
	DDS 100-7 (blast loading)	Pa	2.48E+06	4.53E+06
	DDS 100-9 (air blast / nuclear)			
	For Max Deflection w/o rupture	Pa	2.55E+07	2.94E+07
	For Ship Specifications	Pa	5.75E+06	6.66E+06